UNIVERSITAT DE BARCELONA

Engineering *in vitro* models of the intestinal mucosa to study the role of the stroma on the epithelium

Aina Abad i Lázaro

Doctoral thesis

Engineering *in vitro* models of the intestinal mucosa to study the role of the stroma on the epithelium

Aina Abad i Lázaro

UNIVERSITAT DE BARCELONA

Engineering *in vitro* models of the intestinal mucosa to study the role of the stroma on the epithelium

Memòria presentada per optar al grau de doctor per la Universitat de Barcelona
Programa de doctorat en Biomedicina

Autora: Aina Abad i Lázaro

Directora: Elena Martínez Fraiz

Tutor: Josep Samitier Martí

Institut de Bioenginyeria de Catalunya (IBEC)

UNIVERSITAT DE BARCELONA

Acknowledgements

Aquesta tesi doctoral que trobareu a continuació és la culminació d'una de les etapes més importants de la meva vida. No només m'ha fet ser qui soc com a científica i investigadora, sinó sobretot com a persona. Ha sigut un procés que ha requerit molt d'esforç i dedicació, però també m'ha aportat molts moments de satisfacció personal, i sobretot, persones que no oblidaré mai. Avui soc com soc i no d'una altra manera gràcies a tots vosaltres, que m'heu ajudat a créixer a nivell professional però també a nivell personal.

En primer lloc voldria mostrar la meva gratitud a l'Elena, la directora d'aquesta tesi. Primerament, per haver cregut en mi i haver-me volgut donar la oportunitat de fer la tesi doctoral al teu laboratori. Però sobretot, gràcies també per haver sigut sempre tan propera, fent que em sentís part de l'equip des del primer dia. Gràcies per haver-te mostrat sempre tan positiva i haver mostrat confiança en els meus resultats i en mi.

Jordi, gràcies per haver-me forçat a anar més enllà i analitzar profundament els meus resultats, penso que has aconseguit que elevés la qualitat d'aquest treball i, espero, desitjo, i crec, la meva qualitat com a científica. M'ha encantat poder analitzar i discutir junts els resultats (i això és quelcom que trobaré enormement a faltar), has estat una font inesgotable d'idees. Et considero un referent científic. Gràcies també per haver-me fet sentir tan valorada, per estar disposat sempre a escoltar-me i a ajudar-me.

Vane, gràcies per haver bolcat tots els teus coneixements de biologia en mi. Des del principi vas dedicar-me bona part del teu temps, ensenyant-me innumerables i complicades tècniques com l'aïllament de criptes i fibroblasts o el cultiu d'organoids, indispensables per aquesta tesi. Gràcies també per haver-me involucrat en el projecte de l'estudi del paper dels fibroblasts en la migració de les cèl·lules epitelials. Gràcies també per haver tingut aquesta actitud tan proactiva al laboratori, estant sempre disposada a ajudar a tothom a qui calgués al laboratori i preocupant-te perquè sempre hi hagués una bona dinàmica.

Gizem, you have been a true inspiration to me. I admire your scientific rigor and your complete dedication to research. I immensely enjoyed seeing how you function as a scientist and working with you. In between the hard work we put together, you also showed delicateness and kindness to me. You made me believe in myself and not let others step on me.

María, m'has aportat moltes coses tan a nivell científic com a personal. Al principi vas ser tu qui em va ensenyar a fabricar hidrogels amb el mask-aligner,

a muntar transwells i a tallar pilars amb el bisturí. Més tard, vam poder treballar colze a colze en el projecte de les criptes. I en aquest procés, mica en mica, hem anat teixint una amistat que espero no perdre mai.

Enara, no saps com d'agraïda estic d'haver-te trobat i compartir aquests anys amb tu. Crec que costa molt trobar persones amb les que t'hi entenguis tan bé. Juntes hem fet créixer els millors organoids que mai ningú hagi vist, i a la vegada, hem crescut nosaltres. Estic molt contenta d'haver pogut compartir amb tu la manera de fer ciència, sent conscients i meticuloses en tot el que fem.

Vero, ja saps que soc una persona que necessito el meu espai. Tanmateix, de tan còmode que estava amb tu, molt sovint decidia compartir cabina amb tu. I ara que no hi ets, sento que em sobra espai.

Núria, gràcies per estar sempre disposada a ajudar-me, a mi i a tothom. Anna, gràcies per sempre tenir bones paraules per mi i donar-me confiança en mi mateixa. Marta, gràcies per escoltar-me, m'hagués agradat treballar juntes, crec que haguéssim fet un molt bon equip. Jon, gràcies per fer-me companyia els primers mesos de la meva tesi, ens vam ajudar mútuament i a la vegada ens ho vam passar molt bé. Raquel Alonso, gràcies per haver portat alegria i humor al laboratori, ets una gran científica.

Melika, Angela, and the newcomers (Marcel, David, Aitor and Patricia) thank you for making the lab a more welcoming and friendly place and scientifically enriching it.

Voldria també mostrar el meu més sincer agraïment a tots els científics fora del meu grup de laboratori amb els que he tingut l'oportunitat de col·laborar: en primer lloc, a l'Anna Esteve, del CNAG-CRG, per haver-nos ajudat a analitzar els resultats de single cell RNA sequencing dels fibroblasts intestinals primaris; a l'Emilio Gualda, de l'ICFO, per ajudar-nos a la Gizem i a mi a fer tots els experiments de light-sheet fluorescence microscopy; al Xavier Hernando i a l'Eduard Batlle (IRB), per haver-nos donat els intestins de ratolins i a l'Anna Lladó i al Nikolaos Giakoumakis, de l'Advanced Digital Microscopy de l'IRB, per haver-me donat tot el suport tècnic per adquirir imatges dels hidrogels microestructurats de GelMA-PEGDA amb el microscopi Nikon Lipsi.

Gràcies també a la Giulia, l'Ignasi, la Marina, el Marc, l'Albert, el Miquel, la Cèlia, l'Ona, el Gerardo i a la resta d'estudiants de doctorat de l'Ibec per haver compartit penes als passadissos però també moments de diversió als PhD retreats, calçotades o bowlings.

També voldria dedicar unes paraules d'agraïment a totes les persones que formen part de la meva xarxa de suport fora del laboratori.

En primer lloc, als meus pares, Alícia i Miquel, per haver volgut sempre el millor per mi i per haver-me educat en ser una persona aplicada, responsable i treballadora, sense vosaltres no estaria aquí. Gràcies també a la resta de la meva família, sobretot als meus avis, Glòria i Ferran, i als meus iaios, Damiana i Vidal, per creure sempre amb mi molt abans que jo ho comencés a fer.

Ricard, gràcies per haver estat al meu costat durant tot aquest temps, des del principi fins al final. Sé que hi ha hagut moments durs, però tu mai has dubtat en posar-me totes les facilitats perquè jo pogués tirar endavant. Gràcies per haver-te adaptat a mi en tot moment i per haver-me estimat incondicionalment. Has estat el pilar més important en la meva vida i en aquesta tesi.

Marta, Cris, Berta, Helena, Anna, Meri i Alba, em sento immensament afortunada de tenir-vos, sou el meu refugi etern.

Table of contents

Abstract

The standard *in vitro* model of the small intestine in the field of drug development still consists in a monolayer of cancer-derived cells seeded on a hard substrate. Despite the huge advances that this model has provided, it does not faithfully recapitulate the complexity of the native tissue. Recently, the long-term culture of primary intestinal epithelial cells has been achieved through intestinal organoids, self-organizing 3D structures retrieving many of the features of the native tissue. Yet, they still have some limitations: (i) they are closed structures whose apical side is difficult to access, (ii) to grow, they require to be embedded in a highly heterogeneous matrix where well-controlled gradients of biochemical factors cannot be established, (iii) despite recapitulating the native cell compartmentalization, they do not retrieve the dimensionality of the tissue and (iv) they do not include the stromal compartment (mainly fibroblasts), proven to be key to maintain the intestinal stem cell niche. Therefore, the general objective of this thesis is to contribute to the development of complex *in vitro* models of intestinal epithelium focusing on the incorporation of the input of the stroma.

In the first section of this thesis, we successfully adapted an in-house developed photolithography-based technique to fabricate poly(ethylene glycol) diacrylate (PEGDA)-based hydrogels with crypt-like cavities. Although the nature of the chemical reaction used yielded partially-crosslinked polymer trapped in the cavities, the fabricated hydrogels could be functionalized with collagen I and organoid-derived epithelial monolayers could be formed on top.

In the second section of this thesis, we have developed an *in vitro* model that allows the culture of organoid-derived cells on hydrogels with villus-like architecture under gradients of the ISC niche. The fabricated hydrogels showed native tissue-like elasticity and microstructures resembling those of the native villi. The mesh size of the hydrogels allowed the diffusion of the factors of the ISC niche through the hydrogel, which formed stable gradients along the villus vertical axis. An *in silico* model of protein diffusion through the hydrogel was developed to predict the profiles of the gradients of the factors of the ISC niche. Organoid-derived single cells seeded on collagen I-functionalized hydrogels formed complete monolayers. Only under gradients of the ISC niche factors, as opposed to uniform concentrations, the monolayers displayed native-like cell compartmentalization. Finally, organoid-derived cells cultured under gradients that promote more the proliferation showed faster growth dynamics but also a depletion of the proliferative pool. Altogether, these findings demonstrate that our villus-like 3D intestinal epithelial model retrieves native-like cell compartmentalization under appropriate gradients of ISC niche factors. The *in vitro* model presented here could be used to systematically screen gradients of

factors, of particular interest those secreted by fibroblasts, and study the cellular response.

In the third section of this thesis, we aimed to study if intestinal fibroblasts have a physical role in epithelial cell migration under non-pathological conditions. Through the coculture of fibroblasts with intestinal organoids, we found that the paracrine signalling from the fibroblasts induced a cystic morphology in the organoids, whereas their physical presence triggered their expansion into 2D monolayers. This physical effect of fibroblasts leading the expansion of epithelial cells was also observed in a 2D engineered coculture *in vitro* model. Organoid-derived monolayers exposed to a cell-free space (gap) migrated directionally towards the gap and fully closed it. During this process, fibroblasts were found to also migrate but towards the monolayers, align perpendicularly to the migration front and produce equally oriented ECM proteins that might be used for epithelial cells to migrate directionally. Under only the paracrine signalling from fibroblasts, epithelial monolayers did not migrate that efficiently nor fully closed the gaps. Under no fibroblast input, epithelial cells migrated randomly and could not recover their integrity. All in all, we could demonstrate that fibroblasts are indispensable for epithelial integrity restoration under non-pathological conditions in a 2D coculture in vitro model.

Given the physical role of fibroblasts on the epithelial tissue, in the fourth section of this thesis we aimed to develop an *in vitro* model that incorporated a lamina propria mimicking compartment, together with the epithelial tissue, all the while recapturing the native architecture. To do so, we employed an in-house developed 3D printing technology to fabricate flat and villus-like gelatine methacryloyl (GelMA)-PEGDA hydrogels. First, using flat hydrogels, embedded fibroblasts were shown to be viable, have proliferation capacity and spread over the hydrogel surface. Organoid-derived epithelial cells seeded on top could only grow and form monolayers when fibroblasts were embedded within the GelMA-PEGDA hydrogels. In villus-like hydrogels, fibroblasts not only migrated to and spread on the surface, but they preferentially located at the tips of the villus-like microstructures. Organoid-derived single cells seeded on top of grew mainly at the tips and bases of the hydrogels. In these cocultures, fibroblasts migrated to the regions where epithelial cells were growing, mainly the tips and the bases of the hydrogels. Finally, fibroblasts cocultured with epithelial cells had their nuclei more elongated than when cultured alone, indicating a physical communication between the two cell types. Overall, we developed an *in vitro* model that mimics the native tissue architecture and encompasses not only the epithelium but also the mesenchymal compartment. Through this platform, we have unveiled a bidirectional communication between epithelial cells and fibroblasts.

Abbreviations

2D	Two dimensional
3D	Three dimensional
AA	Acrylic acid
α-SMA	α-Smooth muscle actin
AU	Airy Unit
BMP	Bone morphogenetic protein
BSA	Bovine serum albumin
Caco-2	Colon carcinoma cell line
CK20	Cytokeratin 20
DAPI	4',6-diamidino-2-phenylindole
DLP-SLA	Digital light processing stereolithography
DMEM	Dulbecco's modified eagle medium
E-cadherin	Epithelial cadherin
EthD-1	Ethidium homodimer
ECM	Extracellular matrix
EGF	Epidermal growth factor
F-Actin	Filamentous actin
FBS	Fetal bovine serum
GelMA	Gelatine methacryloyl
GFP	Green fluorescent protein
HBSS	Hank's balanced salt solution
ISC	Intestinal stem cell
LAP	Lithium phenyl-2,4,6- trimethylbenzoylphosphinate
Lgr5	Leu-rich repeat-containing G protein-coupled receptor 5
Lyz	Lysozyme
MA	Methacrylic anhydride
MEM-NEAA	Minimum essential medium - non-essential amino acids solution
NHS	N-Hydroxysuccinimide
PBS	Phosphate buffered saline
PEG	Poly (ethylene glycol)
PEGDA	Poly (ethylene glycol) diacrylate
ROCK	Rho kinase
ROI	Region of interest
RT	Room temperature
SD	Standard deviation
SEM	Standard error of the mean
TA	Transit-amplifying
UV	Ultraviolet light
WD	Working distance
Wnt	Wingless/Int

1. Introduction

1.1. Principles of the small intestine epithelium

The small intestine is the organ within the gastrointestinal tract whose main function is to absorb nutrients and water. It consists of a large tube divided in three segments: the duodenum, the jejunum, and the ileum. The wall of the small intestine is composed of four layers: mucosa, submucosa, muscularis, and serosa (Figure 1.1). The mucosa, in its turn, is composed of three layers: the epithelium, the lamina propria, and the muscularis mucosae.

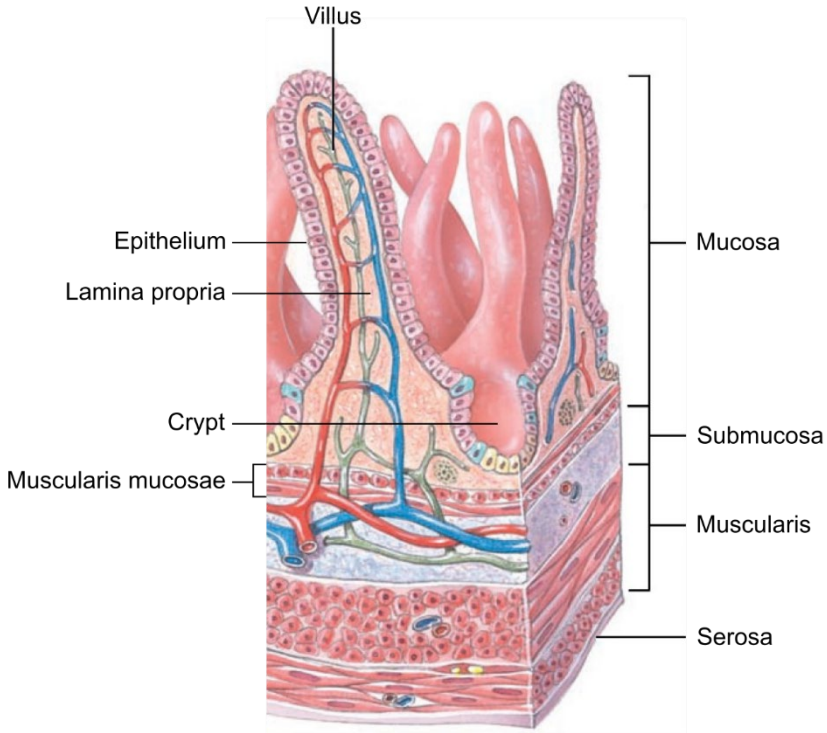

Figure 1.1. Drawing detailing the four layers of the small intestinal wall (right: mucosa, submucosa, muscularis and serosa), the layers of the mucosa (epithelium, lamina propria and muscularis mucosae) and the architecture of the epithelium consisting in villus and crypt units. Adapted with permission from Tortora et al.[1].

The epithelium is the layer in direct contact with the lumen and serves as a barrier to protect the tissue from the potential biological, chemical, and physical insults, such as pathogenic agents or mechanical stress. This simple rather than stratified columnar epithelium is not flat but has finger-like protrusions into the lumen called villi and invaginations into the lamina propria called crypts. The intestinal epithelium is composed of different cell types which are spatially

compartmentalized and serve different functions. In the bottom of the crypts is where the stem cells reside, intermingled with Paneth cells, a secretory cell type key for the formation and maintenance of crypts through the secretion of Wnt3a[2]. The stem cells (Lgr5$^+$) give rise to transit-amplifying (TA) cells, a highly proliferative population that yields all the differentiated cell types while migrating up along the villi (Figure 1.3). At the tips of the villi, cells undergo apoptosis and are shed off into the lumen. Historically, it was thought that this cell turnover, which is one of the fastest in our body (3 to 5 days), was fuelled by the mitotic pressure originated from cell division within crypts[3]. However, inhibiting mitosis in mice did not impair migration[4,5], suggesting the possibility of an active migration of epithelial cells. In this context, employing a biophysical model and quantitative three-dimensional (3D) tissue imaging, a report recently unveiled the existence of an active migratory force dependant on the actin-related protein 2/3 complex within the villi[6]. Thus, this study rejects the hypothesis that mitotic pressure is the only and main driving force for epithelial migration, and it limits this phenomenon to the crypts and lower regions of the villi (Figure 1.2 (a)).

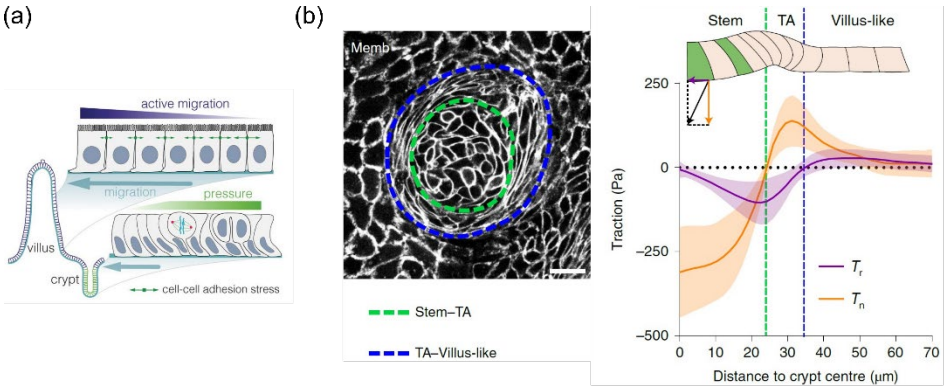

Figure 1.2. (a) Mechanical model for epithelial migration in the small intestine. Adapted with permission from Krndija et al.[6]. (b) (Left) Illustration of the boundaries between the stem cell compartment and transit amplifying zone (green), and the transit amplifying zone and villus-like domain (blue). Scale bar: 20 μm. (Right) Circumferentially averaged normal (Tn) and radial (Tr) tractions as a function of the distance to the crypt centre. The blue and green dashed lines indicate the radii where Tn and Tr, respectively, are zero, which closely correspond to the boundaries between the functional compartments illustrated in (Left). Adapted with permission from Pérez-González et al.[7].

Indeed, this spatial segregation of the main mechanism driving epithelial migration has been recently linked to a mechanical compartmentalization of the intestinal epithelium[7]. In an *in vitro* study, the stem cell-like compartment has been shown to push downwards the extracellular matrix (ECM) and fold through cell apical constriction, whereas the transit amplifying zone pulls upwards the ECM and elongates through cell basal constriction (Figure 1.2. (b).

Conversely, villus-like regions were found to exert positive forces radially, in line with the active migration described before[6]. This study[7] was able to reveal the existence of mechanical compartments linked to cell type compartments for the first time by employing an *in vitro* model that did not take into account the three-dimensionality of the native tissue. However, the characteristic architecture of crypt-villus units serves two fundamental functions: the high aspect ratio of villi allows the maximization of surface absorption, whereas the narrow and invaginated crypts serve to protect stem cells. Moreover, the overall topography allows a sharp spatial compartmentalization of cell proliferation in the crypts and cell differentiation in the villi.

1.2. Signalling pathways regulating the intestinal epithelium compartmentalization

The maintenance of the intestinal stem cell (ISC) niche and thus, the overall epithelial tissue homeostasis, is tightly regulated by signalling gradients of Wnt proteins, bone morphogenetic proteins (BMP) and epidermal growth factors (EGF) (Figure 1.3), as well as Notch lateral inhibition and Eph/ephrin repulsive interactions. The Wnt signalling gradient expands from the bottom to the top of the crypts and maintains the stemness and proliferation within them. In detail, in the Wnt canonical pathway, Wnt factors specifically secreted by Paneth cells[2] and fibroblasts[8,9] engage with the Frizzled Lrp5/6 co-receptors, triggering the stabilization of β-catenin, otherwise degraded by the proteasome. Then, β-catenin binds to the transcription factor Tcf4, which activates the genetic program associated to cell stemness and proliferation. In contrast, the counter-gradient of BMP present along the crypt-villus axis ensures the proper differentiation of TA cells into enterocytes, goblet cells or enteroendocrine cells up in the villi, mainly by repressing the expression of stemness genes[10]. EGF signals exert strong proliferative effects upon binding to their receptors (EGFRs)[11] that activate signalling cascades such as the Ras/mitogen-activated protein kinase (Ras/MAPK) pathway and phosphatidylinositol 3-kinase (PI3K)/AKT[12–14]. The Notch-Delta receptor-ligand signalling has a dual essential role: to direct the secretory cell fate and to maintain the undifferentiated state of the stem cells. In detail, the interaction between ligand and receptor in neighbouring cells leads to the liberation of the Notch intracellular domain (NICD). Once released, NICD translocates into the nucleus and induces the expression of target genes. When Notch is blocked in stem and TA cells, these differentiate into secretory lineage cells, either goblet, enteroendocrine or Paneth cells[15]. Instead, when Notch is on, stem and TA cells differentiate into absorptive cells, namely, enterocytes. Moreover, repulsive bidirectional interactions between Eph receptors and ephrin ligands also control cell

positioning along the crypt-villus axis[16]. Proliferative cells within crypts express EphB receptors in a increasing gradient from the bottom to the top of the crypts, whereas ephrinB ligands are expressed in all cell types in an decreasing gradient from the top of the villi until the bottom of the crypts[16,17].

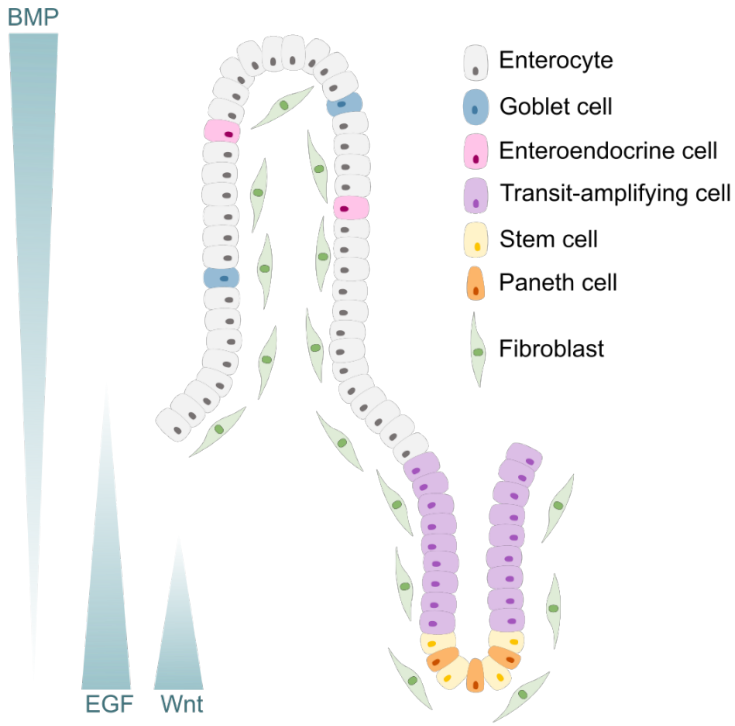

Figure 1.3. Schematic representation of the intestinal epithelium crypt-villus unit. Stem cells are localized at the bottom of the crypts, in between Paneth cells. Upper in the crypt there are the transit-amplifying cells, who, while migrating up towards the tip of the villus, differentiate mainly into enterocytes, goblet cells and enteroendocrine cells. Beneath the epithelium, in the lamina propria, there are specialized fibroblasts. BMP, EGF and Wnt signalling gradients along the crypt-villus axis regulate the overall tissue homeostasis.

In sum, the five signalling pathways (Wnt, BMP, EGF, Notch and Eph/ephrin) act in concert to maintain the ISC niche while driving cell renewal, thus ensuring tissue homeostasis. Wnt, BMP and EGF act as signalling gradients of diffusive molecules whereas Notch and Eph/ephrin are more localised signalling.

1.3. Mesenchymal cells of the lamina propria

Underneath the epithelium monolayer there is the basement membrane, a thin sheet of specialised extracellular matrix composed mainly of type IV collagens, laminins and proteoglycans[18]. The basement membrane separates the

epithelium from the lamina propria, a highly vascularized connective tissue composed of extracellular matrix (ECM) proteins, mainly collagens, and stromal or mesenchymal cells, including immune cells, pericytes, smooth muscle cells, mesenchymal progenitors, and fibroblasts[19,20]. During development, the mesenchyme has an essential role in shaping the epithelium. As it differentiates into the different smooth muscle layers, a process that only takes 48 hours, villi emerge[21,22]. Along with this process, there is also a remodelling of the ECM; for instance, at the top of the developing villus, fibronectin and pro-collagen III expression starts to diminish until eventually disappearing[23]. The maintenance of the intestinal shape by mesenchymal cells through ECM remodelling is continued during adulthood. In detail, mesenchymal cells, a term that, after development, is used to refer to all the cells that are non-hematopoietic, non-epithelial, and non-endothelial within connective tissues, produce type I, II, and V collagens, proteoglycans, glycoproteins such as laminin, fibronectin or nidogen as well as matrix remodelling enzymes such as matrix metalloproteinases[20,24]. Aside from physically supporting the epithelium by providing a scaffold during development and maintaining it across adulthood, mesenchymal cells have also been implicated in preserving the immune homeostasis of the epithelium. In detail, they have been reported to have the ability to sense bacterial damage-associated and inflammatory signals, and secreting several cytokines (IL-1, IL-6R and IL-8R, among others), growth factors such as TGF-β or other inflammatory mediators such as prostaglandins as a result. These factors, in turn, guide leucocyte migration into, within and out of the intestine[25]. Last but not least, recent studies reported an essential role of mesenchymal cells in maintaining the epithelial stem cell niche. Historically, Paneth cells had been regarded as the gatekeepers of the ISC niche through the secretion of Wnt3a, EGF, Notch ligands. However, while knocking out Tcf4 (the transcription factor that activates the genetic program associated to cell stemness and proliferation) in embryonic intestinal epithelial cells impaired their proliferation[26], the knock-out of Wnt3a or the depletion of Paneth cells did not alter the normal physiology of the intestinal epithelium[8,27], suggesting the existence of other epithelial and non-epithelial cells contributing to the ISC niche by secreting redundant Wnt factors.

1.4. Intestinal fibroblasts

Later it was found that Wnt2b, which is secreted by intestinal fibroblasts, could rescue intestinal growth in the absence of Wnt3a[8]. Upon this breakthrough, several studies have shown that these subepithelial fibroblasts support the growth of the intestinal epithelium *in vitro*[28,29] and the maintenance of the tissue homeostasis through, not only the secretion of Wnt2b[8], but also of R-

spondins[28,30], which act as Wnt amplifiers, BMP agonists and antagonists[31–34] and EGFR ligands[35]. Within the intestinal subepithelial fibroblasts, there exist different populations according to several variables: their morphology, the markers they express, the factors they secrete and their localization within the crypt-villus axis. Even though the expression of no niche factor is restricted to a single cell cluster (Wnt2b, for instance, is expressed in diverse cell types) and there is redundancy among ligands and antagonists, the current accepted classification is the following (Figure 1.4). Telocytes, or previously called subepithelial myofibroblasts (SEMFs) are mainly localized at the villus base and at the tip. They display protrusions that can extend hundreds of micrometers and express several BMP agonists as well as Wnt4 and Wnt5a, usually acting as non-canonical Wnt factors. Trophocytes localize between crypts and the muscularis externa and express Wnt2b, R-spondin1-3 and the BMP antagonist Grem1, among others. Platelet-derived growth factor receptor alpha low ($PDGFRA^{low}$) stromal cells, or historically called, interstitial fibroblasts, constitute a large and heterogeneous population characterized by expressing PDGFRA at lower levels than telocytes. They secrete Wnt2b, R-spondin2, BMP agonists, mainly Bmp2, and Wnt antagonists, mainly Dkk3 and Sfrp1.

In the same way that intestinal fibroblasts play a key role in maintaining the integrity and function of the intestinal epithelium, they are also often involved in pathological conditions. For instance, in diseases such as Crohn's, the local inflammation damages the intestinal epithelium, and this leads to the formation of ulcers or wounds. During the first phase of epithelial regeneration, the so-called restitution, epithelial cells migrate to cover the wounded area and restore the integrity of the barrier. It has been extensively demonstrated that transforming growth factor (TGF)-α and TGF-β, epidermal growth factor (EGF), hepatocyte growth factor (HGF) and fibroblast growth factor (FGF), among others, enhance restitution of intestinal epithelial cells via what is known as the TGF-β-dependent pathway[36]. Interestingly, several reports have shown that intestinal fibroblasts secrete these factors[37,38], thus clearly evidencing the importance of the fibroblasts' paracrine signalling not only in homeostasis but also in disease. Studies carried out in epithelia other than the intestinal such as the skin[39] or the cornea[40,41], indicate that, upon injury in the epithelial barrier, fibroblasts get activated in response to mechanical stress and transforming growth factor β1 (TGF-β1) signalling. They have been shown to deposit collagen and express metalloproteases further contributing to the tissue matrix remodelling. Importantly, these fibroblasts display stress fibbers that exert contractile forces that are directly transmitted to the ECM and induce the closure of the wound[42]. However, it remains to be investigated whether (i) there is a direct physical interaction between epithelial cells and fibroblasts, (ii) these

mechanisms occur in the intestinal epithelium, and (iii) if they happen not only in pathological conditions but also in homeostatic state. It has been recently discovered that cells within intestinal villi migrate actively towards the tip, rather than being pushed by the cells below upon their division (i.e. through mitotic pressure). Yet, if the underlying fibroblasts have any role, either paracrine or physical, has not been studied yet. To the best of our knowledge, the only study that addressed this question did so by performing experiments *in vitro* using an epithelial cell line derived from a colon carcinoma[43]. They found that wound repair was more efficient in the presence of fibroblasts, but they did not go further in investigating the mechanism. **In this context, one of the objectives of this thesis is to study if fibroblasts have a role in the migration of epithelial cells in homeostatic conditions.**

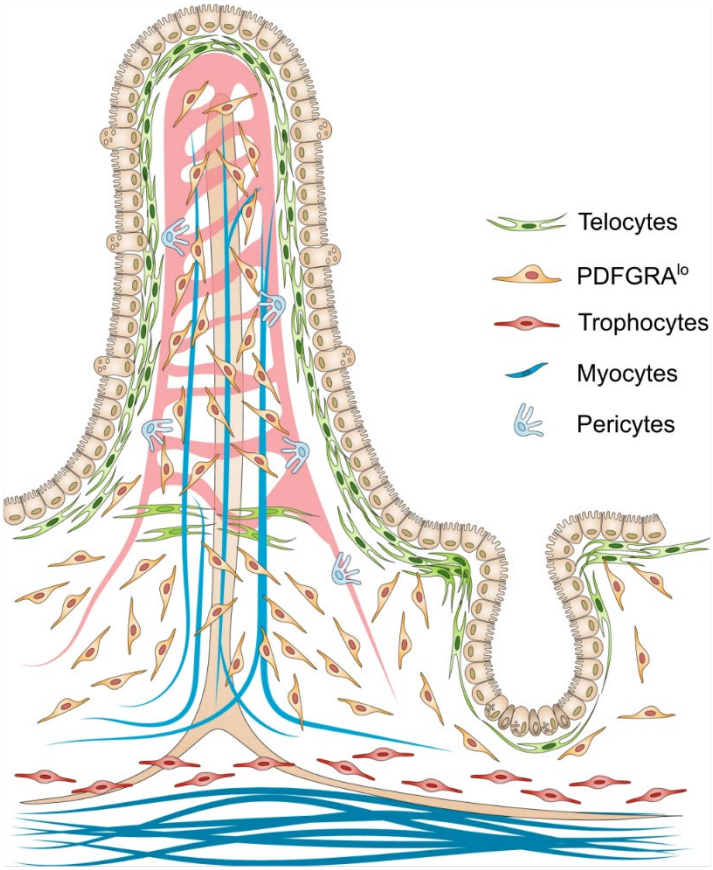

Figure 1.4. Mesenchymal populations within the small intestine. Telocytes or subepithelial myofibroblasts (SEMFs) localize mainly at the villus bases and also at the tips. Scattered all over the lamina propria there are PDGFRA^{low} cells. Underneath the crypts, right above the muscularis externa, there is a third population of fibroblasts called trophocytes. Adapted with permission from McCarthy et al.[33].

1.5. Standard *in vitro* models of the intestinal tissue

Still, most of the current knowledge of the intestinal physiology and dynamics has been gained using animal models. However, recently there have been efforts to reduce their use because of economic and ethical reasons, both in the academics and industry research fields. Naturally, this has caused the emergence of alternative models, mainly *in vitro* ones.

Because the small intestine is the organ in charge of absorbing nutrients and water, there was an even greater urge to develop *in vitro* models of this tissue to study the absorption, permeability, transport, and efficacy of potential drugs. Moreover, the simple yet well-structured nature of this tissue, as well as its fast turnover, make it an excellent framework to study stem cell biology.

The gold standard model in the field of drug development is still nowadays a monolayer of Caco-2 cells cultured on a collagen-coated polycarbonate membrane within a Transwell® insert[44]. Although this platform has been useful for many studies[45–47], Caco-2 is a cell line derived from a human colon adenocarcinoma and has been reported to display non-physiological features such as differentially expressed enzymes and transporters or an increased transmembrane electrical resistance, a property routinely measured to evaluate the barrier function of the epithelium[47] . Additionally, the substrate onto which they are grown does not faithfully recapitulate the native ECM as it consists in a polymeric stiff membrane that does not provide the mechanical nor the biochemical features of the tissue. In this context, novel materials with ECM-like properties such as hydrogels have been shown to improve the properties of *in vitro* cell-based models. Hydrogels consist of hydrophilic polymers that form 3D networks upon chemical or physical crosslinking. They have a huge capacity to uptake high amounts of water without dissolving, a property called swelling, which allows the diffusion of nutrients and oxygen. Their high water content also confers them elastic modulus values that can resemble that of soft tissue microenvironments (<40 kPa) as in the case of small intestine[49].

1.6. Hydrogels as biomimetic cell culture materials

Hydrogels can be of natural or synthetic origin. Natural materials inherently offer cell adhesion cues, but they are also subjected to biodegradation, thus allowing matrix remodelling but at the same time rendering them prone to mechanical instability. Among the most used natural hydrogels is Matrigel®, a mouse sarcoma - derived matrix composed mainly of laminin and collagen IV, together with growth factors, that has proven to be the only matrix able to

sustain functional culture of intestinal stem cells (see later). However, because of its natural origin, it offers high batch-to-batch variability, and it is not very well characterized. Moreover, it displays poor mechanical stability, thus hindering their use for long term studies. Indeed, to increase their stiffness, Matrigel has been frequently mixed with collagen I. Collagen I-only hydrogels have also been proposed, and, although they are more robust, they are still highly prone to degradation and shrinking. Denaturalized collagen, gelatine, has started to be used as it is a cheaper alternative to collagen that maintains the positive features of collagen (biocompatibility, bioactivity, biodegradability, and low antigenicity). Moreover, by reacting gelatine with methacrylic anhydride (MA), one can chemically substitute the free amino groups of the lysines and hydroxilysines, and some hydroxyl groups by the acryloyl groups of the methacrylic anhydride (MA) to obtain gelatine methacryloyl (GelMA), a polymer able to photocrosslink in the presence of a photoinitiator and light exposure. Still, mechanical and biochemical cues of natural based hydrogels cannot be easily tuned and thus are not suitable for certain tissue engineering applications. Moreover, they are subjected to possible unspecific interactions between the diffusing molecules and their 3D mesh, like in the case of rapidly absorbed hydrophobic drugs[50], a drawback when aiming to recreate the chemical gradients present in the native intestinal tissue. Conversely, synthetic hydrogels can be designed to offer the exact chemical composition needed as well as the mechanical properties, although time and - bioinert, they require to be functionalized with natural based cell adhesion ligands to be biocompatible. Among the synthetic polymers used for hydrogel formation, poly(ethylene glycol) (PEG) is the most extensively utilized material in biomedical applications. It can be fabricated with a wide range of stiffnesses (E ≈ 3–1000 kPa[51]) to better mimic the elasticity of soft tissues. Indeed, PEG-based hydrogels functionalized with cell adhesion cues have been proposed as alternatives to the ill-defined matrix Matrigel[52], employed in the culture of organoids, sophisticated cell organotypic models that have revolutionized the culture of stem cells *in vitro*.

1.7. Intestinal organoids

By embedding intestinal stem cells (ISCs) in Matrigel, a matrix rich in laminin, and culturing them with the suitable biochemical factors (EGF, R-spondin and Noggin), Sato and colleagues managed to make them grow and develop into 3D structures, called intestinal organoids, containing crypt-like regions, defined by the presence of $Lgr5^+$ stem cells, and villus-like regions[53] (Figure 1.5).

Since the establishment of intestinal organoids, numerous studies have contributed to gain precious knowledge about them. For instance, it has been unveiled that single stem cells have the intrinsic capability to self-organize resulting first in symmetrical spheres containing cell-to-cell expression variability in YAP1, which in turn, initiate Notch and DLL1 activation, ultimately giving rise to a symmetry-breaking event and the formation of the first Paneth cell. Interestingly, in an attempt to develop a synthetic and well-defined matrix to culture intestinal organoids, researchers found that stem cells required fibronectin- or arginine-glycine-aspartic acid (RGD) peptide-based adhesion and a stiffness of ~1 kPa to expand, whereas to differentiate and form a mature organoids, they required laminin-based adhesion and a stiffness of less than 0.2 kPa[52]. Intestinal organoids have been extremely useful for studies of basic biology and development of the intestine, *in vitro* screening of drug candidates, and functional engraftments for regenerative medicine[54–57].

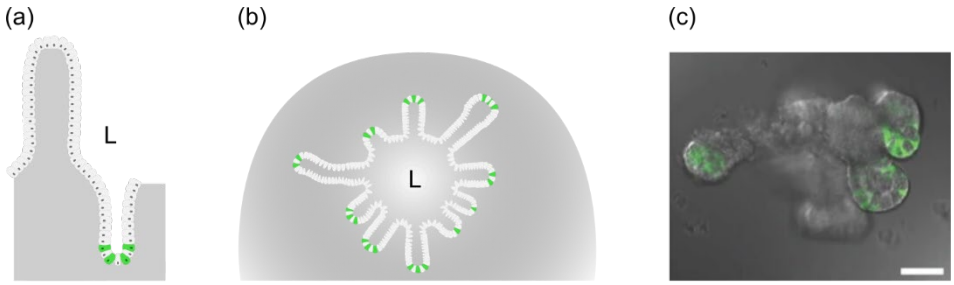

Figure 1.5. (a) Schematic representation of the small intestine morphology. The intestine is lined with a single layer of epithelial cells organized into villus and crypt domains. Lgr5$^+$ stem cells (in green) are localized at the bottom of the crypts. (b) Schematic representation of an intestinal organoid, consisting of a central lumen (L) lined by villus-like domains and crypt-like domains, characterized by the presence of Lgr5$^+$ stem cells (in green). (c) Representative image of an intestinal organoid (14 days after the embedding of a single stem cell) overlapping bright field and GFP fluorescence signals, corresponding to the Lgr5-GFP$^+$ stem cells, localized at the bottom of the crypt-like domains. Scale bar: 50 μm. Adapted with permission from Sato et al.[53].

However, despite their huge usefulness for certain applications, organoids also display several drawbacks. First, they are stochastically developing tissues, therefore exhibiting great morphological variability between them. This inherent heterogeneity scales up by the fact that they require to be embedded in Matrigel, an animal-derived matrix with high batch-to-batch variability. This, in turn, prevents the spatiotemporal control of diffusive factors present in the cell culture medium, therefore hindering their applicability to study the role of biochemical gradients in the tissue homeostasis, restoration upon injury or cancer. Moreover, although they contain compartmentalized proliferative and differentiated regions, the latter ones (the villi), are underrepresented and their

native topography is not retrieved. In addition, despite containing most of the epithelial cell types found in the *in vivo* tissue, they do not accommodate for the mesenchymal cells present in the lamina propria known to have an essential role in tissue homeostasis. Finally, they have a closed architecture that prevents an easy access to the apical side, which is a fundamental feature for most applications including apical-to-basolateral transport studies, host-microbiome interactions and drug absorption tests.

1.8. Organoid-derived intestinal monolayers

Precisely in an effort to allow an easy access to the apical side, several groups have managed to "open-up" the 3D organoids into 2D monolayers[7,58–60]. Either organoid-derived single cells or crypts were seeded on top of Matrigel-coated surfaces[59,60] or polyacrylamide hydrogels functionalized with collagen type I and laminin[7] obtaining monolayers with all the relevant cell types and spatially disposed as the native tissue (in crypt- and villus-like regions) (Figure 1.6). The monolayers developed by Pérez-González *et al* in 2021 allowed to gain insight into the mechanical properties of the different compartments within the intestinal epithelium (Figure 1.6 (a)). The study by Thorne *et al*. in 2018[59] revealed that the morphogen-mediated feedback between Wnt and BMP signalling is sufficient for the epithelium to self-regulate and maintain its homeostasis (Figure 1.6 (b)).

Finally, in our laboratory, monolayers were smartly grown onto porous membranes in Transwell inserts, thus allowing an easy access to both the apical and the basal side, to, for instance, employ different cell culture media between the two chambers (Figure 1.6 (c)). Indeed, this property was used to basolaterally deliver conditioned medium from intestinal fibroblasts.

These experiments evidenced the key role of fibroblasts' paracrine signalling in the growth of intestinal epithelium, as these monolayers could be maintained for up to 20 days while displaying the barrier function of the native tissue and preserving their self-renewal properties, maintaining the spatial cell compartmentalization in crypt- and villus-like domains[60].

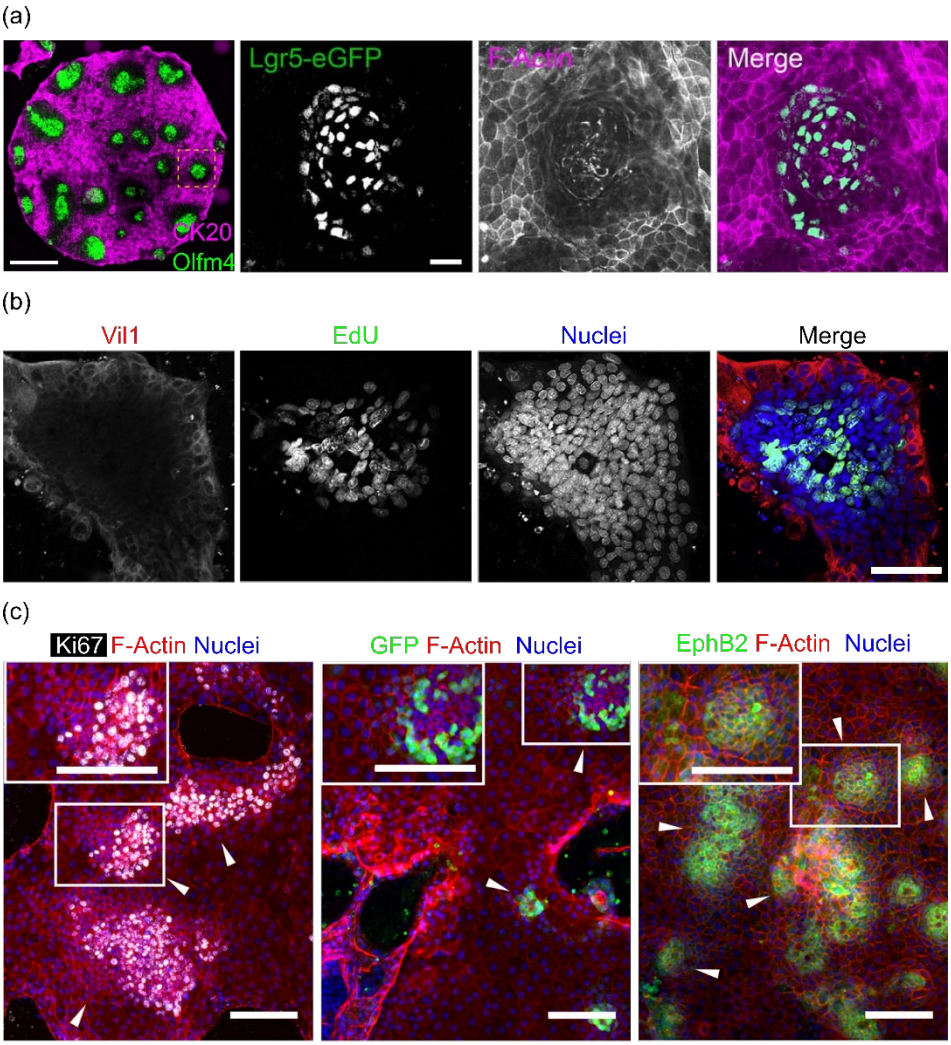

Figure 1.6. Compartmentalized organoid-derived monolayers on top of (a) soft polyacrylamide hydrogels displaying CK20 (differentiated cells) and Olfm4 (stem cells) (left panel), Lgr5-eGFP (stem cells) and F-Actin (three right panels). Scale bars: 200 μm. Adapted with permission from Pérez-González et al.[7]. (b) Matrigel-coated plates displaying Vil1 (enterocytes), EdU (dividing cells) and nuclei. Scale bars: 25 μm. Adapted with permission from Thorne et al.[59]. (c) Matrigel-coated polycarbonate membranes displaying Ki67 (proliferative cells), F-Actin and nuclei (left), GFP (stem cells), F-actin and nuclei and EphB2 (mainly crypt-like regions), F-actin and nuclei. Scale bars: 25 μm. Adapted with permission from Altay et al.[60].

1.9. *In vitro* intestinal models with *in vivo*-like 3D architecture

Despite the indisputable relevance of the 2D monolayer systems mentioned above, they do not recapitulate the 3D architecture of the small intestine, known

to spatially localize signalling gradients and, in turn, the different cell types. In this regard, huge efforts have been put in innovating in both microfabrication techniques and hydrogel materials to develop more physiologically relevant engineered tissues.

Replica moulding has been employed to create microstructured soft hydrogels using first a hard mould as a template. Sometimes, from this hard mould a second elastomeric polydimethylsiloxane (PDMS) stamp is first produced. Next, the PDMS stamp is put in contact with a photosensitive prepolymer solution and crosslinked (Figure 1.7)[61]. Finally, the resulting hydrogel is carefully demoulded. Indeed, because of the dimensions (between 130 and 330 µm in height[62] and around 60 µm in diameter[63]) and the high-aspect ratio of villi (height/diameter > 4[64]), this last step is particularly critical and hydrogels frequently get deformed or even broken.

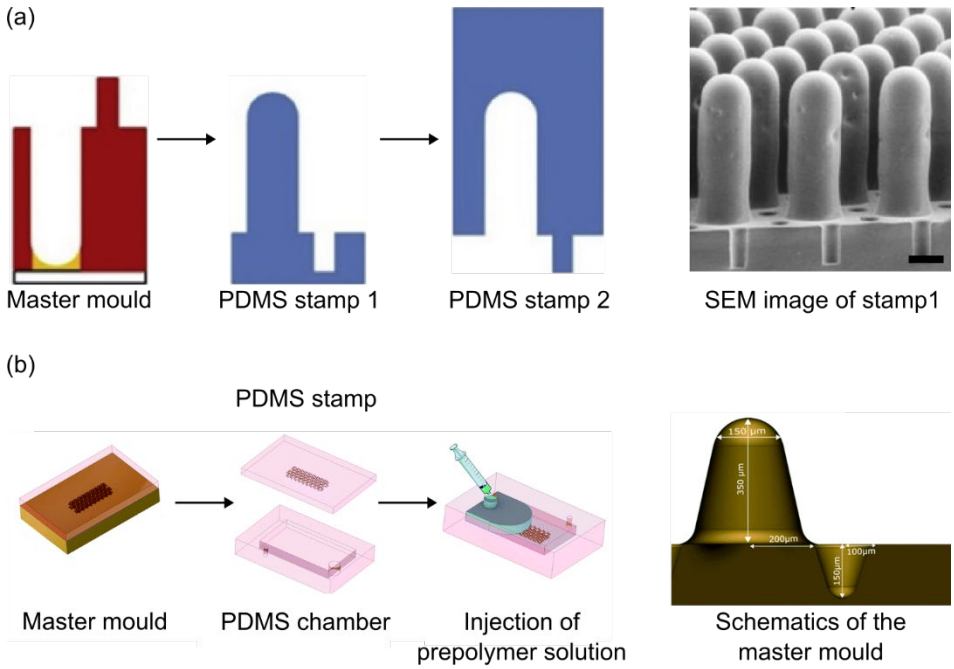

Figure 1.7. Schematic diagrams of examples of replica moulding processes followed to obtain collagen hydrogels with *in vivo*-like crypt and villus units. (a) Adapted with permission from Wang et al. [65]. Scale bar: 100 µm. (b) Adapted with permission from Verhulsel et al.[66].

To overcome this, moulds can be treated to decrease their stickiness or even, sacrificial moulds that can be dissolved in water-based solutions can be used[61]. Still, this renders replica moulding as a labour-intensive and complex technique. Several groups have employed replica moulding to microstructure collagen into hydrogels with *in vivo*-like crypt and villus units and culture intestinal primary

epithelial cells on top, either derived from human[65] or from mouse organoids[66] (Figure 1.7). While the use of collagen opened the way to embed cells within such as fibroblasts and thus include the lamina propria compartment[66], it also implied the degradation of the hydrogel. In the study by Verhulsel et al.[66], this limitation was attempted to be overcome by crosslinking the collagen with threose via glycation. Even though favourable results were obtained, shrinking was still to half of the original height of the scaffold. In another study, chemical crosslinking through N-(3-Dimethylaminopropyl)-N'-ethylcarbodiimide (EDC)/N-Hydroxysuccinimide (NHS) (EDC/NHS) was found to efficiently reduce the degradation[67]. However, cytotoxicity issues render this process incompatible with embedding cells within the scaffold.

Laser ablation has been historically employed as an alternative to photolithography and etching to fabricate the first mould in the replica moulding procedure. Yet, in a recent study, this technique was strategically used to generate microchannels mimicking the intestinal crypts within an already crosslinked hydrogel made of collagen I and Matrigel (Figure 1.8). Using this approach, they were able to engineer a planar chip with integrated flow that allowed the culture of mouse organoid-derived epithelial cells[68].

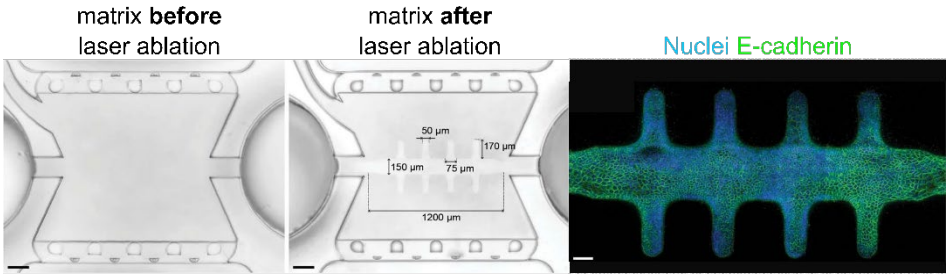

Figure 1.8. (a) Hybrid collagen I/Matrigel scaffold in the central chamber before and after microchannel ablation. Scale bars: 200 µm. (b) Fluorescence confocal image of a representative three-day old epithelial tube. Cells are labelled with DAPI (blue, nuclei) and E-cadherin (green). Adapted with permission from Nikolaev et al.[68].

Photolithography is another microfabrication technique that can be used to microstructure hydrogels. Briefly, a topological pattern is transferred on a light-sensitive polymer by placing a 2D photomask with the desired pattern consisting of transparent and opaque regions on top of the polymer and applying UV light (Figure 1.9 (a)). Photolithography thus poses as a much simpler approach compared to replica moulding.

Still, when employed with polymers that crosslink based on free-radical polymerization, the presence of oxygen renders the reaction kinetics difficult to control. However, our group recently showed how, by controlling fabrication

parameters such as the oxygen diffusion, the distance to the light source and the exposure time, villus-like microstructures with well-defined geometry and dimensions can be obtained[69] (Figure 1.9).

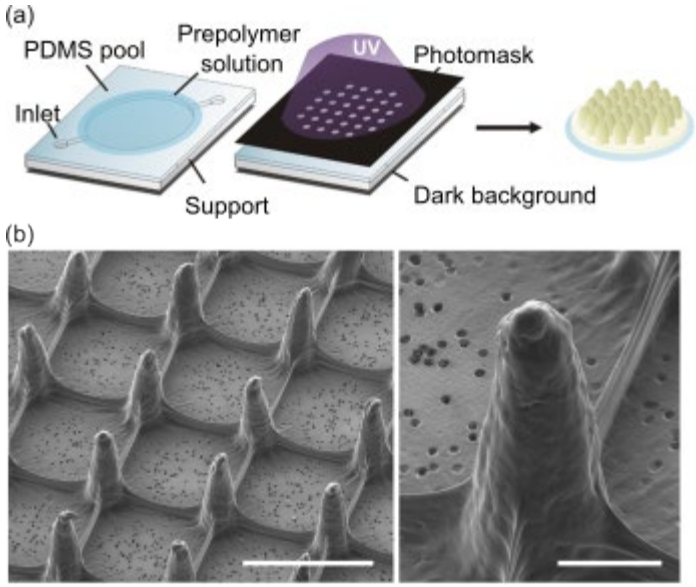

Figure 1.9. Schematic representation of the photolithography process. SEM images of hydrogel microstructures fabricated on a porous membrane (pores are seen at the base due to sample preparation process). Left: Scale bar = 200 μm. Right: Scale bar = 100 μm. Adapted with permission from Castaño et al.[69].

In this thesis, one of the aims has been to adapt this photolithography-based technique to obtain hydrogels with crypt-like microstructures, with the idea of producing hydrogels containing both villus- and crypt-like microstructures.

Another light-based fabrication technique is Stereolithography (SLA), a kind of 3D bioprinting technique that consists in the polymerization of prepolymer solutions (or bioinks) in a layer-by-layer manner upon the exposure of light from a laser beam (Figure 1.10). This technique allows the fabrication of high aspect ratio microstructures, although this will depend on the specific equipment as well as the polymer used. Using SLA, Creff *et al.* fabricated PEG-based hydrogels with crypt- and villus-like structures to engineer an *in vitro* model of the intestinal epithelium using Caco-2 cells[70]. However, these structures were fabricated from highly concentrated pre-polymer solutions (40% of macromer content) of short chain PEG-based polymers, thus making these scaffolds much stiffer than the native ECM of the tissue[70].

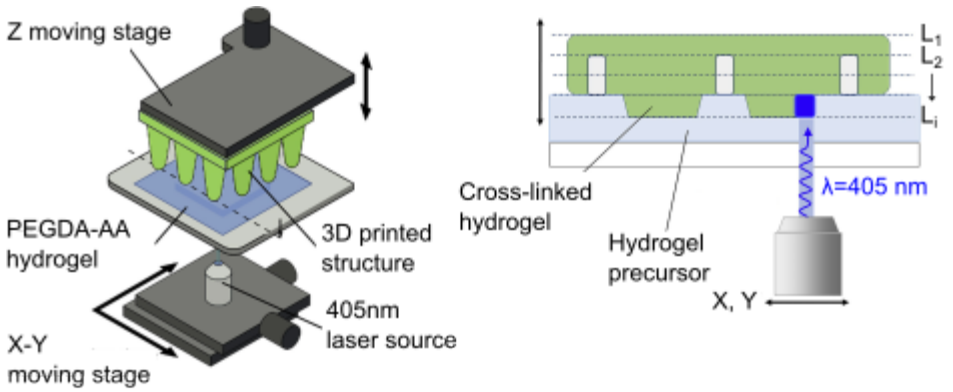

Figure 1.10. Schematic representation of the stereolithography process to fabricate 3D intestinal scaffolds containing crypt- and villus-like structures. Adapted with permission from Creff et al. [70].

Digital Light Processing (DLP) is another type of 3D bioprinting that resembles very much to stereolithography, but instead of using a raster scanning laser as a light source, it uses a projector, therefore rendering it a much faster and thus cell friendly, technique. In our group, we have very recently developed a customised DLP bioprinter that allows the successful fabrication of villus-like hydrogels with embedded cells (Figure 1.11). This technology has been proven to be compatible with the culture of cell lines, thus opening the way of creating intestinal models that include the epithelial and stromal compartments with the 3D *in vivo*-like architecture.

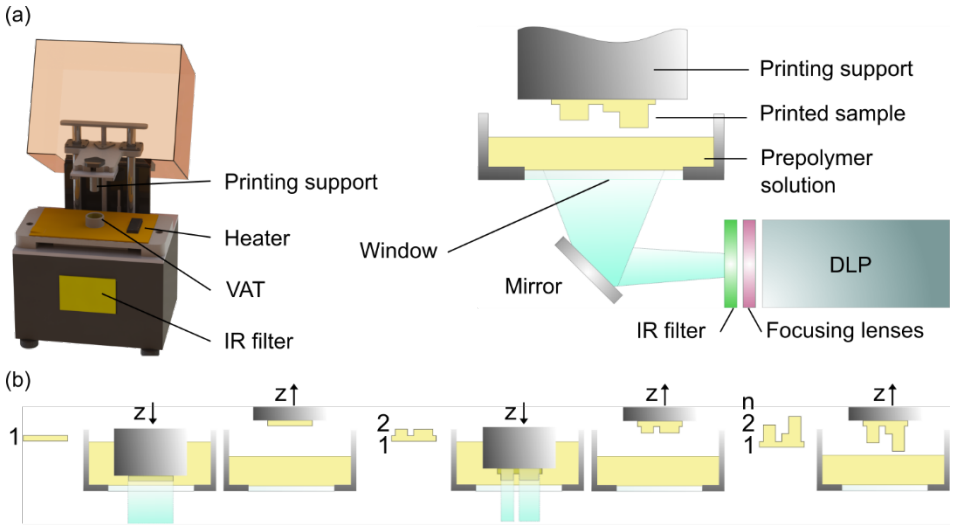

Figure 1.11. (a) Customized DLP-3D bioprinting system: 3D CAD model of the 3D bioprinter system (left) with detailed view of the main components (right). (b) Schematic representation of the DLP procedure. Adapted with permission from Torras et al.[71].

1.10. *In vitro* intestinal models with biomolecular gradients of the ISC niche

As mentioned above, gradients of ISC niche factors guide epithelial compartmentalization into proliferative crypt regions and differentiated villus regions. With the aim of elucidating the threshold concentrations that promote stem cell renewal, Ahmad and co-authors[72] engineered a device (Figure 1.12. (a)) where single colon-derived epithelial cells embedded in Matrigel developed into organoids while being exposed to gradients of Wnt-3a and R-spondin1 (Figure 1.12. (b)). With this strategy, they found out that the minimal concentrations allowing stem cell renewal and differentiation in colonoids (colon organoids) were of 60 ng mL^{-1} for Wnt-3a and of 88 ng mL^{-1} for R-spondin1. By diffusing a 40 kDa Fluorescein isothiocyanate (FITC)-Dextran, they characterized the gradients through fluorescence microscopy (Figure 1.12. (c)). However, because the hydrodynamic diffusion coefficients of proteins cannot be estimated in this highly heterogeneous matrix that is Matrigel, they were not able to estimate the actual protein concentrations that cells were seeing. Moreover, cells were cultured as organoids, thus not allowing the access to the apical side nor retrieving the 3D villus architecture. Later, researchers of the same group developed a microstructured collagen hydrogel where they cultured cell fragments from previously established human organoid-derived small intestinal epithelium monolayers[67] (Figure 1.12. (d)).

By applying gradients of Wnt3-a, R-spondin, EGF and Noggin from the bottom of the crypt up and a counteracting gradient of DAPT (gamma-secretase inhibitor) (Figure 1.12. (d, left panel)), the authors managed to engineer a 3D *in vitro* model of the human intestinal epithelium with *in vivo*-like cell compartmentalization (Figure 1.12. (d, middle and right panels)). Similarly, in another microfluidic device developed by the group of Matthias Lutolf[68], they could spatially compartmentalize proliferative cells and differentiated cells by using two different cell culture media in the basolateral side (promoting tissue expansion) and in the apical side (promoting tissue differentiation). However, because the fabricated hydrogels were made of collagen or collagen and Matrigel, both natural materials, their mesh size cannot be accurately estimated, which in turn impedes the study of how proteins diffuse within the hydrogels. Instead, the network of synthetic hydrogels can potentially be much easily characterized. Nevertheless, while PEG-based hydrogels with villus and crypt-like microstructures could be successfully fabricated through SLA bioprinting[70], the choice of low (700 Da) average molecular weight polymer, and thus small molecular weight between crosslinks prevents the potential diffusion of

molecules relevant for the maintenance of the ISC niche, as their size is larger than the hypothetic mesh size of such hydrogels.

In this regard, **one of the aims of this thesis is to engineer a PEGDA-based villus-like model of the intestinal epithelium using organoid-derived cells that allows the formation of gradients of the ISC niche.**

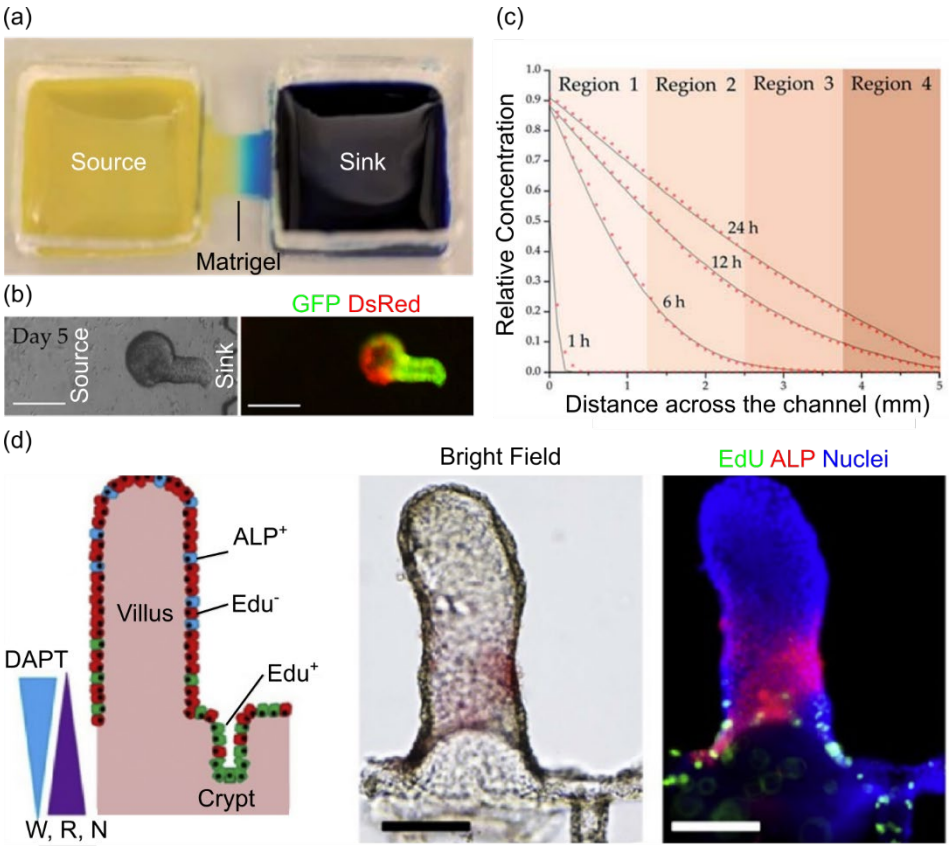

Figure 1.12. (a) Gradient generating microdevice. Adapted with permission from Ahmad et al.[72] (b) Brightfield (left panels) and fluorescence (right panels) images of GFP (GFP^+ cells corresponding to $Lgr5^+$ intestinal stem cells), and DsRed (actin) for colonoids growing from a single cell in the presence of a dual Wnt3a/R-spondin gradient. Scale bars: 50 µm. Adapted with permission from Attayek et al.[73] (c) Gradient characterization on the microdevice. Movement of a 40 kDa FITC-dextran through the channel was monitored using time-lapse fluorescence imaging. The experimentally measured data is marked as red stars. The solid black line is the fit to the data using Fick's Law. Adapted with permission from Ahmad et al.[72] (d) Schematic showing the application of a triple growth factor gradient (W: Wnt3-a, R: R-spondin1 and N: Noggin) with an additional counteracting gradient comprised of DAPT (gamma secretase inhibitor) (left). Brightfield (middle) and fluorescence (right) images of a polarized crypt-villus unit under the 3-growth factor gradient and opposing DAPT gradient. Mature enterocytes (ALP^+), non-proliferative cells (Edu^-) and proliferative cells (Edu^+) are displayed. Scale bars = 100 µm. Adapted with permission from Wang et al.[65].

1.11. *In vitro* intestinal models with stromal compartment

As stated above, intestinal fibroblasts underneath the epithelium have a major role in maintaining the ISC niche by the secretion of factors of the Wnt and BMP signalling pathways. Besides, upon damage, they respond by secreting cytokines and ECM proteins that allow the epithelium to quickly recover its integrity. Therefore, it seems only logical that to develop *in vitro* models that resemble as much as possible the native tissue, intestinal fibroblasts should be included. Few studies have attempted to develop such models due to the numerous challenges needed to be faced. First, the hydrogels used must have cell adhesion motives, either RGD cues within synthetic hydrogels such as PEG, or inherent in the polymer as in the case of natural ones such as collagen or Matrigel. The latter strategy has been the most extensively used so far. Nikolaev et al.[68] developed a Collagen I/Matrigel-based chip that allowed the coculture of organoid-derived single cells with non-epithelial cells such as intestinal fibroblasts (Figure 1.13 (a)). By doing so, they could see how the two cell types made physical contact. However, they did not go further into analysing this crosstalk and its effect on the epithelium, which we believe could be of high relevance. Moreover, intestinal fibroblasts were loaded through the apical side of the chip (empty space recreating the lumen), rather than through the basolateral one (Collagen I/Matrigel hydrogel), thus not truly mimicking the native spatial distribution of the two cell types. In another study by Verhulsel *et al.*[66], a collagen-based crypt-villus platform that allowed the embedding of primary intestinal fibroblasts was described (Figure 1.13 (b)). In this case, the intestinal fibroblasts were delivered through the basolateral side, as *in vivo*. However, because collagen is a natural hydrogel, the hydrogel suffered from severe shrinkage. The researchers could mitigate this phenomenon, which was accentuated upon the embedding of stromal cells, by crosslinking the collagen with threose, a sugar. Interestingly, they could successfully observe that the presence of fibroblasts resulted in a better segregation of the differentiated cells. Yet, they didn't perform any kind of test to analyse the functionality of the fibroblasts after the threose treatment and they appeared rather scarce and not well spread.

In our lab, we have found that the combination of natural and synthetic photocrosslinkable polymer solutions based on GelMA and PEG-based chains, respectively, provides hydrogels with good mechanical stability and compatibility with fibroblasts embedding[74]. Using a photolithography-based approach, we could successfully fabricate flat GelMA-PEGDA hydrogels with embedded NIH/3T3 fibroblasts in the bulk of the hydrogel and Caco-2 cells on top (Figure 1.14)). By comparing Caco-2 grown on cell-free *vs*. fibroblast-laden GelMA-PEGDA hydrogels, we could observe how the presence of fibroblasts

yielded better epithelial barriers (more native-like permeability and transepithelial electrical resistance).

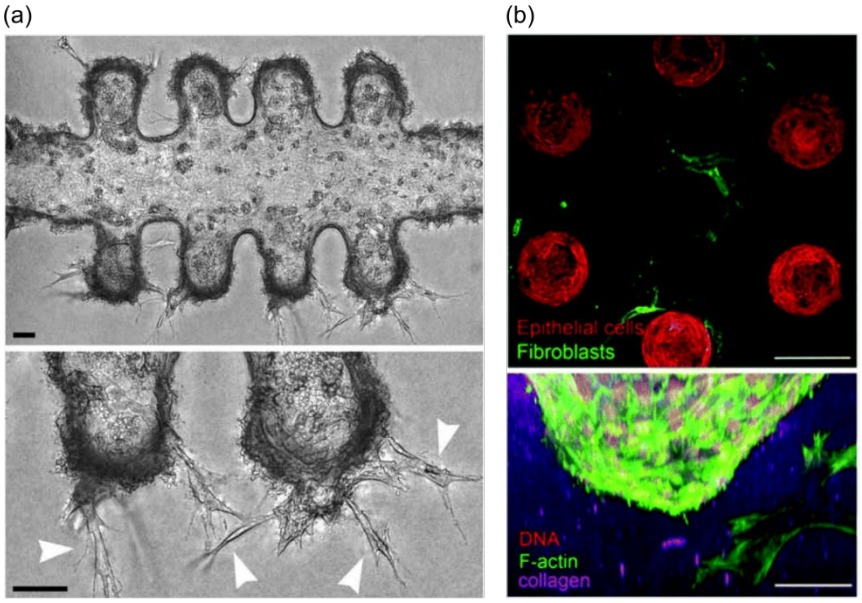

Figure 1.13. (a) Three days after the co-seeding of fibroblasts and intestinal stem cells, fibroblasts localize predominantly in crypt regions and extend pseudopodia into the surrounding matrix (arrows), recapitulating the *in vivo* tissue architecture. Scale bars: 50 μm. Adapted with permission from Nikolaev et al.[68]. (b) Top: a monolayer of epithelial cells (F-actin labelled, red) four days after seeding the organoids over the collagen scaffold containing fibroblasts (expressing αSMA, green). A cross-section through the crypt region, 348 μm from the top of the scaffold showing fibroblasts in contact with crypts. Scale bars: 150 μm. Bottom: side view of the crypt. Epithelial cells and mouse intestinal fibroblasts (F-actin, green; DNA, DAPI, red), collagen (TAMRA-labelled, pink). Scale bar: 50 μm. Adapted with permission from Verhulsel et al.[66]

Very recently, in the lab we have upgraded this model by including the 3D architecture through the in-house developed DLP bioprinting technology and fine tuning the hydrogel formulation, which now allowed the spreading of the fibroblasts within[75]. However, in both these *in vitro* models, a carcinoma cell line as epithelial source was employed. **One of the aims of this thesis is to engineer a more physiologically relevant *in vitro* model of the intestinal mucosa consisting in a villus-like GelMA-PEGDA hydrogel containing fibroblasts and organoid-derived cells as epithelial source.**

All in all, we have seen that, although huge advances have been made in *in vitro* intestinal models compared to the still standard Caco-2 model, there is no ultimate *in vitro* model yet. Indeed, we believe that for the moment, no new engineered platform will satisfy all the desired features, meaning direct access

to the apical side, tissue mechanical properties, retrieving of the native architecture, compatibility with establishing biochemical gradients, the use of physiologically relevant epithelial cell model and mimicking of the mesenchymal compartment. Instead, in our opinion, for each different application there will be a different optimal *in vitro* model, and consequently, a different fabrication technique, scaffold material and cell model. For instance, replica moulding is still the best technique to achieve high aspect ratio microstructures, but when high-through put and easy procedure is desired, photolithography, SLA or DLP are preferred. In terms of materials, synthetic ones such as PEG-based polymers are the best option when mechanical and chemical control are desired, for instance, to mimic biochemical gradients. In contrast, natural materials such as gelatine, collagen I, Matrigel or a mixture of the two are an excellent choice when the aim is to incorporate stromal cells.

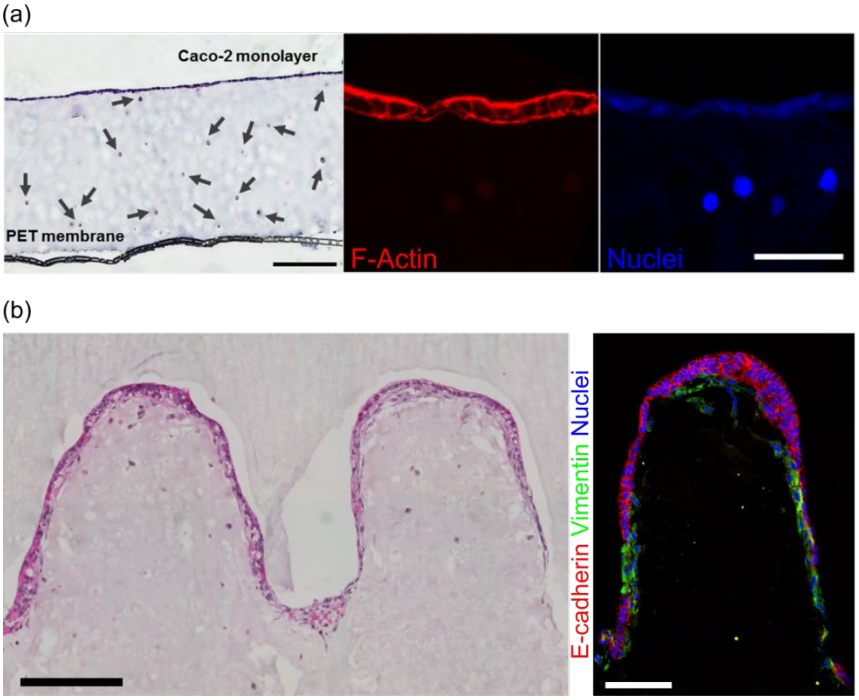

Figure 1.14. (a) Cross-section of haematoxylin and eosin (H&E) stained co-culture samples in hydrogel co-networks showing the formation of an intact epithelial monolayer at the top and a uniform distribution of the NIH-3T3 fibroblasts (arrows) throughout the hydrogel (left panel). Immunostainings of samples after 21 days of co-culture showing F-actin (middle panel) and Nuclei (right panel). Scale bar: 50 µm. Adapted with permission from Vila et al.[74] (b) H&E staining showing fibroblasts distribution at different regions of the samples and their co-localization with epithelial cells (left panel). Scale bar = 100 µm. E-cadherin (red) and vimentin (green) immunostaining show the distribution and localization of both cell types. Scale bar = 100 µm. All samples were fixed and stained after 21 days of culture. Adapted with permission from Torras et al.[71].

With the intention of having the best of both worlds, copolymers combining synthetic and natural material have emerged, yet there is still room for improvement. Finally, when the purpose is to answer a specific biological question, at times it is a clever strategy to reduce the complexity of the model to be able to obtain a clear readout, and then, if possible and desired, to increase back the complexity of the model and confirm the results obtained previously.

2. Objectives

Nowadays, the standard *in vitro* model of the small intestine still consists in a monolayer of cancer-derived cells seeded on a hard substrate. Recently, the long-term culture of primary intestinal epithelial cells has been achieved through intestinal organoids, self-organizing 3D structures retrieving many of the features of the native tissue such as cell compartmentalization. Yet, they still have some limitations: (i) they are closed structures whose apical side is difficult to access, (ii) to grow, they require to be embedded in a highly heterogeneous matrix, (iii) they do not retrieve the three dimensionality of the tissue and (iv) they do not include the mesenchymal compartment. Therefore, **the aim** of this thesis is to contribute to the development of complex *in vitro* models of intestinal epithelium focusing on the incorporation of the input of the stroma. Towards this general objective, the **specific objectives** are the following:

1. To adapt an in-house developed photolithography-based technique to obtain hydrogels with crypt-like microstructures.

2. To engineer a villus-like model of the intestinal epithelium using organoid-derived cells that allows the formation of gradients of factors of the intestinal stem cell niche secreted by epithelial cells and fibroblasts.

3. To study the role of intestinal fibroblasts in epithelial cell migration under homeostatic conditions by developing a simplified 2D coculture platform.

4. To develop a villus-like *in vitro* model that includes the stromal and the epithelial compartments to evaluate the role of fibroblasts in epithelial growth.

3. Materials and Methods

3.1. Cell culture

3.1.1. Cell lines

3.1.1.1. NIH/3T3 fibroblasts culture

NIH/3T3 mouse fibroblasts were employed to mimic the cellular components of the lamina propria in some of the experiments. They were selected because they are a simple cell model easy to grow, which was convenient for some optimization purposes.

NIH/3T3 fibroblasts (ATCC® CRL-1658™) were cultured using NIH cell culture medium (DMEM (1x) plus GlutaMAX™ (Gibco) medium supplemented with 10% Fetal Bovine Serum (FBS) (Life Technologies) and 1% Penicillin-Streptomycin (Sigma-Aldrich)) at 37°C in a humidified incubator under a 5% CO_2 atmosphere. The stock of NIH/3T3 cells was maintained by periodically passaging the cells every 3 days upon 80% confluency with a split ratio of 1:10. Typically, cells were first rinsed with warm Phosphate Buffered Saline solution (PBS) (Life Technologies), then they were incubated with Trypsin-EDTA (Life Technologies) for 5 minutes at 37°C. Next, Trypsin-EDTA was neutralized by adding an equal volume of culture medium and cells were centrifuged at 1200 rpm for 5 minutes. The supernatant was discarded, the pellet was resuspended in culture medium, and the proportional volume was seeded in a new flask containing warm culture medium.

3.1.1.2. LINTERNA NIH/3T3 fibroblasts culture

LINTERNA NIH/3T3 fibroblasts were employed to be able to visualize the cells using fluorescence during live imaging experiments. LINTERNA NIH/3T3 fibroblasts (Innoprot) were cultured with the same medium used for standard NIH/3T3 fibroblasts but supplemented with 10 ug mL^{-1} puromycin (Santa Cruz) to maintain the selection of cells expressing the turboGFP protein. The passage of LINTERNA NIH/3T3 cells was performed in the same way as for standard NIH/3T3 cells (see section above).

3.1.2. Primary intestinal cells

In general, primary cells, as opposed to cell lines, represent advanced culture models that better recapitulate the tissue physiology[76]. For the case of intestinal epithelial cells, it has been demonstrated that the standard model Caco-2, not only is derived from a carcinoma but also exhibits characteristics far from the

normal tissue such as a much tighter barrier[77]. In contrast, intestinal organoids, have been proven to share many of the traits of the native tissue such as their genetic signature, functionality and compartmentalization into proliferative and differentiated regions[78]. Therefore, we employed primary epithelial single cells derived from mouse intestinal organoids to mimic the epithelial compartment.

As for the stromal cells, it has been extensively shown that resident intestinal fibroblasts exert many functions such as the secretion of cytokines during inflammation, growth factors involved in the maintenance of the stem cell niche, extracellular matrix proteins (ECM) and degradation enzymes[25]. These are highly specific functions of intestinal fibroblasts and, for instance, have not been shown to occur in embryonic fibroblasts. Therefore, in some experiments we have employed primary mouse fibroblasts to represent the intestinal fibroblastic population.

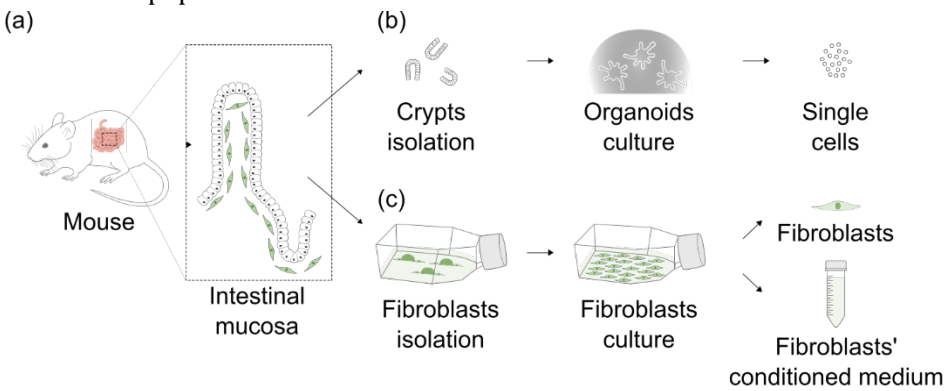

Figure 3.1. Schematic drawing showing the procedure to obtain all the primary cells used for this thesis. (a) Zoom-in in the mouse small intestine displaying the intestinal architecture composed of villus and crypt units with the monolayer of epithelial cells and the fibroblasts beneath. (b) Crypts are isolated from the small intestine; they are cultured embedded in Matrigel drops with the suitable medium until they evolve into organoids, and these are broken down to obtain single cells to use for the experiments. (c) After crypt isolation, the intestine is further digested, and the pieces of tissue obtained are seeded in cell culture flasks. Upon time, fibroblasts start coming out of the tissue pieces and populate the flask. Fibroblasts and their conditioned medium are used for the experiments.

Figure 3.1 shows a schematic of the process to obtain all the primary cells used for this thesis starting from the mouse small intestine.

All experimental protocols involving mice were approved by the Animal care and Use Committee of Barcelona Science Park (CEEA-PCB) and the Catalan government and performed according to their relevant guidelines and regulations. All mice were provided by the Laboratory of Professor Eduard Batlle from the Institute for Research in Biomedicine (IRB, Barcelona).

3.1.2.1. Intestinal crypt isolation and organoid culture

Organoid cultures were established from three types of genetic mouse models (Figure 3.2). *Lgr5-eGFP-IRES-creERT2*[79] (henceforth Lgr5-GFP) mouse model allowed the visualization of $Lgr5^+$ epithelial stem cells located in the crypts of the mouse intestines through the expression of green fluorescent protein (GFP) (Figure 3.2 (a)). *Lgr5-eGFP-IRES-creERT2;Rosa26-tdTomato* (henceforth tdTomato) mouse model, upon Cre-mediated recombination induced by tamoxifen, Lgr5-eGFP- expresses robust tdTomato fluorescence in Lgr5-expressing cells and their progeny (Figure 3.2 (b)). *ROSA26-creERT2;mT/mG*[80] (henceforth mTmG) mouse model consists of a cell membrane-targeted, two-colour fluorescent Cre-reporter allele. Prior to Cre recombination, cell membrane-localized tdTomato (mT) is expressed in all tissues (Figure 3.2 (c)). Upon the activation of Cre recombinase through tamoxifen, all cells (and future cell lineages derived from these cells) express cell membrane-localized GFP (mG) instead of mT.

Intestinal crypts were isolated as previously described[81,82]. Briefly, the small intestine was washed with PBS and fat and faeces were removed. Then, the tissue was cut longitudinally, and the villi were removed by scrapping with a coverslip. The tissue was cut in small pieces and washed gently with PBS. Then, the pieces were incubated with PBS containing 2 mM EDTA (Sigma-Aldrich) for 40 minutes at 4°C in a rocking platform. The tissue was then harshly washed with PBS containing 10% FBS and the supernatant was filtered through a 70 μm pore cell strainer (Biologix Research Co.). The washing and filtering steps were repeated 7 times obtaining 7 crypt fractions. After centrifugating for 5 min at 800 rpm, crypts were resuspended with drops of the commercial protein mixture Matrigel® (BD Bioscience). The drops were let to gel at 37º C for 5 min and were cultured with advanced DMEM/F12 (Invitrogen) medium complemented with 1% Glutamax (Gibco), 1% HEPES (Sigma-Aldrich), 0.2% Normocin (Invitrogen), 2% B27 (Gibco), 1% N2 (Gibco), and 0.25% N-acetylcysteine (Sigma-Aldrich), obtaining the so-called basal medium. The basal medium was supplemented with recombinant murine epidermal growth factor, EGF (100 ng mL^{-1}, Gibco), recombinant murine Noggin (100 ng mL^{-1}, Peprotech), recombinant human R-spondin 1 (200 ng mL^{-1}, R&D Biosystems), CHIR99021 (3 μM, Tebubio) and Valproic Acid (1 mM, Merck Life Science) to obtain what we called ENRCV medium. For the first 4 days of culture, Rho kinase (ROCK) inhibitor Y-27632 (10 μM, Sigma-Aldrich) was added to the medium to prevent anoikis[83], a cell death mechanism that is triggered on anchorage-dependent cells when they are deprived from other cells or the ECM. Within 3-4 days of culture, the crypts developed into 3D closed structures called organoids. These consist of a central lumen lined by an epithelium with crypt-

and villus-like domains, with crypts budding from spherical structures (Figure 3.1 (b), Figure 3.2).

For the maintenance of the organoid culture, outgrowing crypts were passaged twice a week. Briefly, Matrigel drops containing organoids were collected using the used culture medium and transferred to a falcon tube. Then, they were mechanically disrupted by passing them 3 times through a 23 G 1" needle (BD Microlance 3) coupled to a 1 mL syringe. Next, they were washed by adding PBS and vigorously shaking. The resulting solution was centrifuged at 700 rpm for 3 min. Crypt pieces were then plated again in Matrigel drops. Organoid stocks were maintained for up to 4 months at 37°C in a humidified incubator under a 5% CO_2 atmosphere.

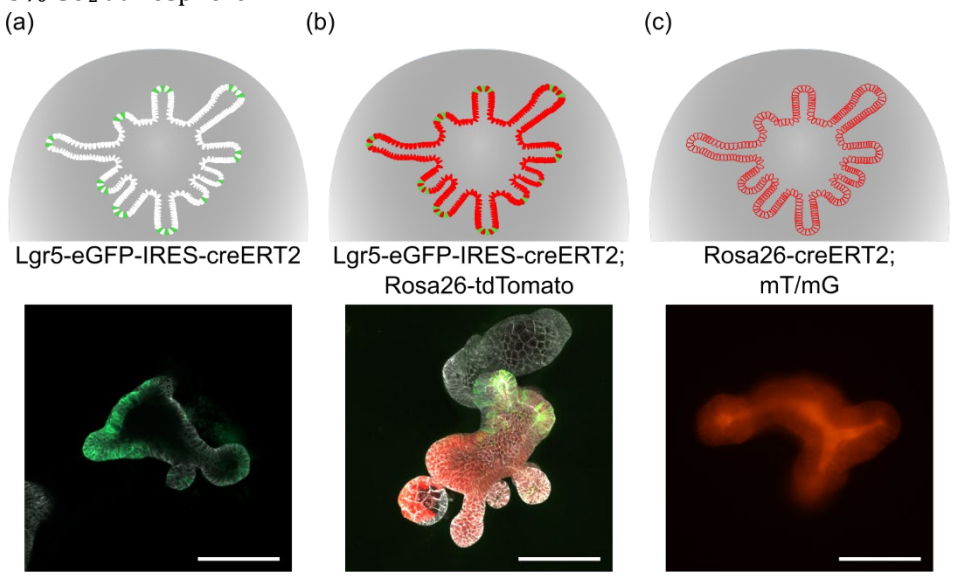

Figure 3.2. Schemes (top panels) and fluorescence microscopy images (bottom panels) of the intestinal organoids derived from the different mouse models: (a) Lgr5-eGFP-IRES-creERT2, (b) Lgr5-eGFP-IRES-creERT2; Rosa26-tdTomato and (c) Rosa26-creERT2;mT/mG. Scale bars: 100 µm.

3.1.2.2. Organoid digestion into single cells and their culture

To obtain organoid-derived single cells, fully grown organoids were now subjected to a harsh digestion protocol[60]. In short, Matrigel drops containing organoids were enzymatically disrupted by pipetting them with TrypLE Express1X (Gibco). The TrypLE Express1X activity was previously reduced by heating it at 37°C for 1 hour in a water bath. The solution containing the disrupted organoids was transferred to a Falcon tube at 4°C, followed by mechanical disruption using a syringe with a 23 G 1" needle (BD Microlance 3). Single cells or small cell clusters were obtained by incubating such solution for

approximately 3 min at 37°C under agitation every minute. After confirming the organoids dissociation into single cells, the TrypLE Express1X was neutralized by adding PBS with 2% FBS, and the solution was centrifuged at 1000 rpm for 5 minutes. Organoid-derived single cells were seeded and cultured using ENRCV medium and ROCK inhibitor Y-27632, unless stated otherwise.

3.1.2.3. Isolation and culture of intestinal primary fibroblasts

Intestinal primary fibroblasts were isolated from the same three models used to establish organoids' culture. Lgr5-GFP- and tdTomato-derived stromal cells exhibited a wild-type phenotype (no fluorescence). mTmG-derived stromal cells exhibited cell membrane-localized tdTomato fluorescence (mT). Intestinal primary fibroblasts were isolated from mouse small intestine by adapting a previously published protocol[84]. Briefly, once the crypts were isolated (Section: Intestinal crypt isolation and organoid culture), the tissue pieces were further digested by first performing 3 incubations of 10 min with 3 mM EDTA in PBS containing at 37ºC shaking. Next, after a washing with PBS, the pieces were incubated with collagenase (100 U mL^{-1}) (Sigma-Aldrich) in culture medium for 30 minutes at 37ºC shaking. Then, the tissue was centrifuged at 1200 rpm for 5 min and the pellet was resuspended in DMEM (1X) with GlutaMAX™ (Gibco) medium supplemented with 10% FBS, 1% Penicillin-Streptomycin (Sigma-Aldrich) and 1% v/v minimum essential medium non-essential amino acids (MEM-NEAA; Gibco) (primary fibroblasts culture medium). The tissue pieces were cultured in flasks kept at 37°C in a humidified incubator under a 5% CO_2 atmosphere. After seven days in culture, tissue pieces had attached, and fibroblasts started to come out and attach to the flasks (Figure 3.3. (a)). Plates reached confluency after approximately fourteen days (Figure 3.3. (b)). Primary fibroblasts were passaged with a split ratio of 1:2 or 1:3, by first rinsing the cells with warm PBS and incubating them with Trypsin-EDTA (Life Technologies) for 5 minutes at 37°C. Next, Trypsin-EDTA was neutralized by adding an equal volume of culture medium and cells were centrifuged at 1200 rpm for 5 min. The supernatant was discarded, the pellet was resuspended in culture medium, and the proportional volume was seeded in a new flask containing warm culture medium. Primary fibroblasts were only passaged a maximum of 5 times. mTmG-derived fibroblasts were treated with 4-hydroxytamoxifen (Merck Life Science) for seven days to convert them from mT^+ to mG^+ fibroblasts. mG^+ fibroblasts were cocultured with tdTomato organoid-derived cells in live imaging experiments in the context of epithelial cell migration studies (section 3.3.5).

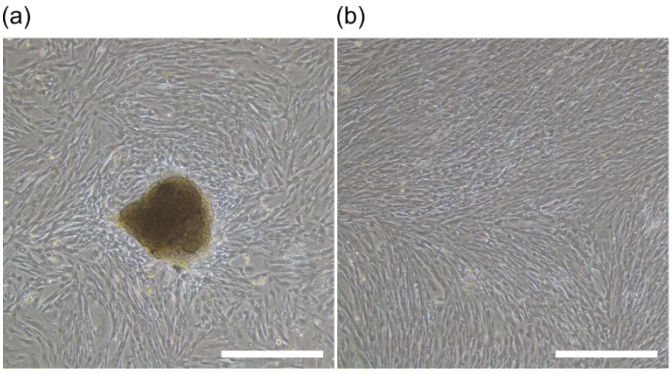

Figure 3.3. Bright field images of primary fibroblasts cultures. (a) Seven days in culture where tissue pieces together with fibroblasts can be seen. (b) 14 days in culture where no tissue pieces are remaining, and fibroblasts have reached confluency. Scale bars: 500 μm.

3.1.2.4. Preparation of primary fibroblasts conditioned medium

The culture medium used to grow the primary fibroblasts for 4-6 days was collected, centrifuged, and filtered through a 0.22 mm pore size filter (Merck-Millipore) in order to get rid of the debris. Next, it was supplemented with 2% B27, 1% N2 and 0.25% N-acetylcysteine, obtaining primary fibroblast_CM. To render it suitable for the culture of organoids or organoid-derived cells, the primary fibroblast_CM was supplemented with EGF (100 ng mL^{-1}), human R-Spondin 1 (200 ng mL^{-1}), Noggin (100 ng mL^{-1}), CHIR99021 (3 mM), valproic acid (1 mM), resulting in primary fibroblast_CM/ENRCV.

3.2. Materials and Methods for sections 1 and 2

3.2.1. Fabrication

3D microstructured PEGDA-AA hydrogels were fabricated by means of free radical photopolymerization of poly(ethylene glycol) diacrylate (PEGDA) triggered by UV light. Both the composition of the hydrogel precursor solution and the method to obtain 3D villus-like hydrogels were previously developed in our lab[69]. In detail, the hydrogel prepolymer solution was prepared by dissolving 6.5% w/v 6000 Da molecular weight PEGDA (P6000) (Sigma-Aldrich), 1% w/v of the photoinitiator, 2-hydroxy-1-[4-(2-hydroxyethoxy) phenyl]-2-methyl-1-propanone (I2959) (Sigma-Aldrich) and 0.3% w/v of acrylic acid (AA) (Sigma-Aldrich) in PBS. To fabricate crypt-like hydrogels with fluorescent beads, we prepared a 1:1000 dilution of FluoSpheres™ Carboxylate-Modified Microspheres (polystyrene-based beads emitting fluorescence at 680 nm) (Thermo Fisher Scientific) in the prepolymer solution. The solution was protected from light at all times and filtered through a 0.22 mm filter (Merck-Millipore) prior use. A PDMS stencil with a central pool of 6.5 mm in diameter,

two inlets of 1.5 mm and 1 mm in high was placed on a plastic surface covered with an opaque adhesive tape to prevent the reflected light from interfering with the reaction. Next, a silanized 12 mm in diameter Tracketch polyethylene terephthalate (PET) membrane of 5 μm pore size (Sabeu GmbH & Co.) was placed on top of the central pool. Then, the hydrogel precursor solution was flown through one inlet into the chip. For the crosslinking of the hydrogel, a mask aligner instrument (SUSS MicroTec MJB4) equipped with a mercury short arc lamp (OSR HBO 350 W/S) was used. The UV intensity used was 25 mW cm^{-2}. In order to obtain 3D microstructures, photomasks were used during the photopolymerization of the hydrogels. The photomasks designs to obtain crypt-like hydrogels consisted in circular black regions with a diameter of 50, 75 or 100 μm and a pitch of 250 μm which had a density of 16 black windows mm^{-2}, respectively. The photomask design to obtain villus-like hydrogels consisted in circular transparent regions with a diameter of 100 μm and a pitch of 150 μm, which had a density of 16 transparent windows mm^{-2}. The crypt-like structures of 50 and 75 μm in diameter were fabricated using a single step of UV exposure of 50 and 70 s, respectively.

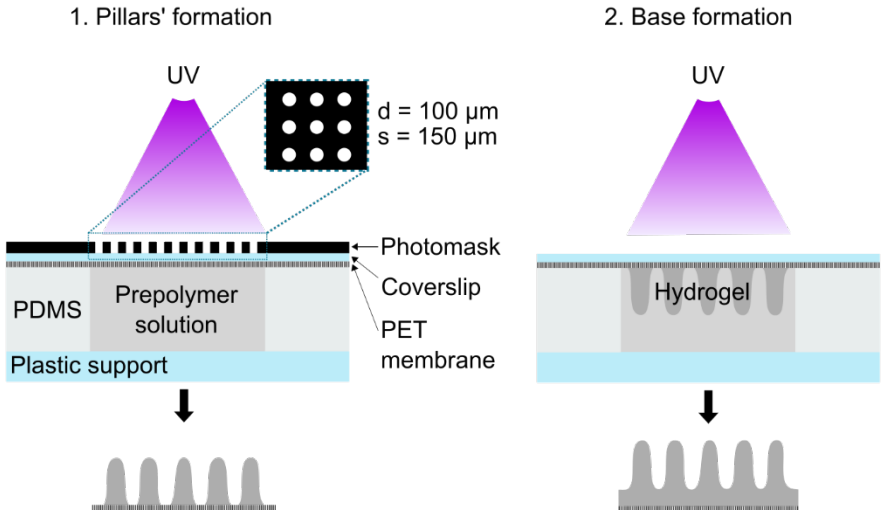

Figure 3.4. Schematic drawing of the fabrication procedure of villus-like microstructured PEGDA-AA hydrogel scaffolds on porous PET membranes. 1. During the first exposure, the microstructures were formed using a photomask consisting of an array of circular transparent windows with a diameter (d) and a spacing (s) of 100 μm and 150 μm, respectively. 2. In the second exposure, the photomask was removed and the base with a 6.5 mm diameter (PDMS pool dimension) was formed. This step was needed to create a homogeneous hydrogel surface.

The crypt-like structures of 100 μm in diameter were formed by a two-step UV exposure: first, the hydrogel prepolymer solution was exposed for 10 s without the photomask to form a base; second, the photomask was placed and the hydrogel prepolymer solution was exposed for 50 s. To fabricate the villus-like

structures we also employed a two-step UV exposure. In this case, the hydrogel prepolymer solution was exposed for 218 s (energy dose of 5.4 J cm^{-2}) through the photomask to form the pillars (Figure 3.4 (1)), the hydrogel was then removed from the PDMS stencil and it was washed first with PBS and next with the hydrogel prepolymer solution. Then, the hydrogel was placed back to the chip and more precursor solution was flown before a second UV exposure of 25 s (energy dose of 0.6 J cm^{-2}) without the photomask, forming the base (Figure 3.4 (2)).

3.2.2. Characterization

After fabrication, the hydrogel scaffolds were kept in PBS for 3 days until equilibrium swelling [69,85] and visualized by a bright field microscope (Nikon Eclipse Ts2). In the case of villus-like hydrogels, the pillars were cut out of the scaffolds with the help of a surgical blade (Didactic) or a 27 G 3/4 " needle (BD Microlance 3) and tilted horizontally to be able to visualize the cross-sections. The samples were kept submerged in PBS at all times. The images were analysed with FiJi (http://rsb.info.nih.gov/ij, NIH, USA) and the height, base diameter and tip diameter were measured for at least 3 pillars (Figure 3.5 (left)). In the case of the crypt-like hydrogels, the samples were directly visualized through a confocal microscope (LSM 800, Zeiss) using the autofluorescence of PEGDA. The images were analysed with ImageJ and crypt depth, top diameter and bottom diameter were measured (Figure 3.5 (right)).

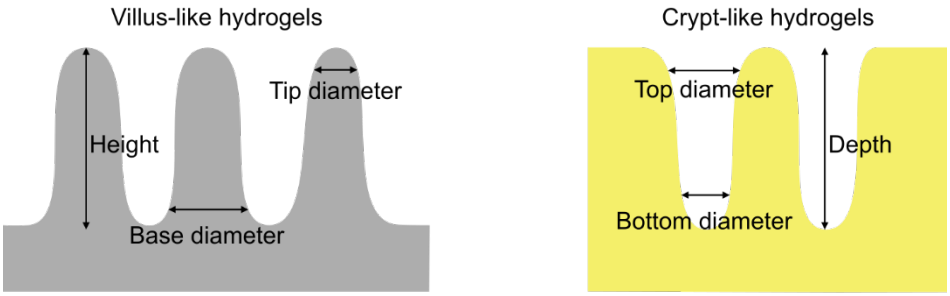

Figure 3.5. Schematic representation of dimensions measured on microstructured PEGDA-based hydrogels.

3.2.3. Mounting onto Transwell® inserts

For the cell culture experiments, the fabricated hydrogels were manually mounted onto Transwell® inserts (Merck Life Science) adaptable to 24 wells-plates (Merck Life Science) (Figure 3.6) to enable the use of different solutions at the apical and basolateral compartments and thus, establish gradients by diffusion. In detail, the original membrane was first removed. Next, a ring of

pressure-sensitive adhesive (PSA) (Adhesive Research) of 6.5 mm inner diameter and 13 mm outer diameter was attached to the Transwell inserts, then the scaffold was placed and finally a second PSA ring was added.

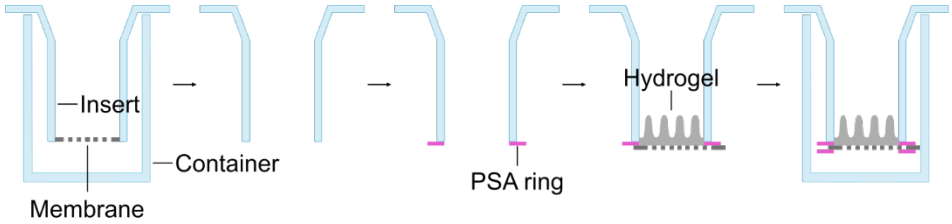

Figure 3.6. Schematic illustration of the process to mount hydrogels on standard Transwell® inserts.

3.2.4. Protein functionalization

To functionalize the PEGDA-AA hydrogels with ECM proteins, we used the N-(3-Dimethylaminopropyl)-N' -ethylcarbodiimide (EDC) (Sigma-Aldrich)/ N-Hydroxysuccinimide (NHS) (Sigma-Aldrich) mediated coupling, as previously described[69] (Figure 3.7).

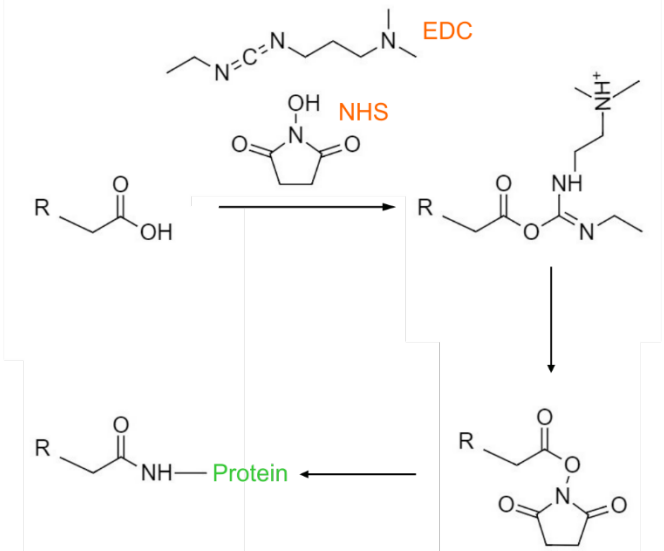

Figure 3.7. Functionalization strategy based on EDC/NHS used to couple proteins to PEGDA-AA hydrogels. Carboxyl groups of hydrogels were first activated with EDC. Then, EDC is displaced by NHS to form a semi-stable NHS-ester. Next, the NHS is replaced by the primary amine of the protein, forming a covalent bond between the protein and the hydrogel.

Specifically, the carboxylic groups of PEGDA-AA hydrogels were activated with a solution containing 25 mM EDC and 50 mM NHS in MES buffer (0.1 M, pH 4.7) for 30 min, shaking at room temperature. Hydrogels were then washed with PBS and incubated with the corresponding protein diluted in PBS overnight at 4°C.

The following proteins or mixtures of proteins and their respective concentrations were used: collagen I (Sigma-Aldrich, 400 µg mL^{-1}), fibronectin (Merk Life Science, 100 µg mL^{-1}), laminin (Merk Life Science, 250 µg mL^{-1}) and Matrigel (Corning, 500 µg mL^{-1}). After incubation, hydrogels were washed again with PBS and the protein functionalization was characterized by immunostaining the samples anti-the corresponding protein (in the case of samples functionalized with Matrigel, we used the antibody against laminin) and imaging them through confocal microscopy (LSM 800, Zeiss).

3.2.5. Formation of Biomolecular Gradients along the vertical axis of the villus-like PEGDA-AA hydrogels

Gradients of the biomolecules reported to be relevant for the formation and maintenance of the intestinal stem cell (ISC) niche at the intestinal crypts, listed in Table 3.1, were established. In detail, ISC niche relevant biomolecules were delivered at the basolateral compartment of the Transwell insert so that they would diffuse along the vertical axis of the villus-like PEGDA-AA hydrogels, thus creating a concentration gradient along this direction. To account for the cellular effects of the biomolecular gradients formed, four different culture conditions were established: (i) *asymmetric*, where primary fibroblast_CM/ENRCV medium was delivered basolaterally and basal medium was delivered apically; (ii) *uniform*, with the basolateral and apical delivery of primary fibroblast_CM/ENRCV medium; (iii) *asymmetric 2.0*, where the concentrations of Noggin and R-spondin were doubled compared to asymmetric while keeping basal medium at the apical chamber, and (iv) *asymmetric Wnt2b*, where the primary fibroblast_CM was replaced by the recombinant protein Wnt2b (Bio-Techne R&D Systems), so ENRCV medium plus Wnt2b were delivered in the basolateral chamber and basal medium at the apical side. Final delivered concentrations for the different relevant biomolecules were determined from the simulations and are detailed at Table 3.1. Previous experiments of BSA diffusion[85] showed that 66% of protein concentration was getting trapped at the Transwell membrane. To compensate for this effect, protein source concentrations were tripled compared to concentrations used for organoids culture within Matrigel drops. Given that the *in silico* simulations[85,86] predicted that the gradients would be stable as long as there was period replenishment every 24h, in the cell culture experiments we added the different media in the corresponding Transwell compartment 24 hours before cell seeding so that when cells were seeded, gradients would be stable, and then, upon cell seeding, the medium of both compartments was also renewed every 24 h to maintain the gradients formed.

Condition	Compartment	Factor / Medium	EGF (ng mL^{-1})	Noggin (ng mL^{-1})	R-spondin (ng mL^{-1})	CHIR (μM)	Valproic Acid (mM)	Wnt2b (ng mL^{-1})
Asymmetric	Apical	Basal medium	0	0	0	0	0	0
	Basolateral	Primary fibroblasts_ CM + 3 x (ENRCV)	300	300	600	9	3	0
Uniform	Apical	Primary fibroblasts_ CM + ENRCV	100	100	200	3	1	0
	Basolateral	Primary fibroblasts_ CM + 3 x (ENRCV)	300	300	600	9	3	0
Asymmetric 2.0	Apical	Basal medium	0	0	0	0	0	0
	Basolateral	Primary fibroblasts_ CM + 3 x (EN_2R_2CV)	300	600	1200	9	3	0
Asymmetric Wnt2b	Apical	Basal medium	0	0	0	0	0	0
	Basolateral	Basal medium + Wnt2b + EN_2R_2CV	300	600	1200	9	3	600

Table 3.1. Detailed medium composition and used concentration of each factor of the apical and basolateral compartments of each gradient condition.

3.2.6. Culture of organoid-derived cells on PEGDA-AA hydrogels with biomolecular gradients

Organoids' digestion into single cells was performed as previously described. In the case of villus-like PEGDA-AA hydrogels, 5×10^5 intestinal epithelial cells were resuspended in 100 μL of the corresponding fresh apical medium and seeded on the hydrogels. Once the cells were adhered (after 1 h), 100 μL of the corresponding fresh apical medium was added. At the moment of cell seeding, the medium of the basolateral compartment was also renewed to maintain the established gradients. In the case of crypt-like PEGDA-AA hydrogels, 3×10^5 intestinal epithelial cells were resuspended in 200 μL of ENRCV medium and

seeded on the hydrogels. Samples were maintained in an incubator at 37 °C and 5% CO_2 and media was renewed every 24 h.

3.2.7. Immunostaining and image acquisition

To characterize the functionalization of crypt-like hydrogels, samples were first blocked with 1% BSA (Sigma-Aldrich), and 3% donkey serum (Millipore) in PBS for 30 min shaking at room temperature (RT). Next, samples were incubated with primary antibodies (Table 3.5.1) against collagen I, fibronectin or laminin diluted in primary antibody buffer (0.1% BSA and 0.3% donkey serum) for 1h shaking at RT. After several PBS washings, samples were incubated for 45 min at RT with the corresponding secondary antibodies (Table 3.5.2). Samples were finally washed and mounted using PBS.

Cells were fixed with 10% neutralized formalin (Sigma-Aldrich) at corresponding timepoints after seeding. Next, samples were carefully demounted from Transwell inserts and placed in new well plates. Then, they were permeabilized with 0.5% Triton X-100 (Sigma-Aldrich) and blocked with 1% BSA, 3% donkey serum, and 0.2% Triton X-100 in PBS for 2 h at RT. Samples were incubated with primary antibodies (Table 3.5.1) against Ki67, GFP, Lysozyme (Lyz), cytokeratin 20 (CK20) and fatty acid binding protein 1 (FABP1) overnight at 4°C followed by several PBS washings.

Next, it followed a 1 h incubation at RT with the adequate secondary antibodies (Table 3.5.2) plus DAPI and rhodamine-phalloidin. Right before imaging, samples were then mounted in PBS on coverslips using 0.8 mm PDMS spacers to avoid the smashing of the villus-like microstructures.

Fluorescence images were acquired using a confocal laser scanning microscope (LSM 800, Zeiss) with a 10x objective (NA = 0.3, WD = 2.0). The laser excitation and emission light spectral collection were optimized for each fluorophore. The pinhole diameter was set to 1 Airy Unit (AU). A z-step of 5 µm was used.

3.2.8. Analysis

3.2.8.1. Surface coverage

The relative surface covered by the epithelial cells was quantified in FiJi by measuring the area occupied by cells and normalizing to the surface of the substrate. To account for tridimensionality of the available surface provided by the villi, the area of a pillar was approximated to the area of a truncated cone (ATC), a method previously used in the lab[85].

The total area (TA) of the sample can then be calculated as follows:

$$TA = 2D_{projected\ area} - Pillars\ base_{area} + Pillars_{area}$$

Where $2D_{\text{projected area}}$ is the total surface of the sample projected in a plane, Pillars $\text{base}_{\text{area}}$ is the surface occupied by all the base of all the pillars, and $\text{Pillars}_{\text{area}}$ is the total area of the pillars minus its base.

To calculate the number of pillars of the sample, first the total number of pillars in a given area was estimated. For that, the area occupied by 4 pillars was calculated by selecting a square ROI. Then, this number was proportioned to the 2D projected area of the villus-like hydrogel to obtain the total number of pillars (p).

$$TA = 2D_{projected\ area} - p * (\pi R^2) + p * ATC$$

To calculate the covered area (CA), we used the following equation:

$$CA = 2D_{projected\ covered\ area} - Pillars\ base_{\ covered\ area} + Pillars_{covered\ area}$$

$$CA = 2D_{projected\ covered\ area} - p_{covered} * (\pi R^2) + p_{covered} * ATC$$

To quantify the $2D_{projected\ covered\ area}$, we performed the maximum intensity projection of the F-actin fluorescence images, and we applied an over/under threshold, obtaining the area with F-actin signal. Then, we manually counted the covered pillars and we computed the Pillars $\text{base}_{\text{covered area}}$ and the $\text{Pillars}_{\text{covered area}}$. Finally, we simply calculated the surface coverage (%) following this equation:

$$Surface\ Coverage = \frac{CA}{TA}\ x\ 100$$

To quantify the surface coverage, we analysed for *Asymmetric* day 1: n = 3 samples from N = 3 independent experiments, day 2: n = 2 from N = 2, and day 3: , n = 4 from N = 4; *Uniform* day 1: n = 3 from N = 3, day 2: n = 2 from N = 2 and day 3: n = 3 from N = 3.

3.2.8.2. Frequency and distribution of cell types

Confocal fluorescence microscopy images of Ki67, GFP, Lyz, CK20, and FABP1 markers were used to quantify the proliferative cells, stem cells, Paneth cells, differentiated cells and enterocytes, respectively, along the vertical axis of the villi. For this, a custom-made ImageJ macro was used to divide the confocal stacks to tiles, each comprising one single villus. For Ki67 and FABP1 markers, the following procedure was used. Each covered pillar was analysed using Imaris (Andor Technology, version 9.1.0). As a pre-processing step, a mean filter of 3×3×3 px to the Ki67 channel was applied to reduce the noise. Then, nuclei were detected with the Imaris Spot detector (diameter set to 9 μm) by manually adjusting the threshold. Next, positive cells for the marker in question (Ki67 or FABP1) were classified by applying a threshold of the mean intensity of the

marker. Finally, the positions in the villus axis (z) of all nuclei and of positive cells were exported as Microsoft Excel files. For each pillar, the z values were rescaled from 0 to 1, 0 corresponding to the nucleus detected closer to the villus base and 1 to the nucleus closer to the villus tips. Z distance was divided into five equal segments for data interpretation purposes. Next, the percentage of positive cells with respect to the total number of cells for the five regular Z segments along each villus was estimated. Finally, the fractioned percentage of each segment was computed. To quantify the frequency of $Ki67^+$ cells we analysed for *Uniform* condition: n = 19 pillars from N = 2 independent experiments; *Asymmetric*: n = 41 from N = 4. To quantify the frequency of $FABP1^+$ cells we analysed for *Uniform* condition: n = 13 pillars from N = 1 independent experiments; *Asymmetric*: n = 11 from N = 1.

To quantify the intensity signal along the vertical axis of each villus of CK20, GFP and Lyz, we used another custom-made ImageJ macro. Briefly, after dividing each stack into individual stacks comprising one pillar, we run the ImageJ built-in plot profile function within a drawn ROI surrounding the villus to quantify the mean intensity for the marker in question (CK20, GFP or Lyz) and F-actin fluorescent channels and we exported the data. We normalized the intensity values of the marker of interest by the F-actin ones to eliminate the intensity variations due to the image acquisition set up and we rescaled them from 0 to 1. Then, we rescaled the villus vertical axis from 0 to 1 and divided it into five equal segments for data interpretation purposes. Finally, we computed the mean intensity fraction of each segment.

To quantify the normalised mean GFP signal and the GFP^+ cells within the $Ki67^+$ population we analysed for *Uniform* condition: n = 12 pillars from N = 1 independent experiment; *Asymmetric*: n = 10 from N = 1. To quantify the normalised mean Lyz signal we analysed for *Uniform* condition: n = 12 pillars from N = 1 independent experiment; *Asymmetric*: n = 12 from N = 1. To quantify the normalised mean CK20 signal we analysed for *Uniform* condition: n = 12 pillars from N = 2 independent experiment; *Asymmetric*: n = 41 from N = 2.

3.3. Materials and Methods for section 3

3.3.1. Single cell RNA sequencing of primary fibroblasts

To characterize the different cell populations within the isolated stromal cells (section 3.1.2.3, we performed single cell RNA sequencing (scRNAseq) in collaboration with Dr. Anna Esteve Codina from the Centre Nacional d'Anàlisi Genòmica - Centre de Regulació Genòmica (CNAG-CRG). A pool of 3 vials of primary fibroblasts from 3 different isolations at passage 2-4 was prepared to

remove the possible variability coming from the mouse selected. Briefly, the 3 vials were centrifuged at 335 rcf during 5 min at 4ºC and resuspended in DMEM/F12 with 10% FBS so as to have a cell density of 300-1000 cells μl^{-1}. Cell concentration and viability were determined using a TC20™ Automated Cell Counter (Bio-Rad Laboratories, S.A) upon staining the cells with Trypan blue. Cells were partitioned into Gel Bead-In-Emulsions (GEMs) by using the Chromium Controller system (10X Genomics), with a target recovery of 5000 total cells. cDNA sequencing libraries were prepared using the Next GEM Single Cell 3' Reagent Kits v3.1 (10X Genomics, PN-1000268), following manufacturer's instructions. Shortly, after GEM-RT clean up, cDNA was amplified during 12 cycles and cDNA quality control and quantification were performed on an Agilent Bioanalyzer High Sensitivity chip (Agilent Technologies). cDNA libraries were indexed by PCR using the PN-220103 Chromiumi7 Sample Index Plate. Size distribution and concentration of 3' cDNA libraries were verified on an Agilent Bioanalyzer High Sensitivity chip (Agilent Technologies). Finally, sequencing of cDNA libraries was carried out on an Illumina NovaSeq 6000 using the following sequencing conditions: 28 bp (Read 1) + 8 bp (i7 index) + 0 bp (i5 index) + 89 bp (Read 2), to obtain approximately 20-30.000 reads per cell.

To analyse the scRNAseq we collaborated with Dr. Anna Esteve (CNAG-CRG). Sequencing reads were processed using CellRanger v.6.1.2[87]. The output folder was used as input to perform downstream analysis with the R package Seurat 4.0.6 (R.4.1.2). Seurat object was created with the function CreateSeuratObject with the parameter min.cells = 3. To ensure cells of good quality, only cell barcodes within the range of 2000 - 7000 detected genes and < 5 % mitochondrial content were kept for the analysis. Data was normalized with the SCTransform method with default parameters. UMAP was performed with the 30 first principal components, followed by the functions FindNeighbours and FindClusters with default resolution. Cluster markers were identified with the function FindAllMarkers with the options only.pos = TRUE and logfc.threshold = 0.25 . Cell type annotation was performed manually looking the expression of the following cell type markers:

```
telocytes=c("Wnt4","Wnt5a","Wnt5b","Dkk3","Wif1","Chrd","Bmp1","Bmp2","
Bmp4","Bmp5","Bmp7","Acta2","Vim","Pdgfra","Foxl1","Myh11","Gli1","Cspg4"
,"Pdpn")
```

```
trophocytes=c("Wnt2b","Rspo1","Rspo2","Rspo3","Dkk2","Dkk3","Srfp1","Gre
m1","Bmp4","Vim","Pdgfra","Cd34","Gli1","Cd81")
```

PDGFRlow_stroma=c("Wnt2b","Wnt4","Rspo3","Dkk2","Dkk3","Srfp1","Frzb","Grem1","Bmp1","Bmp2","Bmp4","Bmp5","Bmp6","Vim","Pdgfra","Cd34","Gli1","Cspg4","Pdpn")

pericytes=c("Grem2","Acta2","Vim","Des","Myh11","Cspg4","Actg2","Pdgfrb","Rgs5")

neurons=c("Wnt6","Gfap","S100b")

immune cells =c("Bmp1","Cd52")

lymphatic cells=c("Lyve1")

blood cells =c("Pecam1")

3.3.2. Co-culture of intestinal organoids with primary fibroblasts

To test the effect of culturing primary fibroblasts with intestinal organoids, crypts derived from *Lgr5-EGFP-IRES-creERT2* intestinal organoids were embedded in Matrigel drops (section 3.1.2.1) together with primary fibroblasts and cultured with ENRCV medium (we called this culture *"+ fibroblasts*" condition). To test only the paracrine effect of primary fibroblasts, crypts were cultured alone with primary fibroblast_CM/ENRCV medium ("*+ fibroblasts conditioned medium*" or abbreviated "*+ fibr. cond. med.*" condition). Crypts were also cultured alone using ENRCV medium ("control" condition). Cultures were maintained for 2 days.

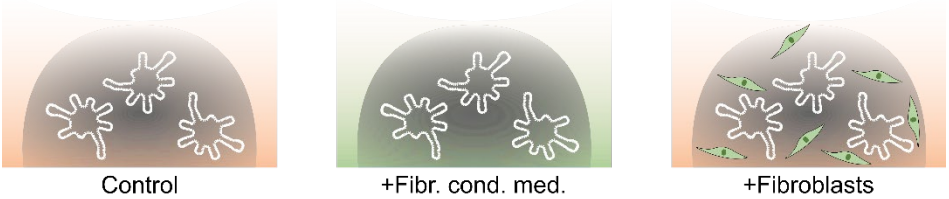

Figure 3.8. Scheme depicting the three culture conditions to test the effect of fibroblasts on the growth of intestinal crypts.

3.3.3. Setup of the gap closure models

Ibidi µ-Slides 8 wells (Ibidi GmbH) were coated with Matrigel to form thin films (< 2 µm) as an extracellular matrix (ECM) surrogate as previously described[60,88,89]. Briefly, Ibidi wells were coated with 10 µL cm^{-2} of 3 mg mL^{-1} Matrigel diluted in DMEM/F-12 (Invitrogen). To spatially confine cell growth and create a gap where cells could migrate to, we employed PDMS barriers fabricated in-house (section 3.3.2). The following experimental conditions were analysed: "*control*" (only organoid-derived cells), "*+ fibr. cond. med.*" (organoid-derived cells were cultured with primary fibroblasts_CM) and "*+ fibroblasts*"

(organoid-derived cells were cultured on top of a continuous monolayer of primary fibroblasts) (Figure 3.9). For the "*control*" condition (Figure 3.9 (left)), first the elastomeric barrier was placed and stuck (using PDMS grease, Corning) on the Matrigel coated wells. Then, $3.5x10^5$ organoid-derived cells cm^{-2} were seeded with ENRCV medium containing Y-27632 and cells were cultured for 1 day. For the "*+ fibr. cond. med.*" condition (Figure 3.9 (middle)), the elastomeric barrier was placed as in the *control* condition, then organoid-derived cells were seeded with primary fibroblast_CM/ENRCV medium containing Y-27632, and cells were cultured for 1 day. Finally, for the "*+ fibroblasts*" condition (Figure 3.9 (right), first, $3x10^4$ primary fibroblasts cm^{-2} were seeded on the Matrigel coated well and cultured with primary fibroblasts culture medium for 1 day, then the elastomeric barrier was placed, and $3.5x10^5$ organoid-derived cells cm^{-2} were seeded on top with ENRCV-medium containing Y-27632 for 1 day more. After the indicated times, the migration assay was initiated by carefully removing the elastomeric barrier, washing with warm PBS and adding new corresponding medium without Y-27632.

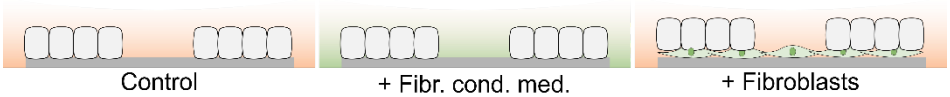

Figure 3.9. Scheme depicting the four gap closure conditions to test the effect of fibroblasts on the migration of intestinal epithelial cells.

3.3.4. Fabrication of PDMS barriers

First, a mould with 9.5 x 10.5 mm wells with a central barrier of 1.5 mm was 3D printed using the resin FREEPRINT® Ortho 385 (Detax) with the Versus 385 nm printer (Microlay) and cured under a UV lamp for 1 h. Next, before casting the intermediate mould, the first mould was silanized to ease the unmoulding. For that, the mould was placed in a desiccator with drops of Trichloro(1H,1H,2H,2H-perfluorooctyl)silane (Sigma-Aldrich) and kept under vacuum for 1 h. Then, an intermediate mould was fabricated using the silicone Ecoflex 00-30 (Smooth-On) and cured for 4 h at RT. The silicone mould was then silanized following the same procedure as for the resin mould.

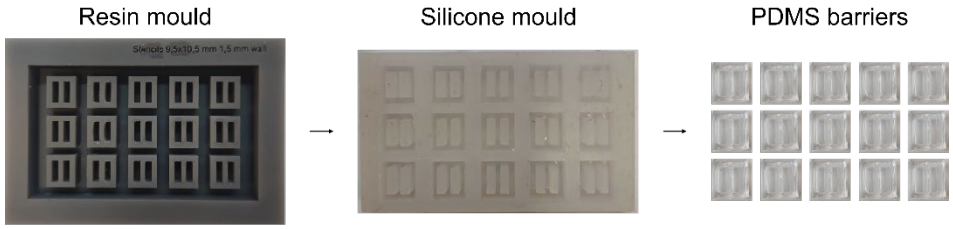

Figure 3.10. PDMS barriers fabrication process with real pictures of the resin mould, the silicone mould, and the resulting PDMS barriers.

Lastly, a mixture of Sylgard 184 Silicon Elastomer and curing agent (DowCorning) at a ratio of 10:1 w/w was prepared and poured on the intermediate mould to obtain the final PDMS barriers. Then, they were treated with 2% Pluronic® F-68 (Sigma) in PBS for 4 h, washed with PBS vigorously and sterilized under UV.

3.3.5. Immunostaining and image acquisition of fixed samples

Cells in Ibidi µ-Slides wells were fixed with 10% neutralized formalin, permeabilized with 0.5% Triton X-100 for 30 minutes, and blocked with 1% BSA, 3% donkey serum, and 0.2% Triton X-100 in PBS for 2 h at RT. Samples were then incubated with the primary antibodies against Ki67, fibronectin, laminin and collagen I (Table 3.5.1) overnight at 4°C followed by several PBS washings. Next, samples were incubated with the adequate secondary antibodies (Table 3.5.2) plus DAPI and rhodamine-phalloidin for 2 h at RT. Finally, samples were washed with PBS and mounted with Fluoromount G (Southern Biotech). Fluorescence images were acquired using a confocal laser scanning microscope (LSM 800, Zeiss) with a 10x objective (NA = 0.3, WD = 2.0) or 20x objective (NA=0.8, WD=0.55). The laser excitation and emission light spectral collection were optimized for each fluorophore. The pinhole diameter was set to 1 Airy Unit (AU).

3.3.6. Live imaging

To optimally track the epithelial cells, single cells derived from tdTomato organoids treated with 4-hydroxytamoxifen (all cells tdTomato$^+$) and from Lgr5-GFP organoids (only stem cells GFP$^+$) were mixed in a 2:1 ratio, respectively, to reduce the number of fluorescent cells and thus ease cell detection and therefore tracking. Similarly, primary fibroblasts isolated from mTmG mice and treated with 4-hydroxytamoxifen (mG$^+$) were used in the time-lapse experiments. To register the migration, an Axio Observer 7 epifluorescence inverted microscope (Zeiss) with a 10x objective or a LEICA Thunder with 10x objective (NA=0.32, WD= 11.13) or 20x objective (NA=0.4, WD=7.5-6.2), employing temperature (37°C), relative humidity (95%), and CO_2 (5%) control were used. Phase contrast, Alexa 546 and Alexa 488 channels were employed. Images were acquired every 10 min up to 48 h of culture.

3.3.7. Analysis

3.3.7.1. Fraction of cysts

Fraction of cysts respect to total number of organoids (cysts and budding organoids) was calculated by manual counting of *control* = 186 organoids of N =

7 independent experiments, *+ fibr. cond. med.* = 151 organoids of N=6 and *+ fibroblasts* = 167 organoids of N=4.

3.3.7.2. Frequency of Ki67⁺ epithelial cells

Confocal fluorescence microscopy images of Ki67 marker were used to quantify the proliferative cells at t=24h. In Imaris, nuclei were first detected with the Imaris Spot detector (diameter set to 9 µm) by manually adjusting the threshold. Next, we applied a F-Actin mean intensity filter to only analyse nuclei within the epithelial monolayer. Then, positive cells for Ki67 were filtered by applying a threshold of the mean intensity of the marker. Finally, the percentage of Ki67⁺ cells respect to the total number of cells was computed. N = 3 independent experiments for *control*, N = 2 for *+ fibr. cond. med.* and N=2 for *+ fibroblasts* were analysed.

3.3.7.3. Fraction of gap closed

In FiJi, the cell-free area was measured for frames of cell migration videos every hour and they were normalized to the final cell-free area to obtain the fraction of gap closed. N = 4 independent experiments for *control*, N = 2 for *+ fibr. cond. med.* and N=3 for *+ fibroblasts* were analysed.

3.3.7.4. Trajectories and directionality index of individual epithelial cells

The centroid trajectories of tdTomato epithelial cells were tracked using the Manual Tracking Plug-in in Fiji. Data analysis was performed using a custom-made code in Matlab (Mathworks, USA). Cell centroid positions during the experiment were defined as $r_i = r(i\Delta t)$, being Δt the time between consecutive images and r a vector. The vector difference between the initial ($t = t_0$) and the final point ($t = t_f$) is defined as the displacement vector d and its module $|| d ||$ as the net displacement. The directionality index of the trajectories is defined as $\cos(2\alpha)$, being α the angle between the displacement vector d and the gap direction, defined as the direction perpendicular to the epithelial front (Figure 3.11).

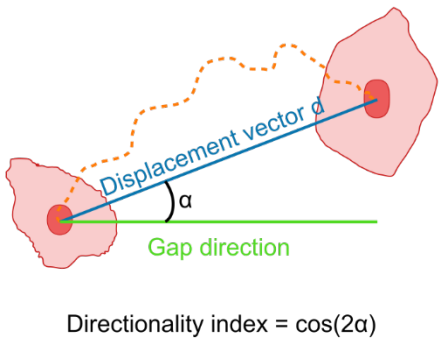

Figure 3.11. Schematic drawing of how the directionality index is obtained.

This index equals 1 when the trajectory is parallel to the direction of the gap and -1 when it is perpendicular. To analyse cell migration, we used for *control* n = 144 cells from N=5 independent experiments, for *+ fibr. cond. med.* n = 164 cells from N=4 and for + *fibroblasts* n = 208 cells from N= 5.

3.3.7.5. Velocities of epithelial and fibroblasts monolayers

For *+ fibroblasts* condition, PIVlab 2.37[90] was used to quantify the velocity of organoid-derived epithelial cells and primary fibroblasts on phase contrast time-lapse videos. Briefly, an interrogation window of 23 µm with a step of 11.5 µm was used to perform Particle Image Velocimetry (PIV) either by FFT window deformation or by ensemble correlation. Image sequencing was set as time-resolved and the resulting velocities were filtered using a standard deviation filter (8*STD) and a local median filter (threshold = 3). For the PIV analysis, n = 4 migration fronts from N = 2 independent experiments were used.

3.3.7.6. Orientation of fibroblasts and deposited proteins

For *+ fibroblasts condition*, orientation fields of fibroblasts at t=0, 24 and 48h after barrier removal and of deposited proteins at t=24h were obtained using the OrientationJ (Püspöki et al., 2016) plug-in in Fiji using a local window of 2 pixels. Next, the fraction of vector fields respect to the total was computed for each bin spanning 10 degrees. Then, polar histograms were generated in Matlab. For orientation analysis of fibroblasts, we analysed 14 pictures from N=5 independent experiments. For orientation analysis of deposited proteins, we analysed: laminin = 4 pictures from N=1 fibronectin = 4 pictures from N=2 and collagen IV = 6 pictures from N=3.

3.4. Materials and Methods for section 4

3.4.1. GelMA synthesis and characterization

Gelatine methacryloil (GelMA) was prepared following a previously described method[91–94]. Briefly, a 10% w/v gelatine solution was first obtained by dissolving gelatine from porcine skin type A (Sigma-Aldrich) in PBS (pH 7.4) at 50ºC for 2 h under stirring conditions. Methacrylic anhydride (Sigma-Aldrich) at 1.25% v/v was added at a rate of 0.5 mL min^{-1} and left to react for 1 h while stirring. The solution was centrifuged at 1200 rpm for 3 min and the reaction was stopped by adding twice the solution volume of Milli-Q water. The resulting solution was dialyzed using 6-8 kDa molecular weight cut-off membranes (Spectra/por, Spectrumlabs) in Milli-Q water at 40ºC, which was replaced every 4 h for 3 days. Then, after adjusting the pH to 7.4, the dialyzed products were frozen overnight at -80ºC and lyophilized for 4-5 days (Freeze Dryer Alpha 1-4 LD Christ). The resulting product, GelMA, was stored at -20ºC until further use.

To characterize each batch of GelMA synthesized, we used a previously stablished method in the lab consisting in determining its degree of functionalization using the Habeed Method[95], where free amino groups react with 2,4,6-Trinitrobenzene sulfonic acid (TNBS) (Sigma-Aldrich) obtaining the trinitrophenyl (TNP) chromogenic derivate (Figure 3.12). Briefly, decreasing concentration solutions (from 0.5 to 0 mg mL^{-1}) of gelatine and GelMA in sodium bicarbonate buffer ($NaHCO_3$, 0.1M; pH 8.4, in Milli-Q water) (Sigma-Aldrich) were prepared. Next, the solutions were incubated with TNBS for 2 h at 37ºC protected from light. After this time, the reaction was stopped by adding sodium dodecyl sulphate (SDS) (Sigma-Aldrich) and hydrochloric acid (HCl) (Panreac Applichem) and the absorbance of the resulting solutions was measured at 335 nm using a microplate reader (Infinite M200 PRO Multimode Microplate Reader, Tecan).

A calibration curve relating the absorbance of unmodified gelatine solutions with their percentage of free amino groups was established and fitted by a linear equation. Using this calibration curve, the unknown percentage of non-modified Lys in GelMA solutions (X) can be estimated from their absorbance. Finally, the degree of functionalization of GelMA was calculated by subtracting the remaining free amino groups in GelMA from the total amount amino groups.

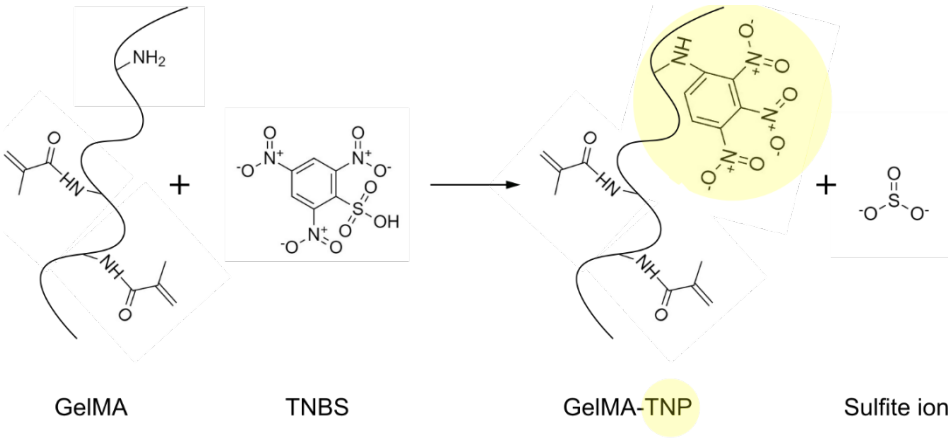

Figure 3.12. Colorimetric assay-based reaction to determine the GelMA degree of functionalization. The free amino groups of GelMA react with the TNBS, resulting in TNP, a yellow colourful product.

3.4.2. Fabrication of GelMA-PEGDA hydrogels through DLP-based bioprinting

A customized digital light processing (DLP) 3D bioprinting system was built in house by modifying a commercially available, low-cost Solus 3D printer (Junction3D), initially designed to print hard resins[75]. Shortly, as shown in

Figure 3.13, the system consists of a printing support coupled to a Z-axis motor, a customized vat with a transparent window, a beam projector with 1080p in resolution projector (Vivitek) able to crosslink the polymer using visible light, a heater to keep the prepolymer solution and the cells at 37ºC, and a short pass heat filter to protect cells from IR damage.

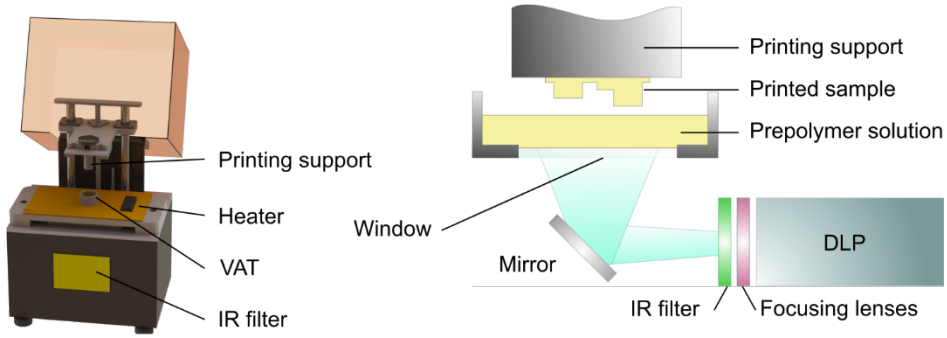

Figure 3.13. Customized 3D bioprinting system: 3D CAD model of the 3D bioprinter system (left) with detailed view of the main components (right). Adapted with permission from Torras et al.[71].

Briefly, a 3D CAD design consisting of a series of white and black patterns is first divided into layers of x µm. Then, the z motor lowers down the printing support until it is immersed in the prepolymer solution. Next, the first layer of the 3D CAD design is projected onto the photocrosslinkable prepolymer solution through the transparent vat window and the first layer gets crosslinked. Finally, the z motor rises up the printing support. This process is repeated layer by layer, forming the 3D structure in the vertical direction (Figure 3.14).

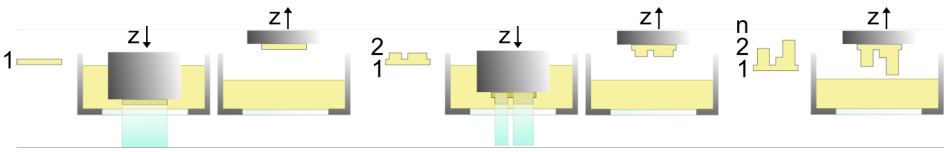

Figure 3.14. Schematic representation of the DLP procedure. Adapted with permission from Torras et al.[71].

The composition of the hydrogel prepolymer solution, or bioink, optimized in our lab, consisted in 5% w/v GelMA, 3% w/v $PEGDA_{4000}$ (Polysciences), 0.4% w/v visible-light lithium phenyl-2,4,6-trimethylbenzoylphosphinate (LAP) photoinitiator (TCI Europe) and 0.025 w/v of tartrazine (Acid Yellow 23, Sigma-Aldrich), a dye with an absorption peak at 436 nm that minimizes light overexposure. First, the bioink was prepared by dissolving all the above-mentioned components in Hank's Balanced Salt Solution (HBSS, Sigma-Aldrich) supplemented with 1% v/v Penicillin-Streptomycin (Sigma-Aldrich). The solution was protected from light at all times. Then, the bioink was pipetted into

the vat of the DLP-SLA system, which was previously warmed at 37ºC. To conduct the fabrication process, the design to be printed was programmed in CAD and the printing parameters were introduced in the software. Next, either silanized glass coverslips or Tracketch® polyethylene terephthalate (PET) membranes with 0.4 μm pore size (ipCELLCULTURE™) were attached to the printing support using a piece of PSA. Then, the printing was initiated. Once the printing process was finished (approximately after 10 min), the samples were immediately rinsed in warm PBS to remove unreacted polymer and then transferred to cell culture well plates with PBS at 4ºC in the case of plain GelMA-PEGDA or in cell culture medium in an incubator until further use.

Two types of designs were printed, namely, flat and villus-like hydrogels. For the flat hydrogels, we used a CAD design that consisted in a disc of 6 mm in diameter and 150 μm in height. Instead, for the villus-like hydrogels, we used a design made of a disc of 6 mm in diameter and 150 μm in height and pillars of of 300 μm in diameter and 700 μm in height, spaced 750 μm centre to centre.

To print both flat and villi-like hydrogels, we used these settings (Table 3.4.2):

First 2 layers	Layer thickness (μm)	15
	Exposure time per layer (s)	15
Rest of the layers	Layer thickness (μm)	13
	Exposure time per layer (s)	4

Table 3.4.2. Printing settings used to print flat or villus-like GelMA-PEGDA hydrogels.

3.4.3. Characterization of the mechanical properties of GelMA-PEGDA hydrogels

To characterize the bulk mechanical properties of the printed GelMA-PEGDA hydrogels, rheological measurements were performed. For that, hydrogels of 8 mm in diameter and 0.5 mm in height were printed using as bioink composition 5% w/v GelMA and 3% w/v PEGDA. As controls, PEGDA hydrogels (8% w/v PEGDA) and GelMA hydrogels (8% w/v GelMA) with the same total polymer concentration as the selected GelMA-PEGDA bioink were included. Samples were allowed to reach equilibrium swelling by immersion in HBSS at 4ºC for 5 days. Rheological tests were performed using a MCR302-PP08 rheometer (Anton Paar) equipped with parallel sandblasted plates of 8 mm in diameter. Measurements were performed using a sinusoidal signal and applying a sweep to the amplitude of shear strain between 0.01% and 500% while keeping the angular frequency constant to 10 s^{-1}. The temperature was maintained at 23ºC throughout the measurements. Values of storage (G') modulus were obtained as a function of the strain, from which the elastic component of the moduli, E, was

calculated considering our hydrogels as quasi-isotropic materials (Poisson's coefficient (μ) = 0.5) ($E = 2\ G'\ (1 + \mu)$[96,97].

3.4.4. Fabrication of GelMA-PEGDA hydrogels with embedded NIH-3T3 cells

To fabricate GelMA-PEGDA hydrogels with embedded NIH-3T3 cells, NIH-3T3 were passaged as detailed in section 3.1.1.1 and after centrifugation, the pellet was resuspended with the bioink at 7.5 x 10^6 cells mL^{-1}. After printing, samples were immersed in previously warmed cell culture medium. Then, samples were mounted onto Transwell inserts as explained in section 3.2.3 and cultured with NIH-3T3 culture medium, which was renewed every other day.

3.4.5. Fabrication of GelMA-PEGDA hydrogels with embedded NIH-3T3 cells and organoid-derived epithelial cells on top

For the coculture experiments of primary fibroblasts and organoid-derived epithelial cells on top of GelMA-PEGDA hydrogels, first, samples were printed following the abovementioned procedure (section 3.4.4), mounted onto Transwell inserts (section 3.2.3) and grown with NIH-3T3 culture medium, renewed every other day. On flat hydrogels, we seeded organoid-derived epithelial cells ($3x10^5$ single cells per scaffold) 4 days after the printing. On villi-like hydrogels, we seeded organoid-derived epithelial cells ($3x10^5$ single cells per scaffold) 7 days after the printing. Upon epithelial seeding, samples were cultured with ENRCV medium both in the basolateral and apical compartments and culture medium was renewed every other day.

3.4.6. Viability of embedded fibroblasts

The viability of the embedded fibroblasts within the flat GelMA-PEGDA hydrogels was determined through the calcein AM/ethidium homodimer-1 (EthD-1) LIVE/DEAD® viability/cytotoxicity assay (Invitrogen). Briefly, at days 1 and 7 after printing, cell-laden hydrogels were demounted from the Transwell® inserts, washed and incubated with EthD-1 at 4 µM EthD-1, calcein AM at 2 µM and Hoechst 33342 (5 µg mL^{-1}) (Invitrogen) for 20 minutes in the incubator. Samples were then vigorously washed, mounted and imaged immediately using a confocal laser scanning microscope (LSM800, Zeiss). Manual cell counter plugin in ImageJ software was employed for cell viability quantification.

3.4.7. Histological sections

To perform histological sections of the bioprinted scaffolds while preserving the 3D architecture of the hydrogels, samples were embedded following a protocol previously developed in our group[98]. Briefly, after fixation with 10% neutral buffered formalin solution at RT for 30 min, samples were demounted from Transwell inserts and submerged in the embedding solution containing 10% w/v of PEGDA 575 kDa ($PEGDA_{575}$) (Sigma-Aldrich) and 1% w/v of Irgacure D-2959 in PBS and kept overnight at 4ºC. Then, a 2 mm thick PDMS stencil with a central round pool of 12 mm was attached to a plastic support and filled with the embedding solution. The construct was then irradiated for 40 s at 25 mW cm^{-2} of power density using UV light at 365 nm wavelength in a MJB4 mask aligner. The resulting $PEGDA_{575}$ block was carefully removed, flipped, and placed back in the pool. The hydrogel to be embedded was then placed inside the pool, embedding solution was added and a coverslip was placed on top. After exposing for 200 s, the whole construct was flipped, more embedding solution was added, and a second coverslip was placed on top. After a second exposition of again 200 s, the hydrogel was successfully embedded in a $PEGDA_{575}$ block. Then, samples were immersed overnight in 30% sucrose solution (Sigma-Aldrich) at 4°C for cryoprotection, further embedded in optimal cutting temperature (OCT) compound (Tissue-Tek® O.C.T. Compound, Sakura® Finetek) and stored at -80 ºC for at least 12 h. Finally, they were cut with a cryostat (Leica CM195) and histological cross-sections of ~7 µm thickness were recovered, attached onto glass coverslips, air dried and stored at -20ºC until use.

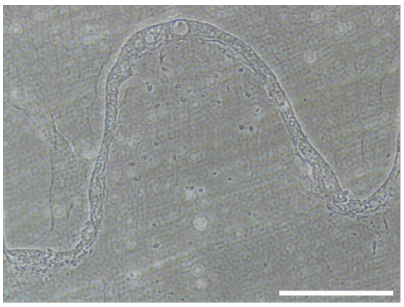

Figure 3.15. Histological section of a GelMA-PEGDA hydrogel with embedded NIH-3T3 fibroblasts and organoid-derived epithelial cells on top at day 14 after printing. Scale bar: 250 µm.

3.4.8. Immunostaining and image acquisition of fixed samples

To immunostain the histological cross-sections, first they were taken out from the -20ºC freezer to thaw and dry at RT overnight. For some antibodies (section 3.4.1, table 3.5.1), samples were first subjected to an antigen retrieval treatment consisting in submersion into a citrate buffer solution (10 mM citrate and 0.05

% v/v of Tween20 in MilliQ water, pH 6) at 85ºC for 5 h. Then, they were permeabilized with 0.5% Triton-X at RT for 1 h and blocked with 1% BSA, 3% donkey serum, and 0.3% Triton-X first at RT for 4 h and then at 4ºC overnight. Samples were then incubated with selected primary antibodies (Table 3.5.1) diluted in 0.1% BSA, 0.3% donkey serum, and 0.2% Triton-X for 8h at RT and overnight at 4ºC. After several washing steps with PBS, samples were incubated with the adequate secondary antibodies (Table 3.5.2) together with rhodamine-phalloidin and DAPI for 8 h at RT. Finally, samples were mounted by placing a drop of Fluoromount G and a coverslip on top.

To immunostain bulk samples, first cells were fixed with 10% neutralized formalin, demounted from Transwell inserts and placed in new well plates. Then, they were permeabilized with 0.5% Triton X-100 for 1h and blocked with 1% BSA, 3% donkey serum, and 0.2% Triton X-100 in PBS for 4 hours at RT. Samples were incubated with the selected primary antibodies overnight at 4°C followed 2h at RT. After several PBS washings, samples were incubated with the adequate secondary antibodies plus DAPI and rhodamine-phalloidin for 2h at RT. Right before imaging, samples were then mounted in PBS on coverslips using 1.5 mm PDMS spacers to avoid the smashing of the villus-like microstructures.

Fluorescence images of either kind (histological sections or bulk samples) were acquired using a confocal laser scanning microscope (LSM 800, Zeiss) with a 5x objective (NA=0.16, WD=12.1), 10x objective (NA=0.3, WD=2.0), 20x objective (NA=0.8, WD=0.55) or 40x objective (NA=1.4, WD=0.13). The pinhole diameter was set to 1 Airy Unit (AU). Alternatively, a Nikon LIPSI microscope with a 10x objective (NA=0.3, WD=5.2) was used. The laser excitation and emission light spectral collection were optimized for each fluorophore.

3.4.9. Live imaging

To see the dynamics of the interaction between the fibroblasts and the epithelial cells through live imaging, first the setup of the samples had to be adapted to improve the optics by minimizing the distance from the objective to the sample. Briefly, flat GelMA-PEGDA hydrogels with embedded LINTERNA NIH/3T3 fibroblasts were printed on silanized 13 mm coverslips as described in section 3.4.2. The 14 mm ø coverslip of a 35 mm MatTek petri dish was removed and a 18x18 mm rectangular double-sided PSA with a 10 mm ø hole was stuck on its place. Then, the coverslip was stuck on the PSA and a pool of PDMS was used to reduce the volume of medium needed. Four days after hydrogel printing, *mT* organoid-derived cells were obtained as detailed in section 3.1.2.2, resuspended with 400 µL of the appropriate medium and seeded on the fibroblast-laden

hydrogels. One day after the seeding, samples were transferred to a Nikon LIPSI microscope, a platform based on the Eclipse Ti2 inverted microscope, equipped with a Yokogawa W1 confocal spinning disk unit, a Prior stage, two Prime BSI Photometrics sCMOS cameras and NIS Elements AR 5.30.05 software, with control of CO_2 (5%) and temperature (37ºC). Four positions were taken with the Super Plan Fluor 20x dry objective (NA = 0.7, WD = 2.3) and images were taken every 15 min for 12 h. One of the two cameras was used to detect simultaneously the cytosolic GFP of fibroblasts, and TRICT, to visualize the membranous tomato of organoid-derived epithelial cells. The other camera was used to detect with brightfield the central plane. The laser power, exposure time and z-step were carefully optimized.

3.4.10. Analysis

3.4.10.1. Fibroblasts' viability in flat hydrogels

To quantify the viability of fibroblasts embedded in GelMA-PEGDA hydrogels at days 1 and 7 after printing, we simply employed a manual cell counter plugin in FiJi. For day 1, we analysed n = 7 images of samples from N = 2 independent experiments. For day 7, we analysed n = 8 images of samples from N = 2 independent experiments.

3.4.10.2. Surface coverage

On GelMA-PEGDA hydrogels with embedded fibroblasts, we quantified the percentage of surface covered by fibroblasts by acquiring F-actin fluorescence images through a confocal microscope (LSM 800, Zeiss) with 5x objective and performing the maximum intensity projection in FiJi. Then, we applied an over/under threshold to obtain a binary mask and we measured the area (covered area, CA). Finally, we normalized it by the total area (TA) to obtain the surface coverage. For day 4, we analysed n = 1 sample from N = 1 independent experiment. For day 7, we analysed n = 3 samples from N = 3 independent experiments. For day 9, we analysed n = 2 sample from N = 2 independent experiments. For day 11, we analysed n = 2 sample from N = 2 independent experiments.

To quantify the percentage of surface covered by epithelial cells in the coculture samples, we could follow the same procedure as to quantify the surface coverage of samples with only fibroblasts as there was sufficient difference in F-actin intensity between fibroblasts and epithelial cells in the coculture samples to only retrieve the signal belonging to epithelial cells when the threshold was applied. For day 1, we analysed n = 1 sample from N = 1 independent experiment. For day 3, we analysed n = 3 samples from N = 3 independent

experiments. For day 5, we analysed n = 2 sample from N = 2 independent experiments. For day 7, we analysed n = 2 sample from N = 2 independent experiments.

3.4.10.3. Fibroblasts distribution within flat hydrogels

To quantify the percentage of cells in the surface vs in the bulk of the flat hydrogels, we first acquired F-actin and Nuclei images through a confocal microscope (LSM 800, Zeiss) with a 20x objective (NA=0.8, WD=0.55). Then, total number of cells, number of cells in the bulk and number of cells in the surface were manually computed to obtain the respective percentages. For this quantification, we used n = 1 sample from N = 1 independent experiment for each day (7, 9 and 11).

3.4.10.4. Fibroblasts distribution within villi-like hydrogels

To quantify the distribution of fibroblasts within the pillars over time, we first acquired F-actin and Nuclei images through a Nikon LIPSI microscope with a 10x objective (NA=0.3, WD=5.2). First, images were subdivided into z stacks that contained one single centred pillar. Next, using Imaris, nuclei were detected with the Spot detector (diameter set to 9 µm) by manually adjusting the quality threshold. Afterwards, we exported the x, y and z coordinates of each nucleus. Then, we developed a customized Matlab script to first, normalize the z values of each pillar to go from 0 to 1, set the x and y origin in the centre of the image, transform the cartesian coordinates into cylindrical ones, and compute a histogram of the proportion of cells as a function of the position within the height axis and the radius axis of each pillar. Results were plotted as a colormap. For day 7, we analysed n = 4 pillars from N = 1 independent experiment. For day 10, we analysed n = 8 pillars from N = 1 independent experiment. For day 14, we analysed n = 8 pillars from N = 1 independent experiment.

3.4.10.5. Elongation index of NIH/3T3 fibroblasts in the presence or absence of epithelial cells

To quantify the elongation index of NIH/3T3 fibroblasts' nuclei in the villi-like hydrogels with embedded fibroblasts and with or without epithelial cells on top at day 14 after printing, we used images of histological cuts and obtained masks of each nuclei employing StarDist[99], a cell detection method that can be implemented as a plugin in FiJi. After manually selecting the adequately detected nuclei and only those in the outline of the hydrogel, we computed the elongation index as $(major\ axis - minor\ axis)/(major\ axis + minor\ axis)$, 0 corresponding to a circle, 1 to a line. For this analysis, we quantified n = 1 sample from N = 1 independent experiment.

3.5. Antibodies

3.5.1. Primary antibodies

NAME	TYPE	SOURCE	DILUTION	ANTIGEN RETRIEVAL IN CUTS
Anti-α-smooth muscle actin	Mouse Monoclonal IgG2a	Abcam ab7817	1:200	N.A.
Anti-β-catenin	Rabbit IgG pAb	Abcam ab2365	1:100	N.A.
Anti-β-catenin	Mouse IgG1	BD Transduction Laboratories 610154	1:200	Yes
Anti-collagen type I	Mouse IgG mAb	Thermo Fisher Scientific MA1-26771	1:200	N.A.
Anti-collagen type IV	Goat	Biorad 134001	1:200	Yes
Anti-cytokeratin 20	Rabbit IgG mAb	Abcam ab109111	1:100	N.A.
Anti-cytokeratin 20 (Clone Ks20.8)	Mouse IgG2a mAb	Dako M7019	1:100	N.A.
Anti-desmin	Rabbit pAb	Abcam ab15200	1:200	N.A.
Anti-fibronectin	Rabbit	Sigma F3648	1:200	N.A.
Anti-fibronectin	Mouse IgG1 mAb	Sigma F7387	1:200	N.A.
Anti-E-cadherin	Mouse IgG2 a K	BD Biosciences 610181	1:100	Yes
Anti-FABP1	Rabbit IgG	Sigma HPA02875	1:50	N.A.
Anti-GFP	Goat IgG pAb	Abcam ab6673	1:100	N.A.
Anti-ki67	Rabbit IgG mAb	Abcam ab16667	1:100	Yes
Anti-ki67	Mouse IgG1 mAb	BD Pharmingen 550609	1:100	N.A.
Anti-laminin	Rabbit Polyclonal	Abcam ab11575	1:200	Yes
Anti-lysozyme	Rabbit anti-Human	Dako A0099	1:100	N.A.
Anti-vimentin	Mouse IgG1 mAb	DSHB 40E-C	1:20	N.A.
Anti-vimentin	Rabbit IgG	Cell Signaling #5741	1:200	No
Anti-vimentin	Rabbit mAb	Abcam ab92547	1:200	N.A.
Anti-YAP	Mouse IgG2a mAb	Santa Cruz Biotech sc-101199	1:200	No

Table 3.5.1 List of primary antibodies used for immunostainings throughout the thesis.

3.5.2. Secondary antibodies

TYPE	MADE IN	NAME	SOURCE	DILUTION ICC
Anti-mouse	Donkey	Alexa Fluor™ 647 donkey anti-mouse IgG (H+L)	Invitrogen A-31571	1:500
	Donkey	Alexa Fluor™ 568 donkey anti-mouse IgG (H+L)	Invitrogen A-10037	1:500
	Donkey	Alexa Fluor™ 488 donkey anti-mouse IgG (H+L)	Invitrogen A-21202	1:500
Anti-rabbit	Donkey	Alexa Fluor™ 647 donkey anti-rabbit IgG (H+L)	Invitrogen A-31573	1:500
	Donkey	Alexa Fluor™ 568 donkey anti-rabbit IgG (H+L)	Invitrogen A-10042	1:500
	Donkey	Alexa Fluor™ 488 donkey anti-rabbit IgG (H+L)	Invitrogen A-21206	1:500
Anti-goat	Donkey	Alexa Fluor™ 647 donkey anti-goat IgG (H+L)	Invitrogen A-21447	1:500
	Donkey	Alexa Fluor™ 568 donkey anti-goat IgG (H+L)	Invitrogen A-11057	1:500
	Donkey	Alexa Fluor™ 488 donkey anti-goat IgG (H+L)	Invitrogen A-11055	1:500

Table 3.5.2. List of secondary antibodies used for immunostainings throughout the thesis.

DAPI (1:1000, Thermo Fisher Scientific).

Rhodamine-phalloidin (3.5:500, Cytoskeleton).

3.6. Statistics

No statistical methods were used to predetermine sample size. Measurements were performed on experimental replicates (samples, pillars or images) (n) obtained in different independent experiments (N) and are detailed in the corresponding analysis section and summarized in the corresponding figure caption. Data presentation (as mean, as mean ± standard deviation (SD) or as mean ± standard error of the mean (SEM)) is defined at the corresponding figure caption. Statistical tests were performed using GraphPad Prism 9 (GraphPad software, La Jolla, CA, USA) and are detailed in figure captions.

4. Results

4.1. Engineering a 3D crypt-like model of the intestinal epithelium

The architecture of the intestinal tissue not only consists in finger-like protrusions called villi but also invaginations into the lamina propria called crypts, which is where stem cells, Paneth cells and transit amplifying cells are located. The shape of these crypts is of crucial importance to protect the stem cells hosted within from any biological or physical hazard present in the lumen. In the lab, we previously developed a photolithography-based technique that allowed the fabrication of villus-like PEGDA-AA hydrogels[69]. However, crypt-like structures were not included in the model. Therefore, we aimed to fabricate crypt-like PEGDA-AA hydrogels and to use organoid-derived cells as epithelial source, thus engineering an upgraded *in vitro* model of the intestinal epithelium.

4.1.1. Lithography-based dynamic photopolymerization allows the fabrication of crypt-like structures with native-like dimensions

The in-house photopolymerization technique that yielded villus-like PEGDA-AA hydrogels was carefully optimized to obtain crypt-like structures. Briefly, PEGDA-AA prepolymer solutions were exposed to UV light through transparent photomasks with black circular windows corresponding to crypts. Photomasks with crypt diameters ranging from 50 to 100 μm and exposure times between 50 and 70 s were tried. For each photomask design, we obtained an optimal exposure time that yielded hydrogels with crypt like structures after swelling (Table 4.1.1).

Crypt diameter (μm)	50	75	100
Exposure time (s)	50	70	10+50

Table 4.1.1. Optimised exposure time (s) for each crypt diameter (mm). In the case of 100 μm crypts, we did two exposures, a first one of 10 s without the photomask, and a second one of 50 s with the photomask.

We then assessed crypt's morphology by imaging PEGDA's autoflourescence through confocal microscopy (Figure 4.1.1). We found that crypts displayed a conical shape, being wider than the actual mask in the upper part while smaller than the actual mask at the bottom end. As in the case of villi fabrication, this effect is typically attributed to oxygen diffusion[69].

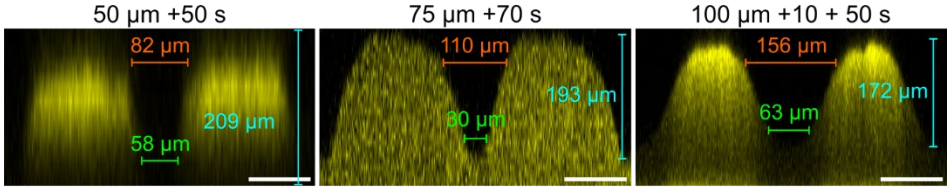

Figure 4.1.1. Orthogonal projections of representative crypt-like cavities in hydrogels obtained with photomasks of 50, 75 or 100 µm diameter crypts with 50, 70 or 10+50 s exposure time, respectively, after swelling. Signal corresponds to PEGDA autofluorescence. Top diameter (orange), bottom diameter (green) and height (cyan) measurements are displayed. Scale bars: 100 µm.

4.1.2. Hydrogel functionalization with ECM proteins unveils partially crosslinked polymer inside the crypt-like cavities

After swelling, crypt-like hydrogels were functionalized with proteins or mixtures of proteins characteristic of the intestinal basement membrane that typically allow epithelial adhesion and growth (collagen-I, fibronectin, laminin and Matrigel), as detailed in section 3.2.4. Next, we characterized the functionalization by performing immunostainings against the different proteins and analysing them through confocal microscopy (Figure 4.1.2). We could observe that the functionalization protocol followed allowed a successful coupling of all the ECM proteins or mixtures of proteins tested. However, in the cases of fibronectin, laminin and Matrigel, we could see that the signal corresponding to the protein was localized at the flat region of the hydrogel but not at the crypts, suggesting that the coupling reaction was unsuccessful within the cavities. The signal corresponding to collagen I could also be localized at the flat region of the hydrogel, but it was also found bridging the area over the crypts. To explain this observation, we raised two hypotheses: since collagen is highly fibrillar, the protein bridging the crypt cavities might be forming part of a mesh structure that has anchoring points at each side of the crypts; another possibility is that there was some remaining material within the crypts thus preventing the proteins to enter in the cavities and sustaining the collagen at the entrance of the crypt.

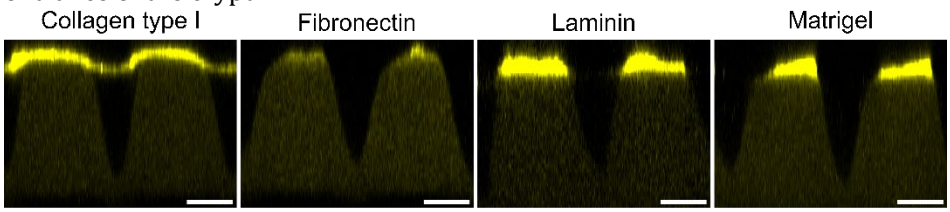

Figure 4.1.2. Orthogonal projections of representative crypt-like hydrogels obtained with the photomask of 75 µm diameter crypts with 70 s exposure time immunostained for collagen type I, fibronectin or laminin (both to visualize laminin and Matrigel). Scale bars: 50 µm.

To elucidate this, we mixed the standard prepolymer solution of PEGDA-AA with fluorescent beads and we fabricated crypt-like hydrogels, as we routinely did.

After swelling, we imaged the hydrogels through confocal microscopy and we observed that crypts appeared similar to the ones fabricated without beads, suggesting that their presence does not interfere with hydrogel polymerization. Then, we focused on the localisation of fluorescent beads to know if there was material in the cavities. We noticed beads trapped in the bulk material of the hydrogel, but we also observed fluorescent beads suspended in the empty crypt cavities (Figure 4.1.3). This result indicates that, within the crypts, there was some material. It may be polymer not crosslinked enough to display autofluorescence and thus be seen when scanning the samples with the confocal microscope but crosslinked enough to trap beads. We thus speculate that this remaining polymer in the crypts is preventing the coupled proteins to go through.

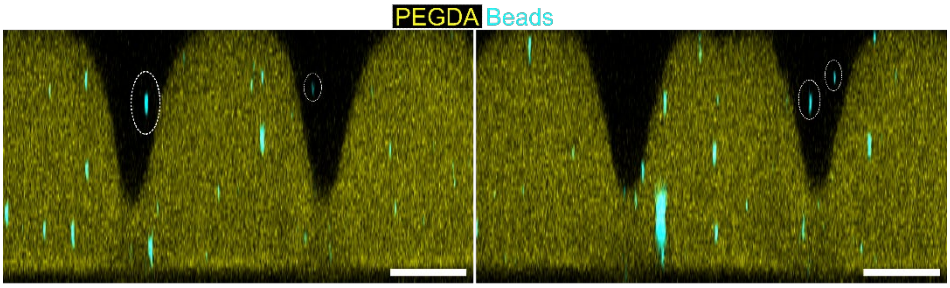

Figure 4.1.3. Orthogonal projections of representative crypt-like hydrogels (PEGDA autofluorescence) with embedded fluorescent beads obtained with the photomask of 75 µm diameter crypts with 70 s exposure time. Dotted areas highlight beads in the crypts. Scale bars: 100 µm.

To overcome this problem, we tried several different strategies: (i) to increase the washing steps before protein functionalization, (ii) to centrifuge the plates where we had the scaffolds at 3000 g for 10 min right after protein incubation, and (iii) to apply vacuum for 30 min right after protein incubation. Unfortunately, none of these attempts yielded a different outcome than the one obtained before.

4.1.3. Larger crypt features allow the formation of organoid-derived monolayers with crypt-like valleys

Next, we thought of ways to prevent that the fabricated holes were filled with partially-crosslinked material, and we opted for fabricating bigger crypts. By doing so, we hypothesized we would ease the wash out of this partially-crosslinked polymer upon the multiple washes we subjected the hydrogels to. In detail, we designed new photomasks with black circular regions corresponding to the crypts of 150, 250 and 300 µm, with a pitch of 300, 350 and 500 µm, respectively. As in the case of the smaller crypts, we observed that, after swelling, these new bigger crypts could also be fabricated through this photolithography-based process by optimising the exposure time. However, the

conical shape observed in the previous set of sizes (50 µm, 75 µm and 100 µm) was lost and more square-shaped crypts appeared when imaging PEGDA's autofluorescence.

Next, we opted to functionalize them with collagen I because it was the only protein with which we could see signal in the cavities. Then, we immunostained the samples against the protein and we observed again a mild fluorescence signal suspended in the cavities of all the designs tested (Figure 4.1.4), possibly coinciding with where there was partially-crosslinked material. Thus, with these new crypts, we could not totally avoid this phenomenon of having partially-crosslinked polymer trapped in the cavities. Still, in these bigger crypts the protein was able to penetrate longer lengths (Figure 4.1.4) than in the smaller crypts (Figure 4.1.2 (left)), probably because the cavities were now wider and deeper.

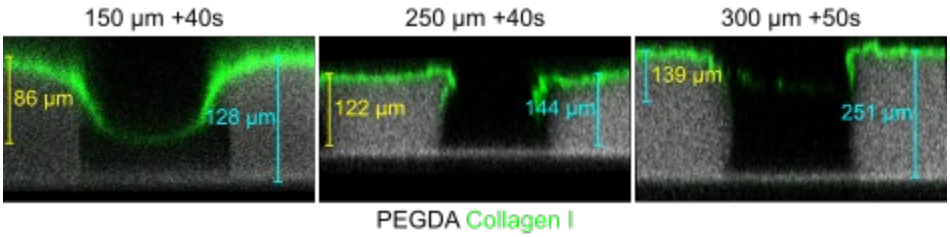

Figure 4.1.4. Orthogonal projections of representative crypt-like hydrogels fabricated with photomasks consisting of black circular windows of 150, 250 and 300 µm, with a pitch of 300, 350 and 500 µm, and exposing for 40, 40 and 50 s, respectively. Crypts depths were calculated using the signal from PEGDA autofluorescence. Measurements of the maximal depths reached by collagen I are displayed.

Therefore, we wanted to assess if those cavities were capable of sustaining the growth of an epithelial monolayer on top, and if we would be able to observe monolayer conformity with the crypt-like PEGDA-AA hydrogels. For that, hydrogels were fabricated, mounted in Transwell inserts and functionalized with collagen I. Then, mT organoid-derived single epithelial cells were seeded on the hydrogels and let grow for one day. We observed that the protein chose to functionalize the hydrogels (collagen I) allowed a successful attachment of the primary organoid-derived epithelial cells. Upon samples fixation and immunostaining, we observed that in all cases, single cells had successfully attached and formed a monolayer on the flat part of the hydrogels (Figure 4.1.5). In the case of epithelial cells grown on top of crypts of 150 µm, we could see the formation of a continuous monolayer all over the scaffolds, i.e, not only flat regions were covered by epithelial cells but also crypt-like regions, resulting in a sinusoidal or wavy monolayer (Figure 4.1.5 (a, left)). Still, when we attempted to keep these cultures for two days more, monolayers started to break and detach, especially in the crypt regions (data not shown). This result goes in line

with the fact that in the cavities, there was a very weak support for the protein coupled (Figure 4.1.4 (left)) and thus, for the monolayer above (Figure 4.1.5, (a, left) and (b)).

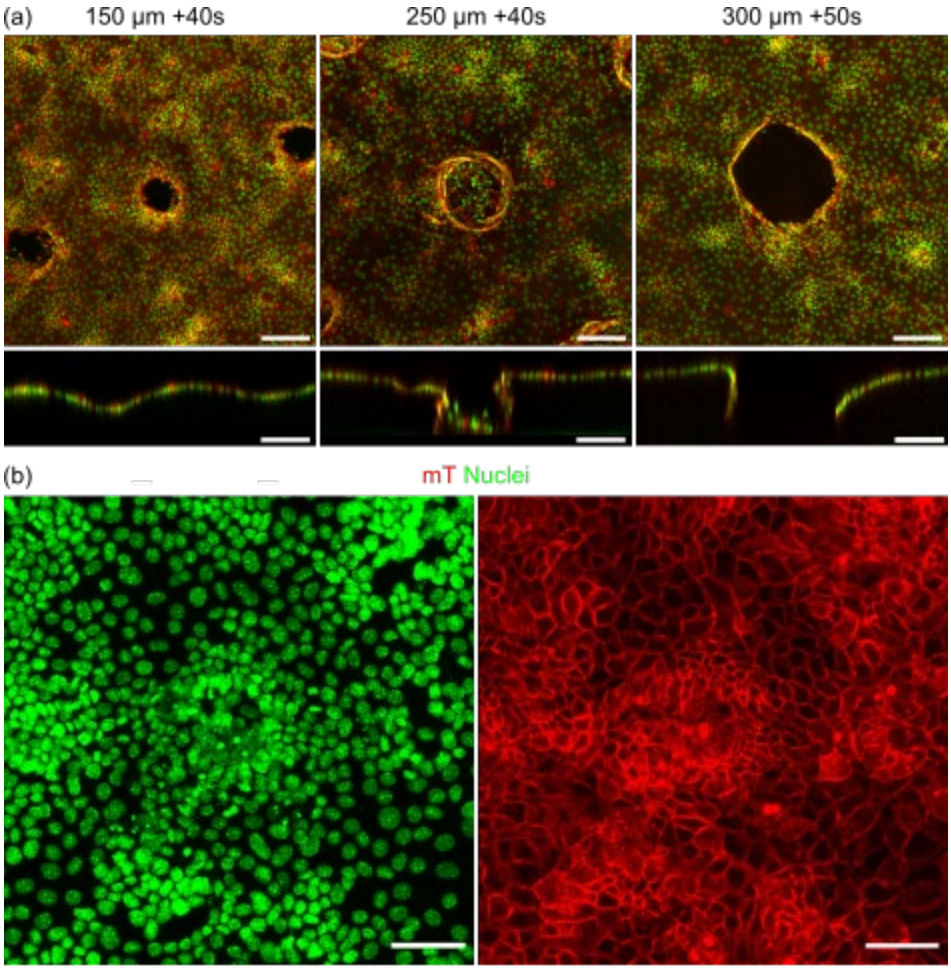

Figure 4.1.5. (a) Maximum intensity and orthogonal projections of mT organoid-derived monolayers on top of crypt-like hydrogels fabricated with photomasks consisting of black circular windows of 150, 250 and 300 µm, with a pitch of 300, 350 and 500 µm, and exposing for 40, 40 and 50 s, respectively. Scale bars: 100 µm. (b) Zoom-in of 150 µm crypts. Scale bars: 50 µm. Samples immunostained for DAPI (nuclei).

In the case of 250 µm crypts, cells were able to reach the bottom of the cavities, but they were not able to form a continuous monolayer (Figure 4.1.5, (a, middle panel). Instead, we could observe that most cells within the crypts were clearly detached, possibly because of the lack of protein, and thus, cell adhesion cues. Finally, when organoid-derived cells were cultured on 300 µm crypts, they were able to grow on the walls of the cavities until a certain depth, point below which they could not attach to the hydrogel (Figure 4.1.5, (a, right panel)), perfectly

coinciding with the region where there was no protein coupling (Figure 4.1.4, (a, right panel). These results suggest that the use of photomasks with bigger windows eases the removal of semi-crosslinked polymer trapped within the holes. Despite not achieving complete wash out, we have shown how epithelial monolayers can be formed on these microstructured hydrogels.

Altogether, these experiments demonstrate that crypt-like microstructures can be fabricated using PEGDA-AA through a photolithography-based approach. However, the polymerization process leaves semi-crosslinked hydrogel trapped in the cavities, which, in turn, impedes a proper protein functionalization. Still, organoid-derived monolayers can be grown on these collagen I-functionalized crypt-like hydrogels.

4.2. Organoid-derived monolayers under biochemical gradients of the stem cell niche display tissue-like cell compartmentalization in a 3D villus-like model of the intestinal epithelium

As mentioned above, the intestinal tissue protruding into the lumen called villi allows to maximise the surface of absorption, while invaginations into the lamina propria called crypts protect the most precious cells, the stem cells, from the hazards present in the lumen. However, the characteristic 3D architecture of the intestinal epithelium has another fundamental function: to provide a physical scaffolding for biochemical gradients to be formed and maintained [100]. Signalling gradients of Wnt, BMP and EGF are responsible for the compartmentalization of proliferative cells within the crypts and differentiated cells within the villi. In spite of the relevance of biochemical gradients of the ISC niche *in vivo*, up to date, there are no platforms allowing a systematic and quantitative study of these gradients in an *in vitro* model that is also apically accessible, exhibits native mechanical properties and mimics the 3D architecture of the tissue. In this context, in this second results section, we thus attempted to engineer a model of the intestinal epithelium that recapitulated the villus-like topology, allowed the establishment of gradients and enabled the growth of organoid-derived monolayers. Then, we evaluated how the presence and variability of gradients affected the growth and organization of the intestinal epithelial cells. The work presented in this section has been published in Advanced Healthcare Materials[86].

4.2.1. The fabricated 3D villus-like PEGDA-AA hydrogels have anatomical dimensions, native tissue-like elasticity and a mesh size that allows the diffusion of the factors of the ISC niche

The 3D villus-like hydrogel scaffolds were fabricated following a technique previously developed in the lab based on free radical photopolymerization[69,85,86,101]. First, we exposed the prepolymer solution containing PEGDA and AA to UV light through a photomask to obtain hydrogels with villus-like microstructures with a density of 16 villus-like pillars mm^{-2}, thus in the range of the density of the native mouse villi (20-40 villi mm^{-2})[1,102,103]. After hydrogel swelling, we measured the dimensions of the villus-like microstructures and found that the base height was 185 ± 24 μm and the villus-like pillars height was 350 ± 44 μm (Figure 4.2.1), therefore resembling the anatomical dimensions of the small intestine villi, reported to range between 130 and 330 μm[62].

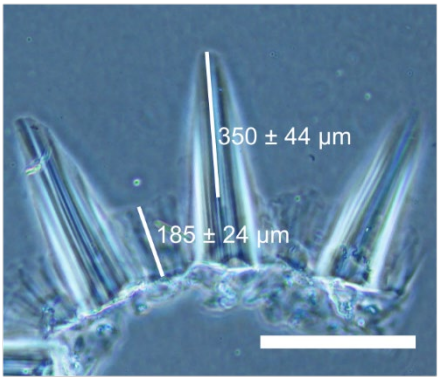

Figure 4.2.1. Bright-field microscope image of the cross-section of the villus-like hydrogels. The height of the microstructures was measured to be 350 ± 44 µm. N = 3, n = 4, pillars = 147. The height of the base was measured to be 185 ± 24 µm. N = 4, n = 5, pillars = 110. Mean ± SD. Scale bar: 400 µm.

The hydrogel bulk elasticity was previously measured in the lab through a compression test and found to be 2.5 – 10.9 kPa[85], also in accordance with the reported elastic properties of small intestinal tissue[49]. The bulk mesh size of the hydrogels was also previously estimated in the lab[85] using the Flory-Rehner equilibrium swelling theory modified by Peppas and Merrill in the presence of water[104,105]. The average mesh size was estimated to be between 8.3 ± 0.2 nm and 11.7 ± 0.2 nm, in agreement with the values reported in the literature[104,106]. Considering that the estimated hydrodynamic diameter (d_h) of the main ISC niche biochemical factors of interest (EGF, R-Spondin 1, Noggin, Wnt2b) range from 3.0 to 7.2 nm (see Table 4.2.1), the fabricated hydrogels were regarded as suitable for the diffusion of these proteins. Overall, we could show that the fabricated 3D villus-like PEGDA-AA hydrogels have anatomical dimensions, native tissue-like elasticity and a mesh size that appears compatible with the diffusion of the factors of the ISC niche.

ISC niche factor	Estimated d_h (nm)
EGF	2.94[107]
R-Spondin 1	4.70[107]
Noggin	7.20[108]
Wnt2b	5.96[107]

Table 4.2.1. ISC niche biochemical factors and their corresponding estimated hydrodynamic diameter (d_h).

4.2.2. Steady-state biochemical gradients can be formed along the villus vertical axis within the PEGDA-based hydrogels

In order to characterize the gradients formed along the vertical axis of villus-like PEGDA hydrogel microstructures, a microfluidic device allocating the hydrogel was engineered, allowing the imaging of the gradient of fluorescently labelled BSA through Light Sheet Fluorescence Microscopy (LSFM). Briefly, Texas Red – BSA was flown into the chip through the channel to the source chamber. By diffusing across the membrane and the hydrogel, a BSA gradient was created along the villus vertical axis of the samples. After 3h of protein loading, time-lapse videos exciting with 568 nm laser were acquired for 90 minutes to visualize BSA, together with 488 nm laser excitation to visualize the hydrogel autofluorescence.

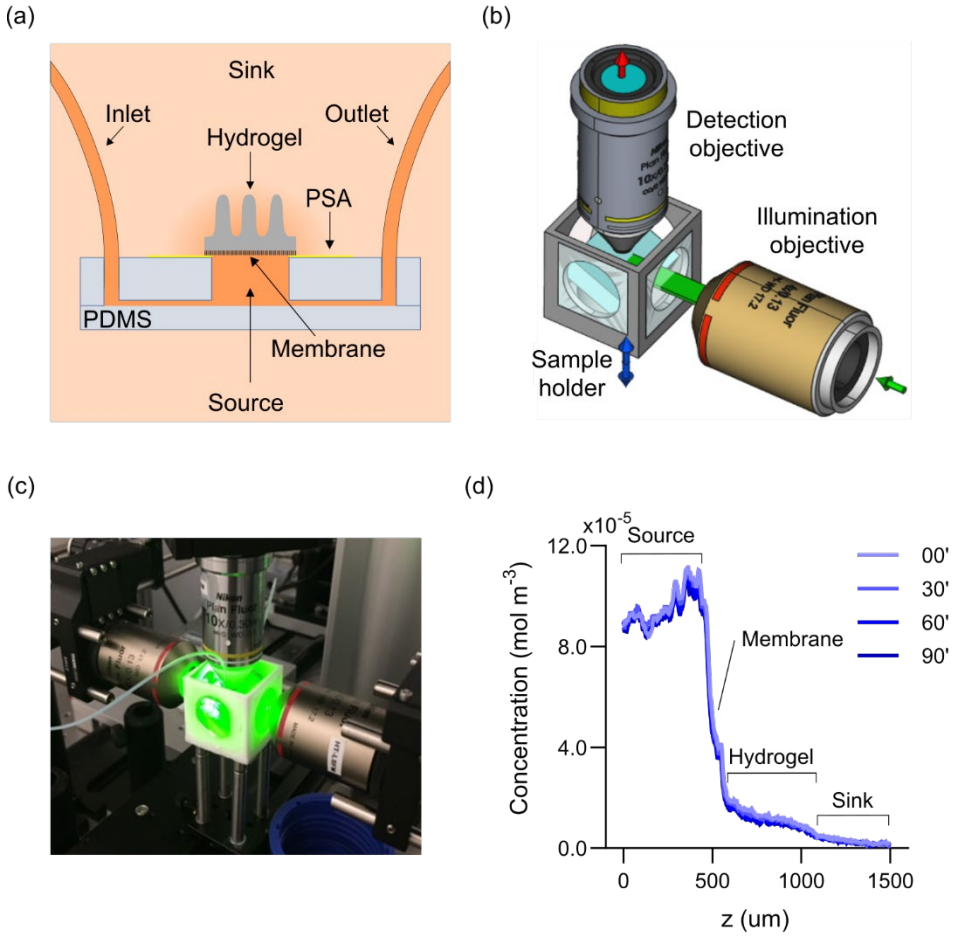

Figure 4.2.2. (a) Schematic drawing of the microfluidic chip allocating villus-like PEGDA-AA hydrogel. Schematics (b) and picture (c) of the LSFM setup used, where the detection was performed in an up-right configuration. (d) Graph showing the concentration profiles of Texas Red-labeled BSA taken across the vertical axis of the pillars at different times points.

Intensity levels were then correlated with BSA concentrations. The gradient profiles were stable along the time of acquisition (Figure 4.1.2 (d)), indicating that the loading time used was sufficient to reach a pseudo steady state. On the other hand, these experiments proved useful to find out that there was a significant amount of protein getting accumulated at the PET membrane-hydrogel interface (Figure 4.1.2 (d)), information we considered when calculating the source concentrations to use for each protein.

4.2.3. The *in silico* model developed fits well the experimental data and allows the prediction of gradients of ISC factors

In order to be able to estimate the spatio-temporal gradients of our molecules of interest (EGF, R-Spondin 1, Noggin and Wnt2b) created along the villus-like PEGDA-AA hydrogels, an *in silico* model using finite element method (FEM) was developed. Briefly, the diffusion of proteins over time and space was described by Fick's second law and simulated employing the 'Transport of diluted species' module of COMSOL Multiphysics software (version 5.5). 3D forms were reduced to 2D geometries assuming axial symmetry. The geometry was composed of two media: the PEGDA-AA hydrogel and the surrounding aqueous solution. For each medium, the corresponding diffusion coefficient values of each species were estimated [85,86]. The gradients formation was modelled in a system composed by a source, the hydrogel, and a sink compartments. In agreement with the experiments performed, BSA was chosen as the model protein to develop the model, and the villi geometry and the protein accumulation observed at the membrane-hydrogel interface during the LSFM acquisition were accounted for in the model. The concentration profiles computed along the axis spanning the source, the hydrogel and the sink predicted stable gradients within the timeframe studied, in excellent agreement with the experimental data (Figure 4.2.3 (a)). Moreover, the simulations showed that periodic medium replenishment every 24 h would establish stable gradients. Then, the *in silico* model developed was used to predict the concentration of each ISC niche biochemical factor (Noggin, R-Spondin 1, and EGF) along the villus axis of the hydrogels in the cell culture setup when asymmetric concentrations (factors only delivered through the basolateral side) were applied. For instance, when the source concentrations were doubled in the simulations (Noggin 2.0 and R-spondin 1 2.0), rather than the slopes changing, what we observed was that the concentrations in the entire geometry were also doubled (Figure 4.2.3 (b)). Therefore, in the pseudo steady state considered, this system enabled the regulation of the absolute concentrations that the cells can sense, while keeping the relative change between the base and the tip constant.

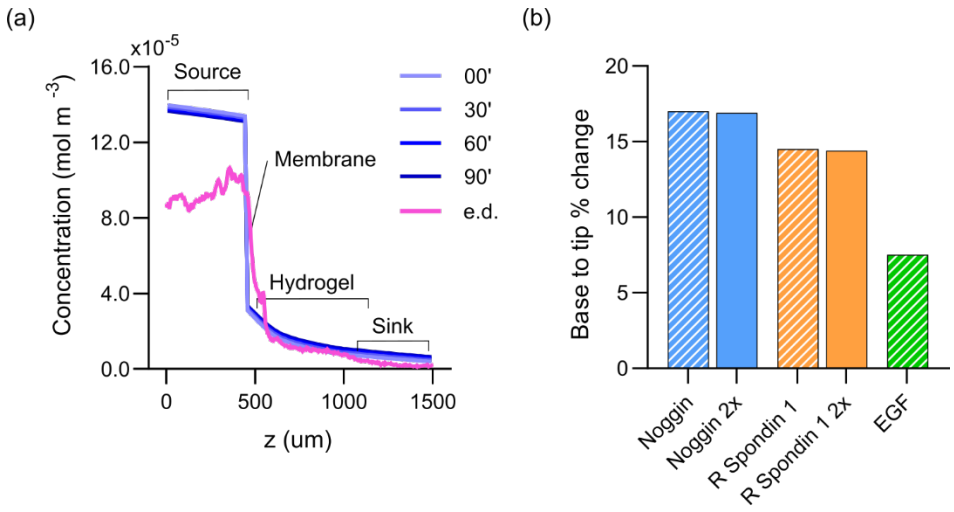

Figure 4.2.3. (a) Graph showing the concentration profiles of the model protein BSA predicted by the FEM simulations together with the experimental data (e.d.) corresponding to 90 min after protein loading. (b) Graph showing the percent decrease in concentrations of the proteins from the base to the tip of the pillars.

4.2.4. Organoid-derived single cells can grow on 3D villus-like PEGDA-AA hydrogels and form a monolayer

After characterizing the gradients of ISC niche factors formed on villus-like PEGDA-AA hydrogels by LSFM and *in silico* modelling, we assessed whether we could grow organoid-derived epithelium monolayers on the hydrogels bearing the biochemical gradients. For that, the villus-like PEGDA-AA hydrogels were fabricated on PET membranes, mounted on Transwell inserts and functionalized with collagen type I (as detailed in the respective sections of Materials & Methods). Then, the proteins were delivered in the Transwell insert asymmetrically, i.e., from the basolateral side, to create the spatial gradients. For this first step, we employed as source medium primary fibroblasts_CM/ENRCV (see table 3.1 for a detailed composition) and we corrected the concentrations of the ISC niche factors for the protein accumulation taking place in the membrane as predicted by the *in silico* simulations. 24 hours after the formation of the gradients, we seeded organoid derived single cells from mouse isolated intestinal crypts. Using an initial cell seeding density of approximately $5x10^5$ cells/sample (carefully adjusted for each experiment), we observed that three days after seeding, epithelial monolayers had formed and were fully covering the surface of the hydrogels. Next, we wondered if the process to form a monolayer was dependent on the presence of ISC niche biomolecular gradients. For this, we seeded organoid-derived single cells on top of scaffolds bearing gradients and on scaffolds with no gradients, in other words, with uniform concentration of the

factors. Every 24 hours we renewed the media of both apical and basolateral compartments to maintain the gradients stable, as predicted by the *in silico* simulations. One day after cell seeding, cells were starting to form a monolayer, covering approximately 30% of the surface under both conditions (Figure 4.2.4). 48 hours after seeding, the monolayer coverage reached to 70% of the surface in the *Asymmetric* condition while in *Uniform* condition, the surface was almost fully covered (Figure 4.2.4). At 72 hours, the samples reached nearly 100% surface coverage in both conditions (Figure 4.2.4).

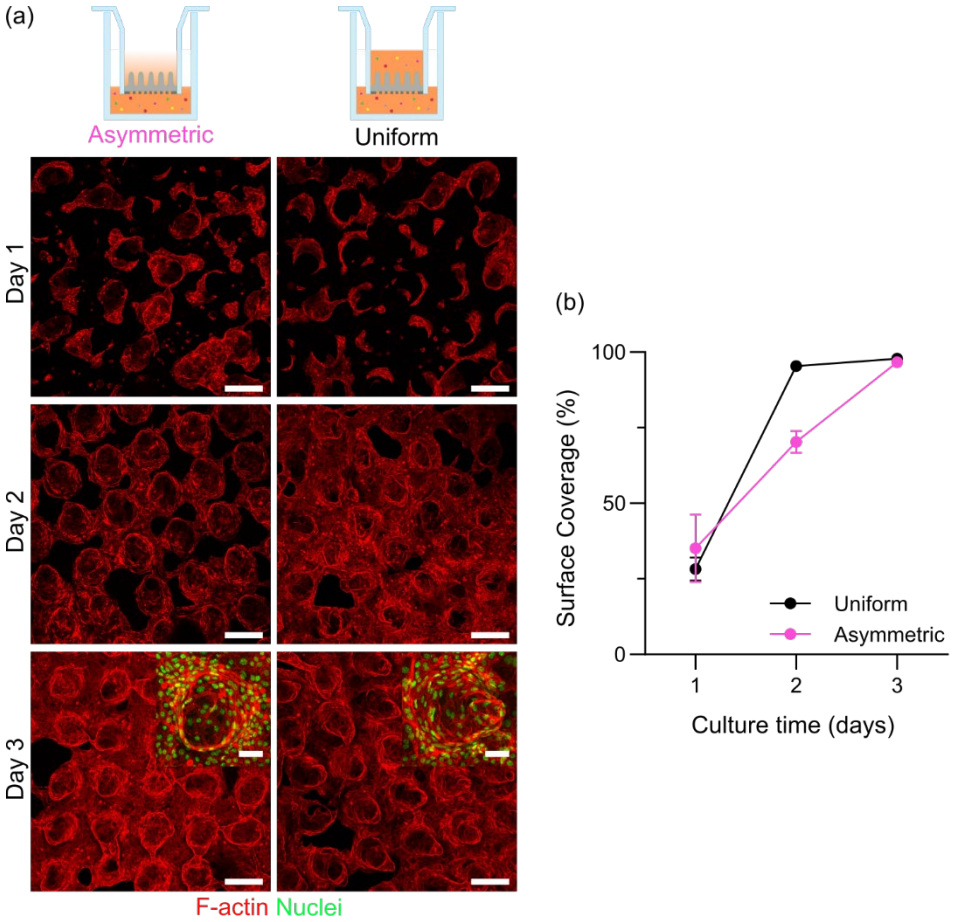

Figure 4.2.4. (a) Schematic drawings of *Uniform* and *Asymmetric* conditions. Representative confocal maximum intensity projection images of samples at day 1, 2 and 3 of culture immunostained for F-actin. Scale bars: 200 µm. Zoom-in insets at day 3 immunostained for F-actin and DAPI. Scale bars: 50 µm. (b) Graph plotting the percentage of surface covered by epithelial cells with respect to the total surface as a function of the cell culture time in the absence (*Uniform)* or presence (*Asymmetric*) of ISC biochemical gradients. Mean ± SD. n ≥ 2 samples. N ≥ 2 independent experiments.

These results suggested that organoid-derived cells were able to form complete monolayers on the surface of the hydrogels irrespective of the presence or

absence of such gradients. This implies that the type of ISC niche factor gradients formed in our system were not necessary for epithelial cells to be able to form complete epithelial monolayers; provided that the minimum concentration of factors required for cell growth were supplied. Still, it remained to be deciphered whether gradients of ISC factors determine cell compartmentalization *in vitro*.

4.2.5. The gradients' profile and composition affect the cellular behaviour

To elucidate if gradients of ISC factors guide cell compartmentalization *in vitro*, we analysed both the distribution of cells within the crypt region *in vivo*, i.e., proliferative ($Ki67^+$), stem (GFP^+), and Paneth cells (Lyz^+), and the cells within the villus region, i. e. all differentiated ($CK20^+$) cells including enterocytes ($FABP1^+$) in the presence or absence of gradients of ISC niche factors when there was a complete epithelium (i.e. at day 3). First, we analysed the compartmentalization of proliferative $Ki67^+$ cells along the villus axis (Figure 4.2.5 (a), (c)). We observed that under *Asymmetric* condition, almost 50% of proliferative cells were located at the base of the pillars, while only 11% were at the tip of the pillars (Figure 4.2.5 (c)) (the remaining cells were located in the intermediate region between the base and the tip). Instead, in the absence of gradients, less than 30% of the $Ki67^+$ cells were located at the base, and above 15% were located at the tip and the difference was not statistically significant (Figure 4.2.5 (c)). These results clearly evidenced that the frequency of proliferative cells positioned at the base was significantly higher in the presence of gradients. The quantification of the GFP signal along the villus axis revealed that GFP^+ stem cells were also preferentially located at the base in the *Asymmetric* condition, while they were rather uniformly distributed among the whole axis of the pillar in the *Uniform* condition at day 3 (Figure 4.2.5 (b) (d)). Moreover, 68.2 ± 5.0 % and 93.7 ± 2.0 % of $Ki67^+$ cells were also GFP^+ for *Asymmetric* and *Uniform* conditions, respectively (Figure 4.2.5 (e)). This result suggested that in the *Uniform* condition, almost all proliferative cells are stem cells, implying that the transit-amplifying population is almost absent, and that there are almost no quiescent cells within the stem cell pool. Conversely, in *Asymmetric* condition, there is a fraction of proliferative cells that corresponds to cells that are not stem cells, possibly transit-amplifying cells. Therefore, the *Asymmetric* condition seems to be favouring a more homeostatic like tissue. Next, we analysed the distribution of Paneth cells $(Lyz)^+$ and found that they were also preferentially located at the base for both conditions (Figure 4.2.5 (f), (g)) and they were localized next to GFP^+ stem cells (Figure 4.2.5 (f)), in line with the *in vivo* disposition.

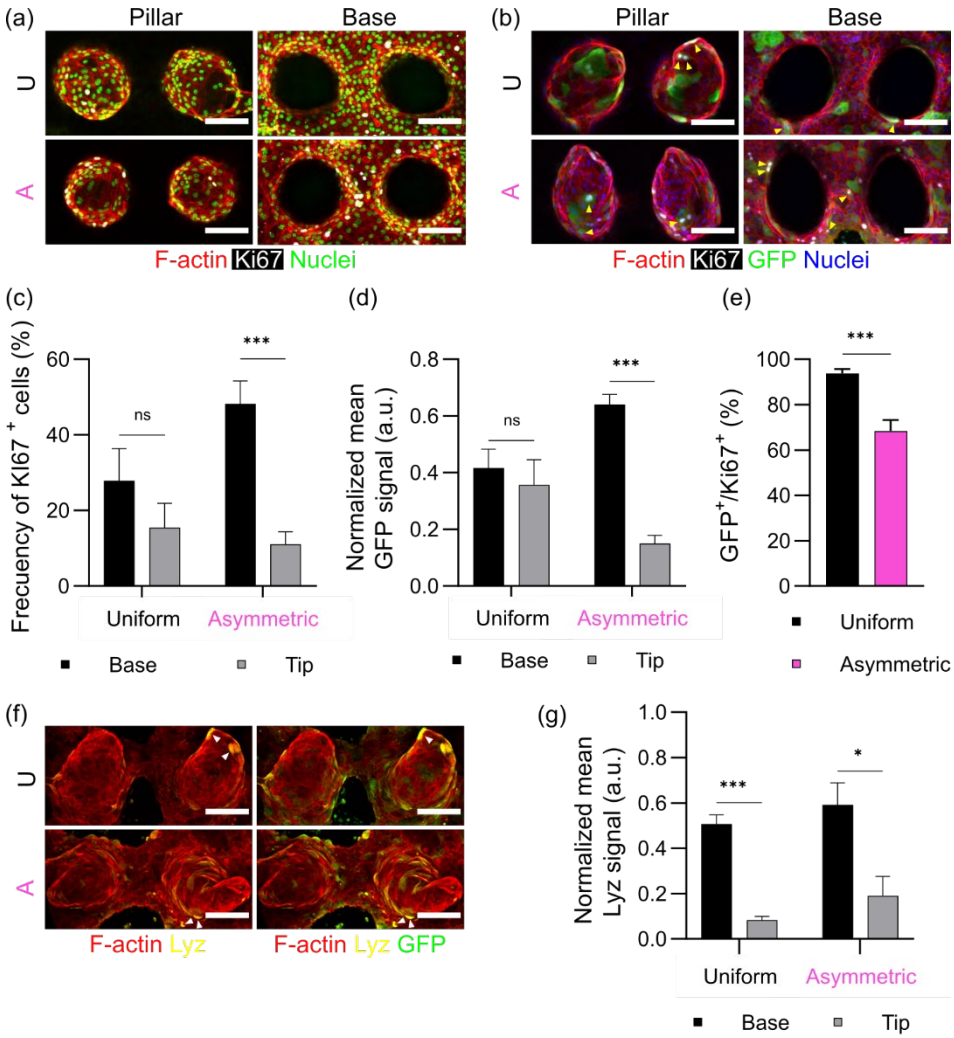

Figure 4.2.5. (a) (b) Maximum intensity projections of the sections corresponding to the pillar and to the base for *Uniform* (U) and *Asymmetric* (A) conditions. (f) Maximum intensity projections for *Uniform* (U) and *Asymmetric* (A) conditions. (a) Samples immunostained for F-actin, Ki67 (proliferative cells) and DAPI (nuclei). (b) Samples immunostained for F-actin, Ki67, GFP (stem cells) and DAPI. (c) Frequency of Ki67⁺ cells at the base and the tip of the pillars with respect to the total Ki67⁺ cells under ISC-niche biomolecules gradients (*Asymmetric*) or no gradients (*Uniform*). n ≥ 19 pillars, N ≥ 2 independent experiments. (d) Normalized mean GFP signal at the base and the tip of the pillars in *Asymmetric* or *Uniform* conditions. n ≥ 12 pillars, N ≥ 1 independent experiment. (e) Frequency of GFP⁺ cells within Ki67⁺ population. n ≥ 10 pillars, N ≥ 1 independent experiment. (f) Samples immunostained for F-actin, Lyz (Paneth cells) and GFP. Arrow heads point to Lyz⁺ cells. (g) Normalized mean Lyz signal along the rescaled villus axis and at the base and the tip of the pillars in *Asymmetric* or *Uniform* conditions. n ≥ 12 pillars, N ≥ 1 independent experiment. Scale bars: 100 µm. Data in all graphs are presented as Mean ± SEM. T-test, (*) $p < 0.05$, (***) $p < 0.001$.

Altogether, these findings suggest that the presence of gradients guides the formation of crypt-like compartments containing proliferative, stem and Paneth cells to localize at the base of the pillars.

Then, we wanted to evaluate how the disposition of the differentiated population in fully covered epithelial monolayers was impacted by the gradients of stem cell niche factors. For that, we analysed the mean intensity of CK20 (Figure 4.2.6 (a), (b))., a marker for differentiated cells with a graded expression, proportionate to the differentiation state[109]. In the absence of the gradients, the normalized mean intensity of CK20 was similar all along the pillars (Figure 4.2.6 (b)). In contrast, in the presence of gradients, there was a steep, statistically significant difference of such intensity, being lower at the base and higher at the tip of the pillars (Figure 4.2.6 (b)). Similarly, the amount of fatty acid binding protein 1 positive ($FABP1^+$) enterocytes concentrated at the tip of the pillars was significantly higher in the presence of gradients, as opposed to the *Uniform* condition (Figure 4.2.6 (c), (d)). Altogether, these findings suggest that the presence of gradients favours the *in vivo* physiological cell disposition.

After observing that the gradients of stem cell niche factors formed in our *in vitro* platform favour an *in vivo* disposition of cells in both crypt-like and villus-like regions, we made use of our system to modify the gradients applied and to read out the effect on the cellular response. For this purpose, we devised two new conditions: in the first one, we doubled the concentrations of Noggin and R-Spondin 1 (*Asymmetric 2.0*); and in the second one, we tested a chemically defined medium by plainly substituting primary fibroblasts_CM in *Asymmetric 2.0* for the recombinant protein Wnt2b, the most relevant proliferation-promoting molecule coming from the mesenchyme[8,110] (*Asymmetric Wnt2b*) (see table x for a detailed composition). The *in silico* model we developed predicted that doubling the concentration of R-spondin 1 and Noggin in the source would result in doubled concentrations for a given point along the villus axis, while the gradient slopes would stay unchanged (Figure 4.2.3 (b)). Cells receiving doubled amounts of these ISC niche factors can explain the increased expansion of the epithelial monolayers we observed at day 1 for *Asymmetric 2.0* and *Asymmetric Wnt2b* conditions, compared to *Asymmetric* condition (Figure 4.2.7 (a)). At day 3, epithelial cells occupied almost the entire scaffold surface for all the conditions (96.2 ± 0.9% for *Asymmetric*, 97.2 ± 1.1% for *Asymmetric 2.0* and 93.1 ± 3.6% for *Asymmetric Wnt2b*), therefore constituting a full epithelial monolayer (Figure 4.2.7 (a), (b)). The faster expansion of the epithelial monolayers under both *Asymmetric 2.0* and *Asymmetric Wnt2b* conditions can account for the increased amounts of proliferative cells found in these cultures (Figure 4.2.7 (a) (c)). At day 1, the percentage of $Ki67^+$ proliferative cells was

significantly higher in *Asymmetric Wnt2b* compared to the other two conditions (Figure 4.2.7 (c)). On the other hand, the frequency of Ki67⁺ cells was significantly reduced at day 3 for the same condition (Figure 4.2.7 (c)), suggesting that the type of Wnt2b gradient present in our system leads to an initial fast expansion and a later exhaustion of the proliferative domain, altering the growth rhythm of the epithelial monolayer. For *Asymmetric 2.0*, we observed a similar behaviour although less pronounced: at day 1, the percentage of Ki67⁺ cells was higher than in *Asymmetric*, and at day 3, it decreased significatively (Figure 4.2.7 (c)). Altogether, these findings demonstrate that different ISC niche biochemical gradients lead to changes in the proportion of different cell types and their distribution in our villus-like 3D intestinal epithelial model, proving it useful for the study of the effect of such gradients on the cellular response.

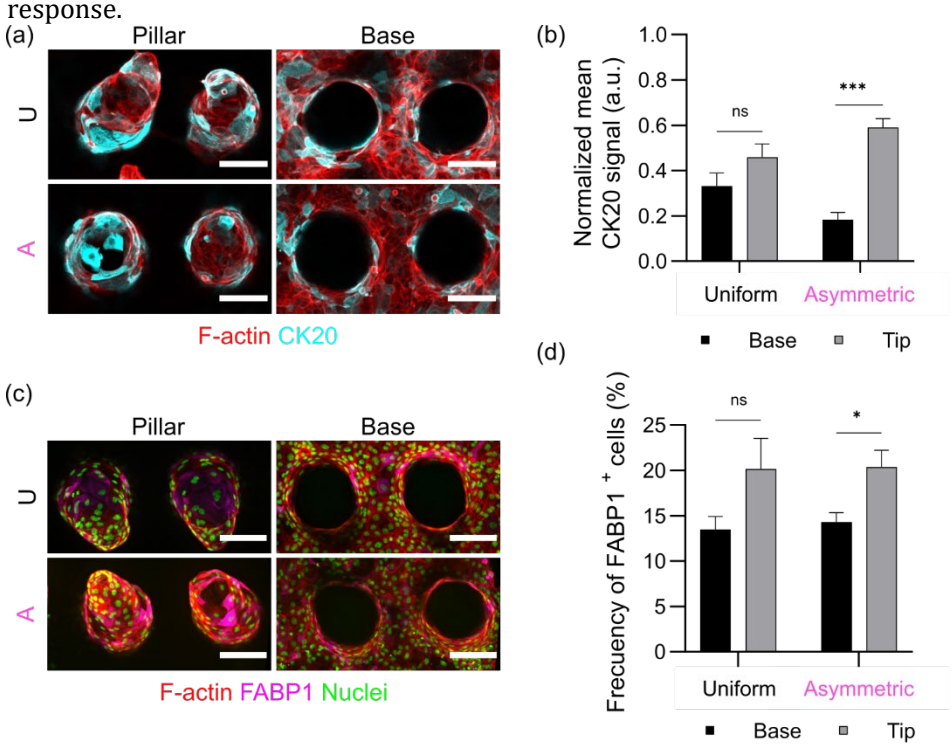

Figure 4.2.6. (a) (c) Maximum intensity projections of the sections corresponding to the pillar and to the base for *Uniform* and *Asymmetric* conditions. (a) Samples immunostained for F-actin and CK20 (differentiated cells). (b) Normalized mean CK20 signal at the base and the tip of the pillars in *Asymmetric* or *Uniform* conditions. n ≥ 19 pillars, N ≥ 2 independent experiments. (c) Samples immunostained for F-actin, FABP1 (enterocytes) and DAPI. (d) Frequency of FABP1⁺ cells at the base and the tip of the pillars with respect to the total FABP1⁺ cells under ISC-niche biomolecules gradients (*Asymmetric*) or no gradients (*Uniform*). n ≥ 11 pillars, N ≥ 1 independent experiment. Data in all graphs are presented as Mean ± SEM. T-test, (*) $p < 0.05$, (***) $p < 0.001$.

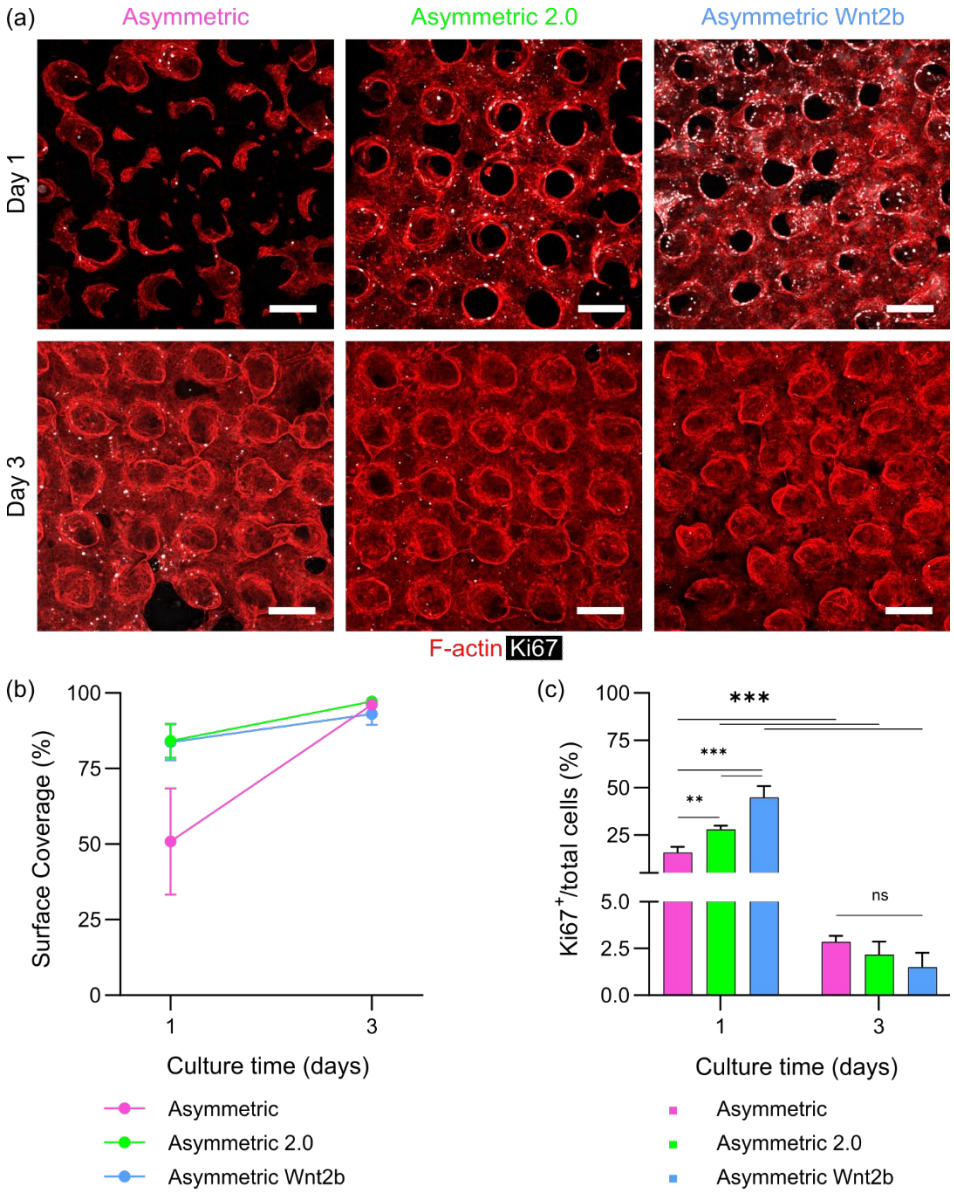

Figure 4.2.7. (a) Maximum intensity projections of *Asymmetric*, *Asymmetric 2.0* and *Asymmetric Wnt2b* conditions at days 1 and 3 of cell culture immunostained for F-actin and Ki67. Scale bars: 200 µm. (b) Percentage of surface covered by epithelial cells with respect to the total surface as a function of the cell culture time in *Asymmetric*, *Asymmetric 2.0* and *Asymmetric Wnt2b*. *Asymmetric*: Day 1 N = 4, n = 4, Day 3 N = 4, n = 5. *Asymmetric 2.0:* Day 1 N = 3, n = 3, Day 3 N = 2, n = 3. *Asymmetric Wnt2b:* Day 1 N = 2, n = 3, Day 3 N = 2, n = 4. (c) Percentage of $Ki67^{+}$ (proliferative) cells with respect to the total number of cells for each culture condition. *Asymmetric:* Day 1, N = 3, pillars = 19, Day 3, N = 4, pillars = 40. *Asymmetric 2.0:* Day 1, N = 2, pillars = 13, Day 3, N = 2, pillars = 15. *Asymmetric Wnt2b:* Day 1, N = 2, pillars = 10, Day 3, N = 2, pillars = 15. Data in all graphs are presented as Mean ± SEM. T-test, (**) $p < 0.005$, (***) $p < 0.001$.

Altogether, the experiments presented in this section demonstrate the successful fabrication of 3D villus-like PEGDA-AA hydrogels with anatomical dimensions, a native tissue-like elasticity and a mesh size that allows the diffusion of the factors of the ISC niche. We have also shown how these hydrogels can be successfully functionalized with collagen I, which in turn allows the culture of organoid-derived cells. Primary epithelial cells formed a complete monolayer regardless of the presence or absence of gradients. However, only under gradients of the ISC niche (*Asymmetric* condition), the 3D monolayer exhibited *in vivo*-like cell compartmentalization, as seen by proliferative and stem cells preferentially located at the bases of the hydrogel and the differentiated cells (mainly enterocytes) located at the uppermost regions of the villus-like pillars. Finally, by delivering different types of gradients and observing how they impacted on the dynamics of monolayer formation and the proliferative population within them, we proved our platform as an ideal tool to screen for different gradients profiles and compositions and read out how epithelial monolayers react.

4.3. Intestinal primary fibroblasts are indispensable for homeostatic-like epithelial migration

In the section presented above (section 4.2), we described the engineering of a 3D platform that allowed the culture of epithelial cells under gradients of ISC niche factors from epithelial and fibroblast source. As mentioned in the introduction, several studies have shown that the intestinal stem cell niche, and thus, the overall homeostasis of the intestinal epithelium, is not only sustained by the epithelium itself but also by the paracrine signalling coming from the subepithelial fibroblasts present in the lamina propria[28,29]. Specifically, factors promoting both differentiation (BMP agonists[32–34]) and proliferation (Wnt2b[8], R-spondins[28,30], BMP antagonists[31–33] and EGFR ligands[35]) have been reported to be implicated. Aside from all these factors involved in the maintenance of the stem cell niche, intestinal fibroblasts have also been shown to express and secrete chemokines, cytokines, growth factors, prostaglandins, and ECM proteins, thus playing a key role in intestinal development and disease[20]. However, few studies have gone beyond studying the effect of the fibroblasts paracrine signalling on the epithelium and, in our opinion, there's scarcity of studies evaluating the possible physical crosstalk between intestinal fibroblasts and epithelial cells in homeostatic and pathological conditions. In 2010, Seltana et al.[43] developed an epithelial-mesenchymal coculture system consisting in a layer of human intestinal myofibroblasts (HIM) and a layer of Caco-2 cells on top. By manually scratching using a pipette tip, they managed to create a wound in the epithelial layer and study the migration of epithelial cells. They found that wound repair was more efficient in the cocultures of Caco-2/HIM than in monocultures of Caco-2, although they did not go further in investigating the mechanism. Moreover, even though the study allowed to unveil a role of fibroblasts in epithelial migration under pathological conditions, whether fibroblasts exert the same functions in physiological conditions was not addressed. Moreover, they used the tumour-derived cell line (Caco-2) as the epithelial source.

In this section, we aimed to develop a simple yet physiologically relevant *in vitro* model to study if, given their close proximity to the epithelial monolayer, fibroblasts play a role in the migration of epithelial cells under physiologic conditions (rather than pathologic such as upon wounding) by either paracrine signalling and or direct physical contact..

4.3.1. scRNAseq reveals the population of isolated primary stromal cells from the intestinal mucosa to consist mainly of fibroblasts-like cells

To study the possible effect of fibroblasts on the migration of epithelial cells, we opted for isolating primary fibroblasts from mouse intestinal mucosa (Figure 3.1 (c)) as they better represent the tissue physiology compared to available cell lines. Since the reported cell populations within the intestinal mucosa are multiple and varied, we decided to characterize the cell populations obtained from our isolations and after their culture through scRNAseq.

First, we found a population of cells accounting for 1% of the total population expressing Pecam1, which we identified as endothelial cells (Figure 4.3.1, top left panel). The second smallest population (2%) was expressing Gap43 (Figure 4.3.1, top right panel), Ngfr and S100b (data not shown), typical markers of neurons and glial cells. Cd52 was expressed by 10% of the cells (Figure 4.3.1, bottom left panel), thus suggesting their identity as immune cells. Next, we identified a large fraction of cells (75%) expressing none of the markers above and the intermediate filament Vimentin (Figure 4.3.1, bottom right panel), thus considering this cell cluster a suitable candidate to be the fibroblastic population of the intestinal lamina propria compartment. Last but not least, there were 12% cells that could not be faithfully classified into any group.

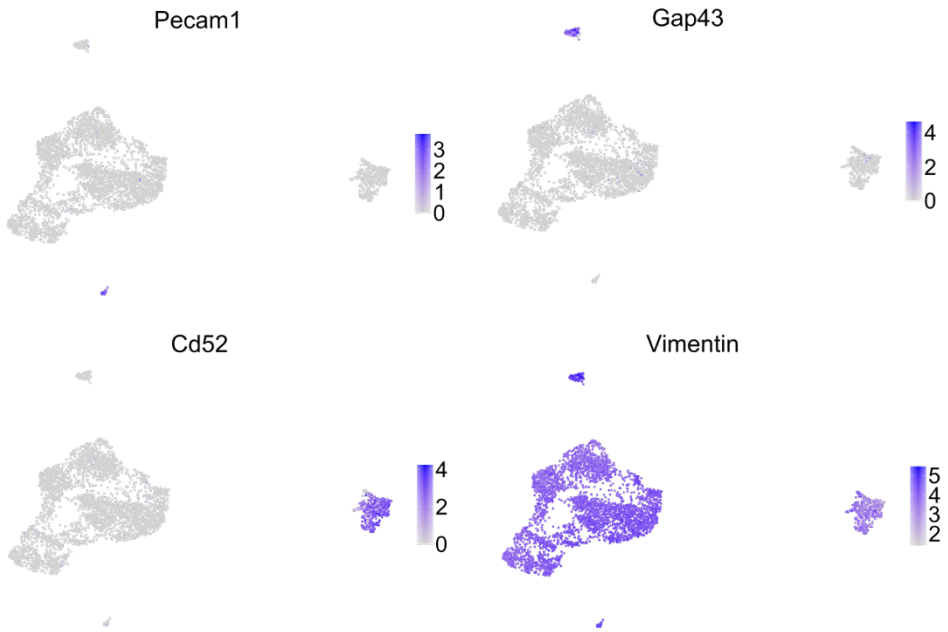

Figure 4.3.1. Projection of Vim, Pecam1, Gap43 and Cd52 single-cell transcript density onto the Uniform manifold approximation and projection (UMAP) plot. Expression scales are different for each marker.

All in all, scRNAseq analysis confirmed that the vast majority of cells obtained through our isolation protocol were a suitable candidate to be identified as fibroblasts, but there was also the presence of other cell types relevant for tissue function: endothelial cells, neurons and glial cells and immune cells, perfectly coinciding with previous characterization of intestinal lamina propria cellular populations[111,112].

4.3.2. The fibroblastic population contains *in vivo*-like subcellular types: telocytes, pericytes and PDGFRA^{low} cells

Within the fibroblastic population, distinct cell types have been reported to exist according to their morphology, the markers they express, the factors they secrete and their localization within the crypt-villus axis[33]. Therefore, we decided to further evaluate the sub-population that we identified as fibroblasts to see if we could identify the same cell populations as those reported *in vivo*. For that, we focused on the expression of proliferation and differentiation promoting factors involved in the Wnt and BMP signalling (Figure 4.3.2). First, we identified a group of cells (30% of the total stromal population) that displayed a high expression of Wnt4 and Wnt5a - two non-canonical Wnt agonists -, the Wnt inhibitors Dkk3 and Sfrp1, and Bmp4 and Bmp5, two Bmp agonists, which is compatible with telocytes (Figure 4.3.2 (first row)). Next, we found a cluster expressing Wnt2b, the canonical Wnt agonist secreted by non-epithelial cells, together with Rspo3 and Chrd (BMP antagonist), which is compatible with PDGFRA^{low} cells (PDGFRA^{low} 2) (Figure 4.3.2, (fifth row)). Another population was found to express Grem1 and Grem2 (BMP antagonists), Bmp1 and Dkk2 (Wnt antagonist), classified also as PDGFRA^{low} cells (PDGFRA^{low} 1) (Figure 4.3.2 (fourth row)) and accounting for the 22.3% of the total population together with the previous one.

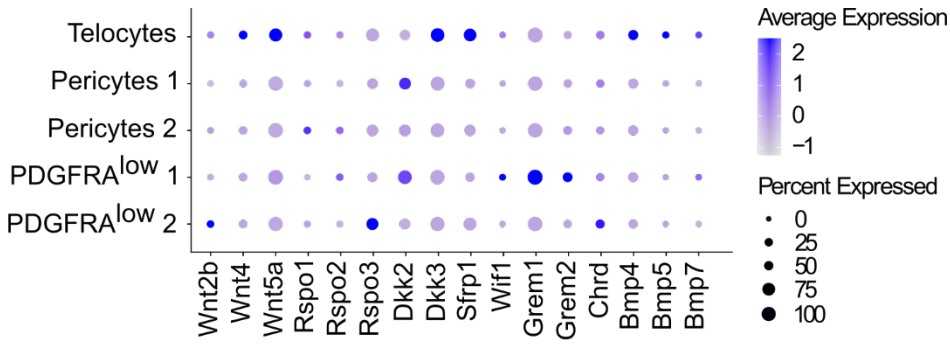

Figure 4.3.2. Relative expression of known stromal cell markers in cell clusters identified by scRNA-seq. Circle sizes represent the within-cluster probability of gene detection and fill colours represent normalized mean expression levels.

Finally, we spotted two populations (together summed up to 22.5%) that had almost no expression of any of the relevant factors of the ISC niche (Figure 4.3.2 (second and third rows)), so they could be classified as pericytes, according to the literature[33].

Overall, the data presented here suggests that our protocol to isolate intestinal stromal cells and, most importantly, after the passaging and culturing of these primary cells, we could successfully identify the presence of all the fibroblastic populations reported to be located right underneath the epithelium[33]: telocytes (30%), pericytes (22.5%) and PDGFRA^{low} cells (22.3%), as seen by the expression of similar markers, together with neurons, endothelial cells/lymphocytes and immune cells (Figure 4.3.1). As reported in the literature, we have also found that, even within a specific cell population, there is expression of counteracting molecules (for instance, within telocytes, there is simultaneous expression of Dkk3 and BMP4), hindering the categorization of specific cell types into proliferation-promotive ones and differentiation-promoting ones. Since there is this signalling overlap between cell types, as well as redundancy among agonists and antagonists, it still remains a challenge to attribute specific functions to individual cell clusters[33]. Therefore, to faithfully represent all the cellular components of the intestinal stroma and to evaluate their effect on the epithelium, we conducted the following experiments using the whole population of isolated stroma, containing mainly fibroblasts.

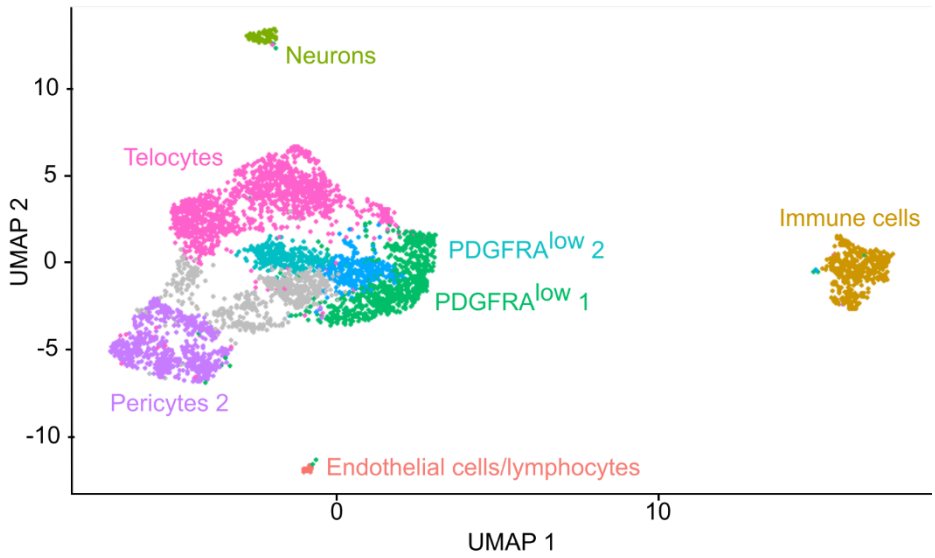

Figure 4.3.3. UMAP of established primary culture from small intestine stroma. Resident populations were dominated by molecularly distinct clusters of telocytes, pericytes and PDGFRA^{low} cells. Grey dots represent cells that could not be integrated within a cluster.

4.3.3. The fibroblasts' paracrine signalling transforms organoids into cysts and fibroblast-organoids physical interaction leads to epithelial spreading

To study the interplay between fibroblasts and organoid-derived epithelial cells in the migration of the latter, we first used what we considered the most straightforward approach, that is to say, co-culturing organoids and primary fibroblasts in 3D Matrigel drops. We compared crypts cultured with ENRCV medium (*control*), with primary fibroblasts_CM/ENRCV medium *(+ fibroblasts conditioned medium condition* or *+ fibr. cond. med.)* and crypts cultured with primary fibroblasts *(+ fibroblasts*). By comparing the last two conditions we aimed to disentangle the paracrine signalling from physical cue effects.

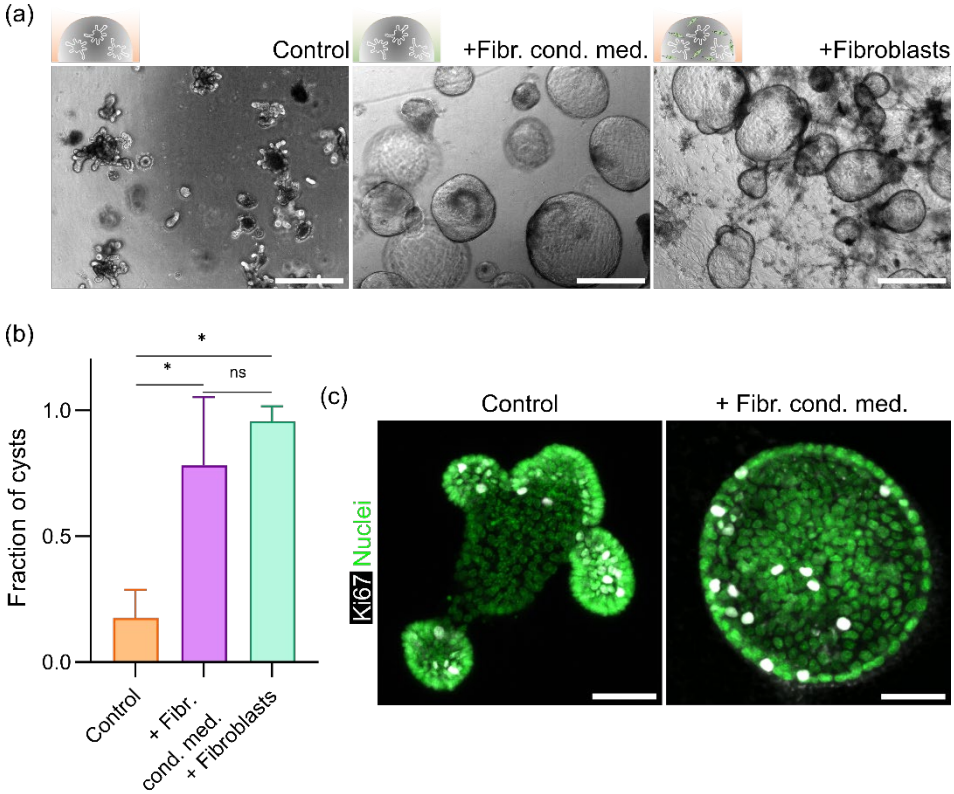

Figure 4.3.4. (a) Representative bright field images of crypts grown in 3D-Matrigel drops with ENRCV medium (*control*), with primary fibroblasts_CM/ENRCV medium (*+ fibr. cond. med.)* and in coculture with primary fibroblasts *(+ fibroblasts*) after 2 days in culture. Scale bar: 1000 µm. (b) Fraction of cysts respect to all organoids per condition. N ≥ 4 independent experiments. Kruskal-Wallis test. (*) $p < 0.05$. (c) Representative confocal images of crypts grown in 3D-Matrigel drops in *control* and in *+ fibr. cond. med.* Scale bars: 50 µm.

After 2 days in culture, we observed that when crypts were cultured in *+ fibr. cond med.* or in *+ fibroblasts* conditions, they were forming cystic structures without budding units, suggesting that the paracrine signalling from the

primary fibroblasts was sufficient to induce this change of phenotype (Figure 4.3.4, (a), (b)). Because this phenotype has been previously linked to an increase in proliferation[8,28,30,113], we immunostained crypts grown in the three different conditions against Ki67. Surprisingly, we did not observe any visual increase in the amount of cells positive for Ki67 in the *+ fibr. cond. med.* condition vs the *control* condition (Figure 4.3.4 (c)). Instead, we found that, while in the *control* condition they were localised in clusters within the crypt-like regions, in the *+ fibr. cond. med.* they were found randomly scattered throughout the cysts. Indeed, a very recent study reported this same cystic morphology of crypts upon the culture with BMP agonists[112]. In our scRNAseq analysis, we could clearly observe that the isolated primary fibroblasts expressed both, factors involved in proliferation, such as Wnt2b and Rspo3, together with factors promoting differentiation, such as Bmp4. Assuming that these proteins are secreted into the media and thus, the conditioned medium used to culture the organoids contains these factors, we conclude that this morphological transition into cysts cannot be solely linked to an increase in cell proliferation.

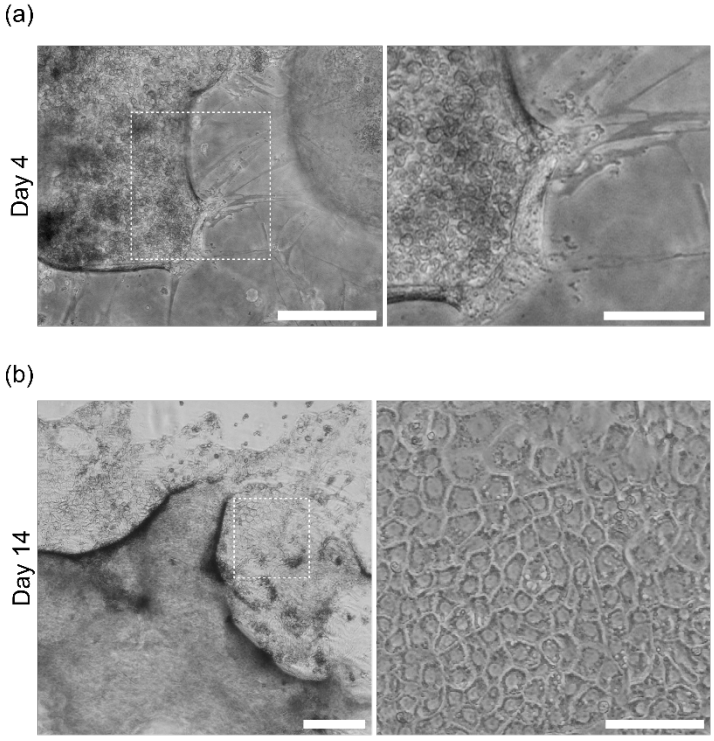

Figure 4.3.5. Representative bright field microscopy images of *+ fibroblasts* condition after (a) 4 days in culture. Scale bar: 500 µm. Zoom-in scale bar: 200 µm. (b) 14 days in culture. Scale bar: 250 µm. Zoom-in scale bar: 50 µm.

Even though we could observe this cystic behaviour in both *+ fibr. cond. med.* and *+ fibroblasts* conditions, the morphology of the cysts was clearly distinct.

While *+ fibr. cond. med.* cysts were fairly spherical (Figure 4.3.4, (a, middle panel)), cysts in the physical presence of fibroblasts adopted deformed spherical shapes, characterized by large bulging regions (Figure 4.3.4, (a, right panel)). Moreover, at day 4 of coculture those bulging regions were already contacting the surface (Figure 4.3.5 (a)). A closer look unveiled fibroblasts physically interacting with the cysts in a perpendicular fashion and visibly deforming them, seemingly pulling the epithelial cells with them and triggering their expansion over the surface. Indeed, at day 14 of coculture, the cysts dragged by the fibroblasts had transformed into flat monolayers (Figure 4.3.5 (b)).

All in all, intestinal primary fibroblasts' secreted factors were found to induce the morphological change of organoids into cysts. The coculture of organoids with fibroblasts, not only induced this 3D reorganization but they caused them to transition from 3D cysts into 2D monolayers, a process that involved epithelial migration triggered by the physical contact with the fibroblasts.

4.3.4. Primary fibroblasts enhance intestinal epithelial migration *in vitro*

Historically, passive mitotic pressure generated by cell division in the intestinal crypts has been regarded as the main driving force for cell migration on villi[3,114]. However, treating mice with irradiation and mitotic inhibition, in spite of causing significant cell death within crypts, did not impair epithelial migration[4,5]. Moreover, a group of scientists has recently found that indeed, mitotic pressure acts solely in the crypts and lower regions of the villi. Instead, they found that along the villi, enterocytes have front-back actin-rich protrusions pointing in the direction of cell movement that are dependent on Arp2/3 complex, thus claiming that along the villi there is active migration[6]. At the same time, we have reported above a seemingly role of fibroblasts in the expansion of organoid-derived epithelial cells in a 3D context. To shed light in how cell migration in the intestinal epithelium occurs, we decided to evaluate, on one side, which is the role of fibroblasts, and on the other side, which is the role of cell proliferation on this process. To do so, we adapted our protocol to create self-organizing monolayers of organoid-derived cells on Matrigel coated glass [60,89] to setup a coculture system with primary mouse fibroblasts, and we devised customized PDMS barriers to generate cell-free gaps to be able to analyse epithelial migration (section 3.3.3). To study the putative role of fibroblasts in epithelial migration, we set up three different experimental conditions: epithelial cells only (*control*), epithelial cells cultured with primary fibroblasts_CM (*+ fibr. cond. med.*) and epithelial cells cultured with primary fibroblasts underneath (*+ fibroblasts*). Then, we acquired time-lapse videos of the three conditions, and we tracked the epithelial cells over time.

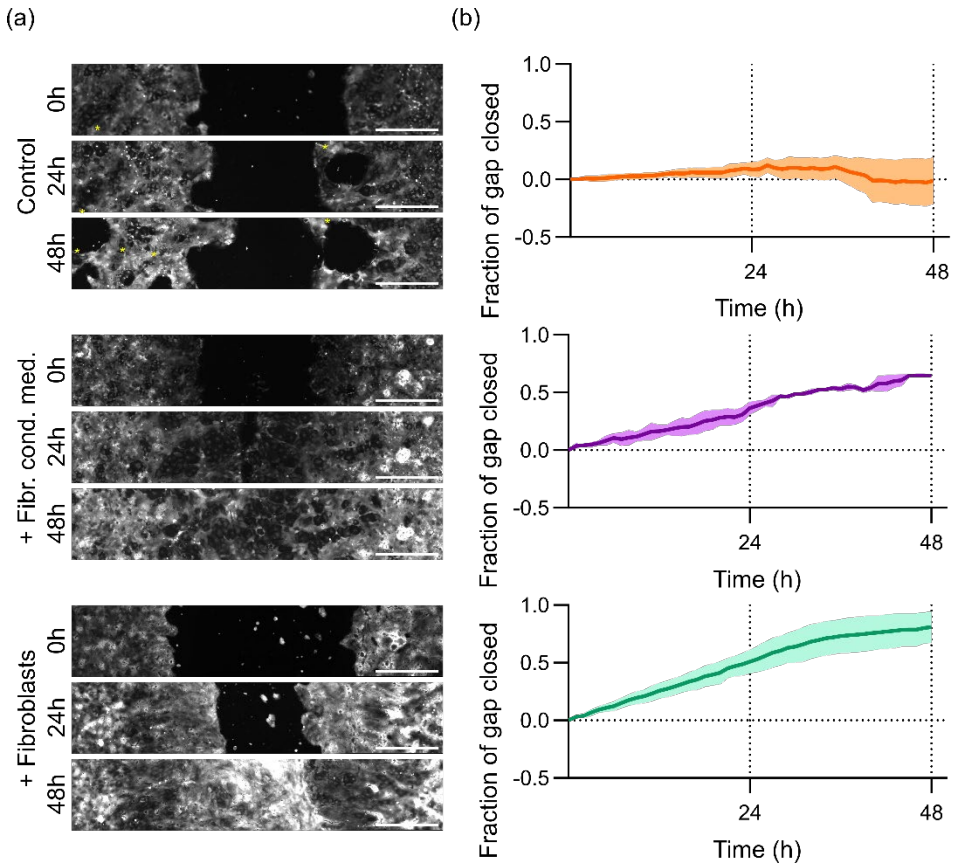

Figure 4.3.6. (a) Snapshots of the live-imaging of tdTomato organoid-derived cells migrating in control, *+ fibr. cond. med.* and *+ fibroblasts* conditions at 0, 24 and 48h upon barrier removal. Asterisks highlight holes in the monolayers. Scale bars: 500 µm. (b) Fraction of gap closed along time in control, *+ fibr. cond. med.* and *+ fibroblasts* conditions. Mean ± SEM. N ≥ 2 independent experiments.

At t=0h, right after barrier removal, all conditions had confluent epithelial monolayers. However, at t=24h and specially, at t=48h, we found striking differences (Figure 4.3.6). Both in *+ fibr. cond. med.* and *+ fibroblasts* conditions, the migration front advanced, but only in the *+ fibroblasts* condition the gap could be fully closed. Conversely, in *control* condition, despite the appearance of some collective finger-like structures protruding from the monolayer, it advanced much less, impeding the closure of the gap. A closer look unmasked the appearance of large holes in the monolayer of the *control* condition (Figure

4.3.7, top panel), suggesting that the epithelium was not able to maintain its integrity and cohesiveness during the gap closure process.

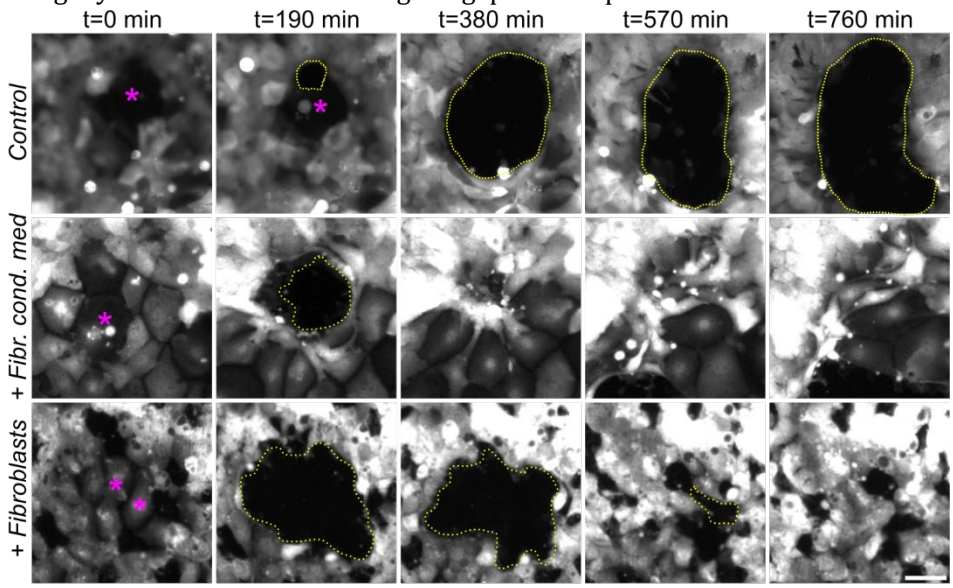

Figure 4.3.7. Snapshots of the live-imaging of organoid-derived cells (fluorescence signal comes from tdTomato⁺ ones) migrating in *control*, *+ fibr. cond. med.* and *+ fibroblasts* conditions. t=0 min corresponds to right before hole emergence. Holes areas are delineated with a dotted yellow line. Larger cells next to holes are highlighted with a magenta asterisk. Scale bar: 50 μm.

Next, we tracked the origin of these holes by back-tracing how they formed. We observed that holes generally emerged next to cells with a large area, usually indicative of differentiated cells[88] (Figure 4.3.7 (top panel)). Typically, the process started by the breaking of the cell-cell contact between this large cell and one of its neighbours, leading to the retraction of the large cell and its subsequent detachment from its neighbours. Then, cells at the edge of this newly formed gap started migrating inwards in an attempt to close it and restore tissue integrity. However, this process typically failed, and the hole actually expanded. It is worth noting that this process was not necessarily associated with cell death or delamination. Interestingly, in the *+ fibr. cond. med.* and *+ fibroblasts* conditions, we could also spot the emergence of holes associated with large cells and following a similar pattern (Figure 4.3.7 (middle and bottom panel)). However, in these two conditions, after the initial retraction, cells at the edge of the hole started migrating inwards and successfully closed the gap, thus quickly restoring the monolayer integrity. These results seem to indicate that the paracrine signalling from the fibroblasts, present both in *+ fibr. cond. med.* and *+ fibroblasts* conditions, is sufficient to enable epithelial cells to successfully close the gap.

4.3.5. Epithelial migration is independent of cell proliferation

To elucidate if cell proliferation had a substantial role in the migration of epithelial cells in our experiments, we immunostained samples with Ki67 and we quantified the percentage of positive cells in the migration front region and in a far-away region where the monolayer was intact (Figure 4.3.8). For all three conditions, we observed that within the monolayer, proliferative cells localized in clusters, typically linked to crypt-like regions (Figure 4.3.8 (left)). Moreover, the percentage of proliferative cells was similar between *control*, *+ fibr. cond. med*. and *+ fibroblasts* conditions (around 5%) (Figure 4.3.8 (b)).

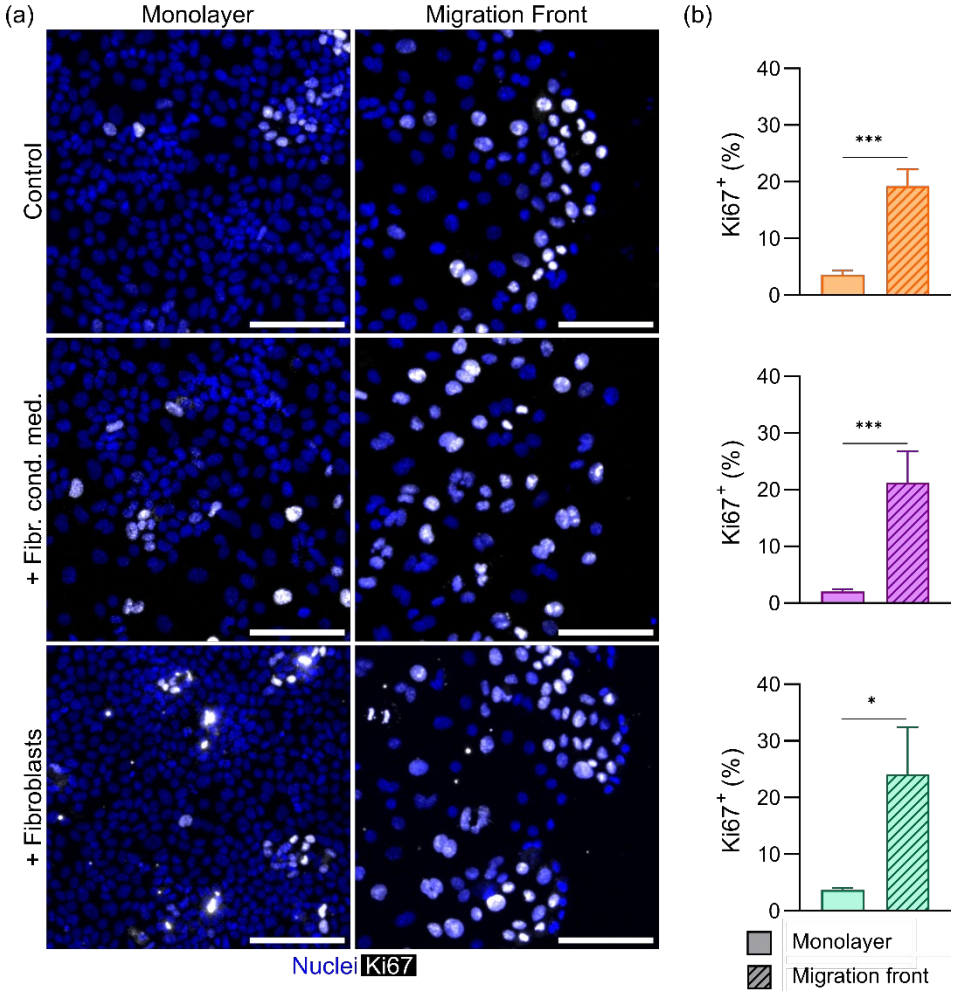

Figure 4.3.8. (a) Sum intensity projections in the monolayer region and in the migration front region at 24h upon barrier removal immunostained for DAPI (nuclei) and Ki67 (proliferative cells) of *control*, *+ fibr. cond. med.* and *+ Fibroblasts* conditions. Scale bars: 100 μm. (b). Percentage of $Ki67^+$ cells in the monolayer and in the migration front region of *control*, *+ fibr. cond. med.* and *+ fibroblasts* conditions. Mean ± SEM. Mann-Whitney test. (*) $p<0.05$, (***) $p<0.001$. $N \geq 2$ independent experiments.

Next, we observed that in the migration front, there was a statistically significantly higher percentage of Ki67$^+$ proliferative cells (more than 20%) than inside the monolayer for all conditions. With this result, we found reasonable to discard the hypothesis that cells migrate because of mitotic pressure can be discarded (if proliferative cells are at the front, they cannot exert any pressure on the rest of the cells). Instead, in agreement with other previous observations[6,7], we claim that, at least in the system developed here, the migration of epithelial cells is not a passive phenomenon, but an active one. Intriguingly, Ki67$^+$ cells were arranged very differently than within the monolayer: proliferative clusters were less well-defined and with proliferative cells less packed. Interestingly, we observed the same ratio of cell proliferation in the *control* condition than in both *+ fibr. cond. med.* and *+ fibroblasts* conditions, suggesting than the differences observed in epithelial migration between conditions cannot be attributed to differences in the rate of cell division.

4.3.6. Primary fibroblasts align in the direction of the gap, migrate towards the gap, and induce directional epithelial migration

Having concluded that differences in gap closure between the different conditions cannot be attributed to changes in cell proliferation, we analysed individual cell trajectories to better understand the epithelial cell migration. We observed that epithelial cell trajectories in the *control* condition were rather random, there was no preferred direction (Figure 4.3.9, (a)), whereas in *+ fibr. cond. med* and in *+ fibroblasts* conditions, most of the trajectories were oriented towards the gap (Figure 4.3.9 (b), (c)), and epithelial integrity was maintained during migration (Figure 4.3.6 (a, middle and bottom panels)). Still, cell trajectories in the *+ fibroblasts* condition (Figure 4.3.9 (c) were significantly more directed towards the gap than in the *+ fibr. cond. med.* condition (Figure 4.3.9, (b)), as seen by the quantification of the directionality index (Figure 4.3.9, (d).

We thus hypothesize that fibroblasts, as we observed in the 3D co-culture experiments with organoids (Figures 4.3.4 and 4.3.5), might be playing a physical role in guiding epithelial migration in gap closure experiments. To explore this scenario, we decided to further evaluate the *+ fibroblasts* condition at the initial stage of gap closure (first 9 hours upon barrier removal), focusing on the behaviour of fibroblasts during the migration of epithelial cells. To do so, we used particle image velocimetry (PIV) to obtain velocity fields from phase contrast time-lapse movies at the migration front, thus comprising both epithelial cells and fibroblasts.

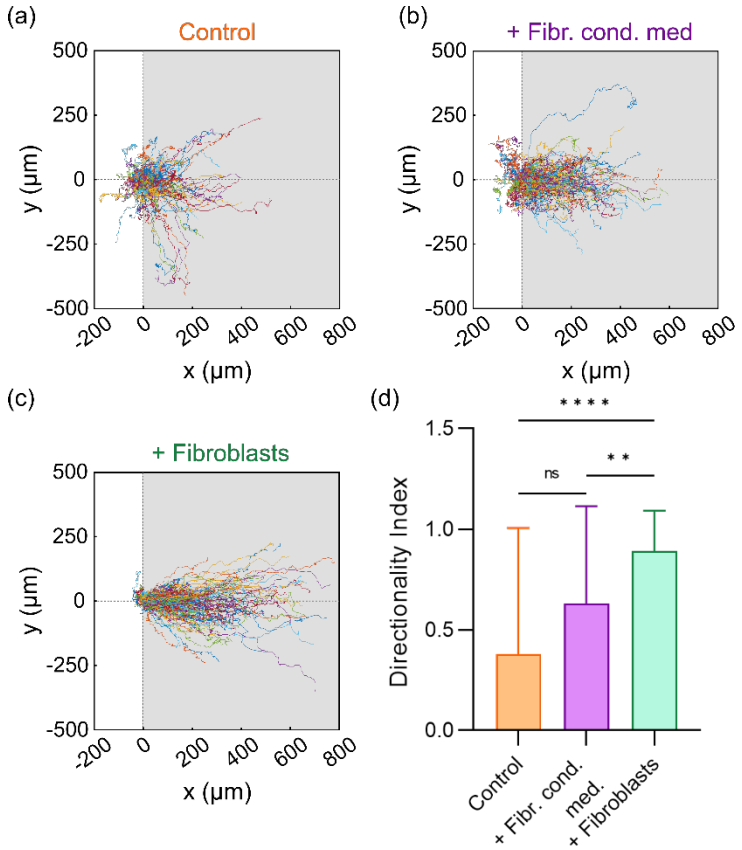

Figure 4.3.9. Trajectories of each individual cell centred at the origin at t = 0h for *control* (a), *+ fibr. cond. med.* (b) and *+ fibroblasts* (c) conditions. White area represents the monolayer whereas grey area represents the gap. (d) Directionality index of epithelial cells within the first 250 µm from the migration front. 0 corresponds to completely parallel to the migration front. 1 corresponds to completely perpendicular and towards the migration front. Mean ± SEM. Kruskal-Wallis. (*) $p<0.05$, (***) $p<0.00$. $N \geq 4$ independent experiments.

Two clearly differentiated regions appeared on the maps of the x-component of the mean velocities (V_x), invisible on the maps of the y-component (Figure 4.3.10 (a), (b)). Specifically, the region at the left of the migration front (corresponding to epithelial cells) exhibited $V_x > 0$ on average, indicating migration toward the gap. In contrast, the region at the right of the migration front (corresponding to fibroblasts) exhibited $V_x < 0$ on average, thus evidencing migration towards the monolayer. This observation implied not only migration of epithelial cells but also of fibroblasts. Therefore, these results suggest that there might be an active cooperation in migration between the fibroblasts and the epithelial cells. Whether this cooperation is necessary for an efficient migration or not needs to be properly addressed.

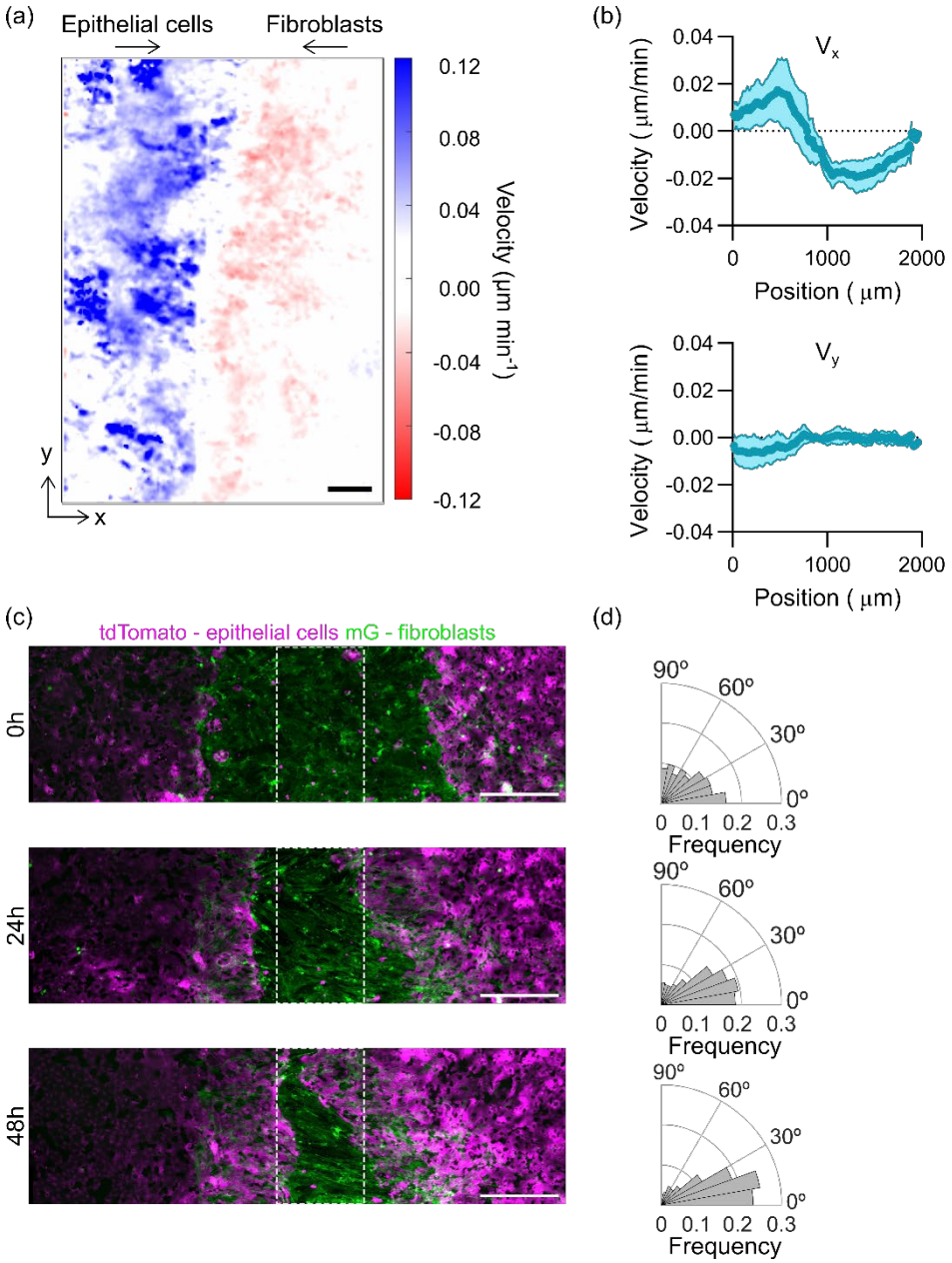

Figure 4.3.10. (a) Average velocity fields in the x axis of the first 9 hours of gap closure obtained through PIV analysis. Scale bar: 250 µm. (b) Profiles of the x-component (V_x) and y-component (V_y) of the mean velocity across the gap direction during the first 9 hours of gap closure. Mean ± SD. n = 4 migration fronts of N = 2 independent experiments. (c) Sum intensity projections of timeframes corresponding to 0, 24 and 48h upon barrier removal of the *+ fibroblasts* condition. Scale bars: 500 µm. (d) Polar histograms of the fibroblasts orientation. 0º corresponds to parallel alignment to the migration direction and 90º, perpendicular. Mean. N = 5 independent experiments.

Given the observation that not only epithelial cells but also fibroblasts migrate, we wanted to analyse how they were oriented while doing so. For that, we inspected the disposition of fibroblasts with respect to the migration front using Orientation J, a software package implemented in FiJi that characterizes the orientation and isotropy properties of ROIs. We observed that over time, fibroblasts became preferentially oriented close to 0º, that is to say, aligned perpendicularly to the migration front (Figure 4.3.10, (c), (d)). Noteworthy, not only those fibroblasts in contact with the epithelium became aligned but also those in the central region of the gap (as far as 750 μm from the migration front), clearly suggesting a fibroblast-fibroblast communication added to the epithelium-fibroblast crosstalk previously seen (Figure 4.3.10 (a)). In sum, we have observed that fibroblasts, while migrating towards the epithelial monolayers, align perpendicularly to the migration front, even those far from it, and allow epithelial cells to migrate in a more directed manner towards the gap, thus suggesting an active and physical role of fibroblasts in leading the migration of epithelial cells.

4.3.7. Primary fibroblasts at the gap secrete aligned ECM fibres that aid epithelia directionality

Fibroblasts are the primary mediators of ECM deposition and maintenance. In the context of tumour invasion, aligned ECM fibres have been shown to generate tracks for the invasion of tumour cells [115,116]. Indeed, a recent study has put the two concepts together, i.e., they correlated fibroblasts' alignment with how the ECM is organized. Therefore, we wondered whether, in our setup, fibroblasts were secreting aligned ECM proteins that were in turn, being used by epithelial cells to migrate. To answer this question, we immunostained *+ fibroblasts* samples at 24 h upon barrier removal against relevant ECM proteins (fibronectin, laminin and collagen IV) (Figure 4.3.11). First, we observed that the three proteins were being expressed in the cocultures and also in the epithelium-free region, suggesting they were secreted by fibroblasts. Then, we observed that they exhibited a very characteristic pattern composed of fibres that seemed to be fairly aligned with the direction of migration. The analysis through Orientation J revealed that the fibres of the three proteins, but specially of fibronectin, were preferentially oriented near 0º, that is to say, aligned perpendicularly with the migration front (Figure 4.3.11, (b)). These results indicate that fibroblasts deposit ECM fibres that we speculate might be used as tracks for the epithelial cells to migrate.

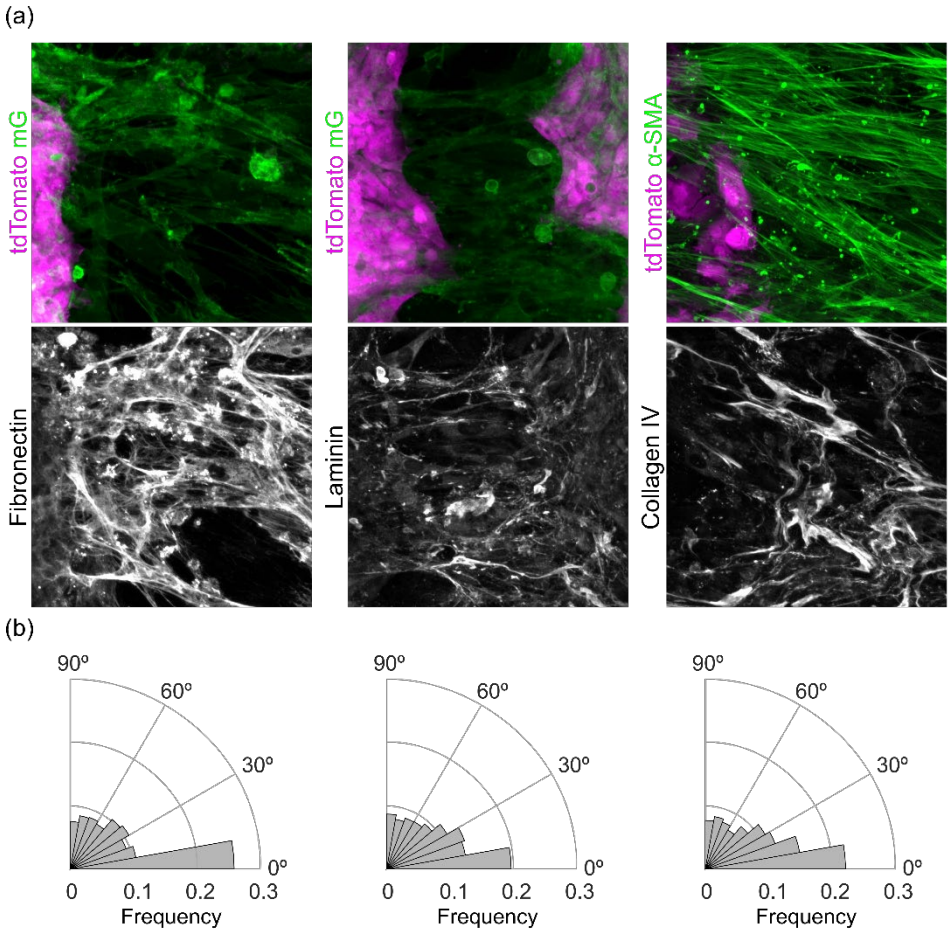

Figure 4.3.11. (a) Sum intensity projections of *+ fibroblasts* samples at 24h upon barrier removal stained for fibronectin, laminin or collagen IV, with tdTomato (epithelial cells) and mG or α-SMA (fibroblasts). (b) Polar histograms of the fibbers' orientation of each protein. 0º corresponds to parallel alignment to the migration direction and 90º, perpendicular. Mean ± SEM. N ≥ 1 independent experiment.

Together with the observation that fibroblasts align with epithelial cells and perpendicular to the migration front, and the increased directionality of epithelial migration on the *+ fibroblasts* samples, we conclude that the physical presence of fibroblasts upon epithelial migration results in (i) higher epithelial integrity (compared to in their absence), and (ii) greater directed epithelial migration (compared to in their absence or in the presence of only their paracrine signalling).

4.4. Incorporating the stromal compartment is required for epithelial growth in a villus-like GelMA-PEGDA *in vitro* model

As mentioned in the introduction, the maintenance of epithelial homeostasis depends on intestinal fibroblasts, which are present within a 3D connective tissue called lamina propria. Thus, to faithfully recreate the intestinal mucosa, *in vitro* models should not only recreate the native architecture, but also incorporate stromal cells in a lamina propria-mimicking compartment and, allow the culture of organoid-derived epithelial cells. However, to achieve a platform that combines the three features has been extremely challenging. Indeed, to the best of our knowledge, only one study attempted so[66]. In the previous section, we described the engineering of a 2D *in vitro* system that allowed the co-culture of fibroblasts with epithelial cells. On the other hand, in the lab we have developed a customised DLP-based bioprinting technique that allows to print villus-like GelMA-PEGDA hydrogels. In the section presented here, we intend to use the in-house DLP-based bioprinting technique to fabricate villus-like GelMA-PEGDA hydrogels with embedded fibroblasts and organoid-derived single cells on top. Within this platform, we aim to investigate the impact of fibroblasts on epithelial growth.

4.4.1. The in-house DLP-based bioprinter allows to fabricate GelMA-PEGDA hydrogels with villus-like pillars and native tissue-like mechanical properties

To be able to print GelMA-PEGDA hydrogels using the customised DLP-based bioprinter, we first had to optimise both the composition of the bioink (section 3.4.2) and the printing conditions (mainly layer thickness and exposure time). To ease this initial optimization step, we first used flat designs so that the complexity associated with the 3D structures was avoided. The optimised bioink contained 5% GelMA, 3% PEGDA, 1% LAP and 0.025% Tartrazine and the optimised printing conditions were 13 μm of layer thickness and 5 s of exposure time. 24 h after printing, once the swelling had reached equilibrium (this data can be found in Torras et al.[75]), we characterised the morphology of the resulting hydrogels using a stereo microscope (Olympus, SZX2-ILLB) (Figure 4.4.2).

Then, we attempted to include the high aspect ratio villus-like microstructures in the GelMA-PEGDA hydrogels using several CAD designs with different pillar dimensions prepared previously in the lab[75]. After numerous tests, the selected CAD design consisted in a flat disk of 6 mm in diameter and 150 μm in height with pillars of 300 μm in diameter and 700 μm in height (Figure 4.4.1 (a)). Using the same hydrogel composition and printing settings optimized to print the flat hydrogels, we could successfully print the villus-like hydrogels.

After swelling, the villus-like pillars were of approximately 700 µm in height (Figure 4.4.1 (b)), exactly the same as the design, suggesting a much lower swelling than the one experienced by PEGDA-only hydrogels[69,85]. Moreover, the obtained dimensions were also in the range of those reported for mouse villi[117].

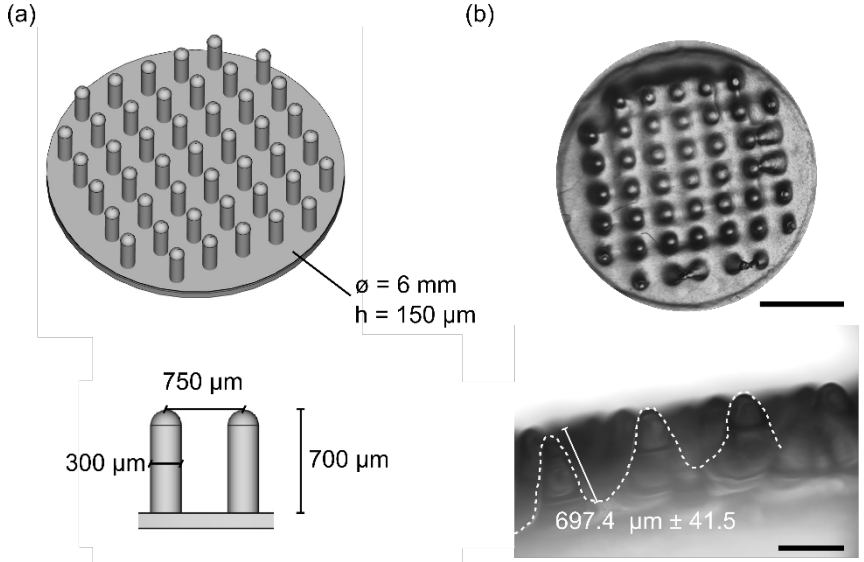

Figure 4.4.1. Top and lateral views of (a) CAD design with the selected dimensions (b) Printed villus-like scaffolds. Scale bars = 2 mm (top views) and 500 µm (lateral views).

Next, to validate the potential of these hydrogels for the fabrication of intestinal mucosa models, it was fundamental to evaluate their mechanical properties. For that, we performed rheological tests on the GelMA-PEGDA flat hydrogels of 8 mm in diameter, and we obtained an average value for the storage modulus of ≈ 2 kPa, which corresponds to an apparent elastic modulus of ≈ 6 kPa, assuming a Poisson coefficient of 0.5.

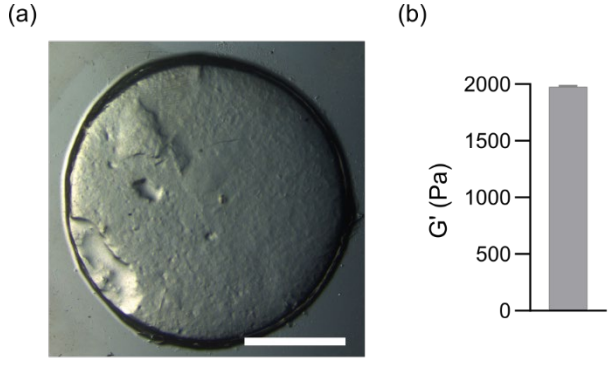

Figure 4.4.2. (a) Stereo microscope picture of a GelMA-PEGDA hydrogel after swelling. Scale bars: 2 mm. (b) Graph showing the storage modulus (G') measured for GelMA-PEGDA hydrogels. Mean ± SD.

Since the elastic modulus of our GelMA-PEGDA hydrogels is in the range of the reported elastic modulus for the intestine[49] (11 kPa), we considered our hydrogels to have native-tissue like mechanical properties.

So, all in all we established the prepolymer composition, the CAD design and the printing parameters that allowed us to obtain hydrogels with microstructures resembling the native villi and with elasticity in the range of the intestinal tissue.

4.4.2. NIH/3T3 fibroblasts can grow when embedded in GelMA-PEGDA hydrogels

Once the suitability of the customised DLP-SLA technology to print GelMA–PEGDA hydrogels with villus-like architecture and tissue-like mechanical properties was confirmed, the feasibility to embed stromal cells within the hydrogels was evaluated. For that, we embedded NIH/3T3 fibroblasts in GelMA-PEGDA hydrogels, and we assessed their viability through the Calcein-AM/ethidium homodimer live/dead assay and confocal microscopy 1 and 7 days after printing. At day 1, almost 90% of the cells were alive and homogeneously distributed within the hydrogel (Figure 4.4.3), suggesting that the DLP-SLA bioprinting technique employed here was not appreciably stressful for the cells. At day 7, the high cell viability was maintained, with 90% of cells alive, suggesting that the material did not have a cytotoxic effect.

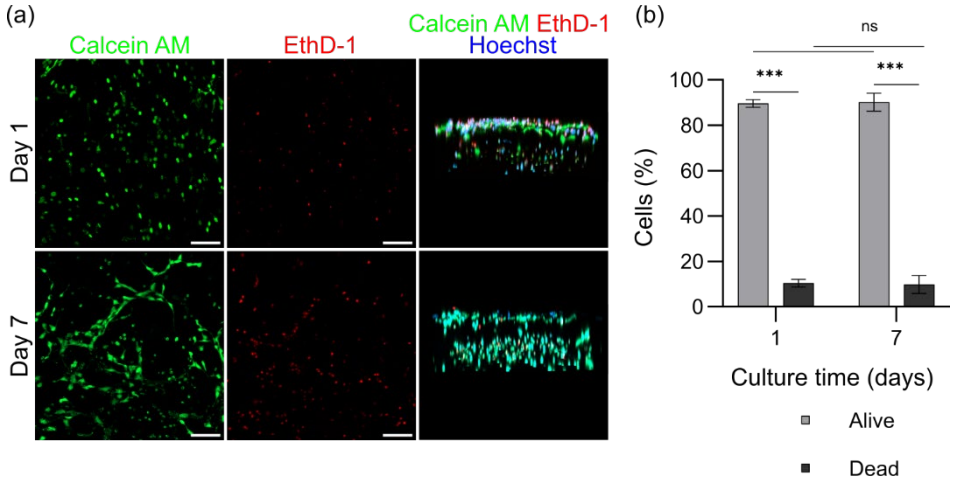

Figure 4.4.3. NIH/3T3 fibroblasts viability within GelMA-PEGDA hydrogels across time. (a) Maximum intensity projections (two left panels) or 3D reconstruction of representative samples at days 1 and 7 after embedding. Scale bars = 100 µm. (b) Quantification of the percentage of cells alive and dead based on live/dead staining. Mean ± SD. T-test, (***) $p<0.001$. N = 2, n ≥ 7.

Next, we observed that, over time, the hydrogels became more and more crowded with fibroblasts. To quantify this observation, we immunostained samples with rhodamine-phalloidin to visualize F-Actin cytoskeleton and we

measured the surface coverage (Figure 4.4.4). At day 4 of culture, surface coverage was already at 75%, and it reached more than 96% by day 11. Overall, these results confirm the suitability of this bioprinting technology for the successful embedding of NIH/3T3 fibroblasts. However, whether this increase in surface coverage was caused by cell proliferation and/or by the migration of cells from the hydrogel's bulk towards the surface was not clear.

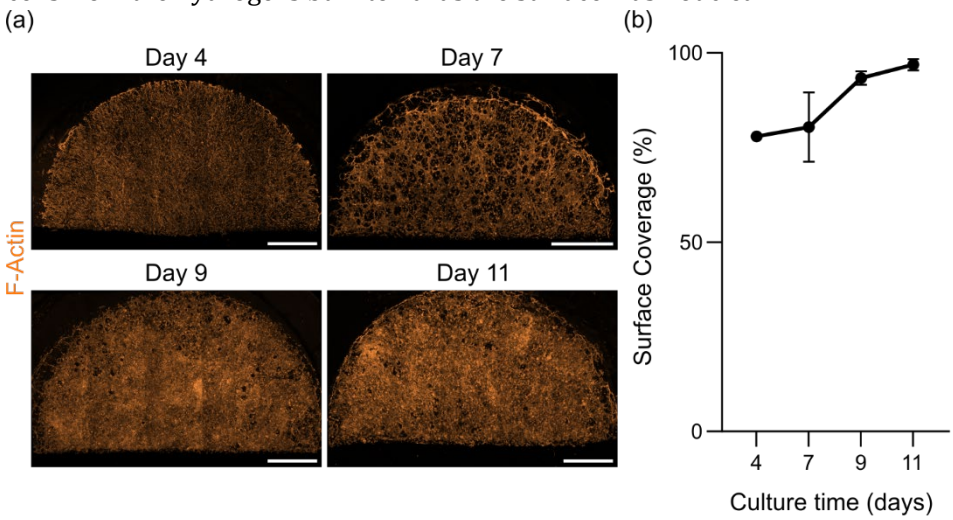

Figure 4.4.4. Surface coverage of NIH/3T3 fibroblasts within GelMA-PEGDA hydrogels at days 4, 7, 9 and 11 after embedding. (a) Maximum intensity projections of representative samples immunostained with rhodamine-phalloidin (F-Actin). Scale bars = 1000 µm. (b) Quantification of the surface coverage. Mean ± SEM. N = 2, n ≥ 1.

To address this question, we first assessed the proliferative capacity of these fibroblasts when embedded in GelMA-PEGDA hydrogels. For that, we immunostained samples with Ki67 antibody at different time points (e.g., days 4, 7, 9 and 11) (Figure 4.4.5). We found that there was a relatively high amount of cells positive for this marker already at day 4 after printing (33.1% ± 5.1), and that a proliferative cell population was well conserved over time for at least 11 days (31.5% ± 6.5). These results suggested that these GelMA-PEGDA hydrogels successfully enabled the cells embedded within to undergo different phases of the cell cycle and thus remain functional for at least 11 days. Together with the small percentage of dead cells (Figure 4.4.2 (b)), it appears that cell proliferation is contributing to the increase in surface coverage observed.

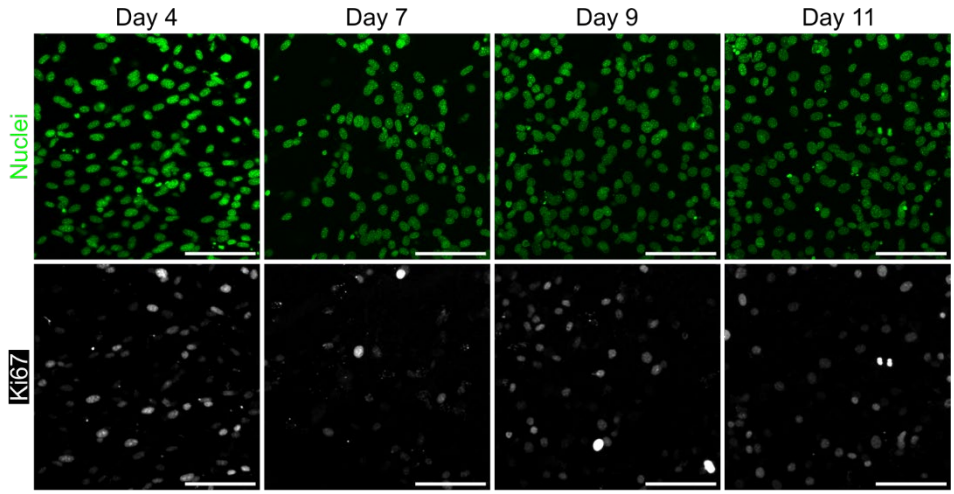

Figure 4.4.5. Maximum intensity projections of GelMA-PEGDA hydrogels with NIH/3T3 embedded immunostained with DAPI (nuclei) and Ki67 at days 4, 7, 9 and 11 after printing. Scale bars = 100 µm.

Next, we addressed the contribution of cell distribution within the hydrogel in the apparent increase of surface coverage. To gain knowledge on the 3D distribution of NIH/3T3 cells in the hydrogel, we obtained orthogonal histological cuts by embedding the samples first in $PEGDA_{575}$ and later in OCT (section 3.4.7).

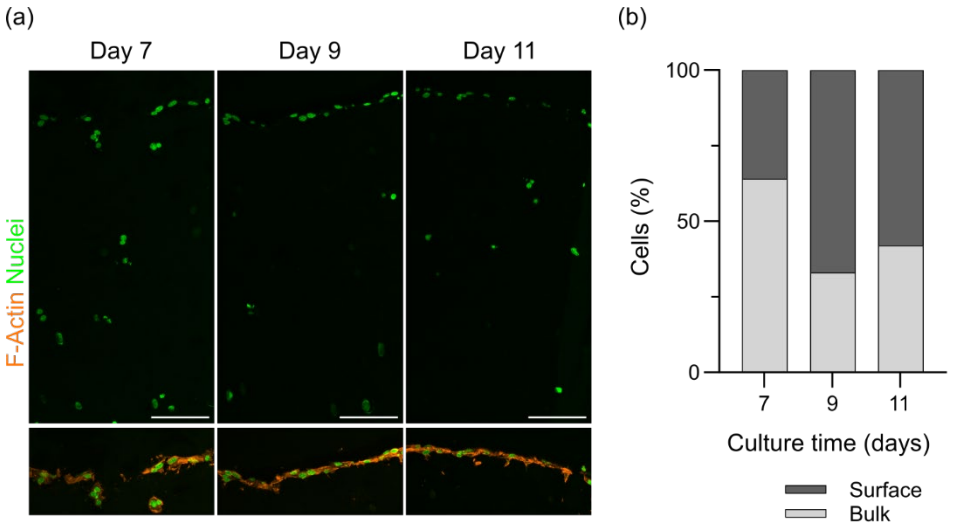

Figure 4.4.6. NIH/3T3 fibroblasts distribution across the thickness of GelMA-PEGDA hydrogels at days 7, 9 and 11 after printing. (a) Maximum intensity projections of cuts of samples embedded in $PEGDA_{575}$ and OCT immunostained with rhodamine-phalloidin (F-actin) and DAPI (nuclei). Scale bars = 100 µm. (b) Quantification of the percentage of cells in the surface vs in the bulk. Mean. N = 1, n = 1.

Then, by immunostaining with rhodamine-phalloidin (F-actin) and DAPI (nuclei), we could see that, initially (at day 4), there were some roundish cells in the bulk of the hydrogel, either as single cells or as small clusters, and there were fibroblasts at the hydrogel surface that were already spread (Figure 4.4.6). At day 9, the cells in the bulk were less than in prior timepoints, although they had the same roundish shape as in day 4, whereas the surface was almost fully crowded by fibroblasts (in line with the surface coverage percentage). At day 11, the surface of the hydrogel was covered by a complete monolayer of fibroblasts, whereas in the bulk we could spot approximately the same percentage of cells as day 9. Thus, the results suggest that, as culture time went by, the surface of the hydrogels became more and more populated by fibroblasts, finally creating a continuous monolayer. At the same time, the proportion of cells found in the bulk of the hydrogel slightly diminished. Overall, the fabricated GelMA-PEGDA hydrogels seem to allow cells to move and to undergo their cell cycle.

Fibroblasts are well-known for their capacity to produce and secrete ECM proteins, which, together with stromal cells, constitute the lamina propria of the intestinal mucosa. In particular, we wanted to evaluate if the NIH/3T3 fibroblasts embedded within the GelMA-PEGDA hydrogels were able to secrete proteins of the intestinal basement membrane, the layer right beneath the epithelium[118].

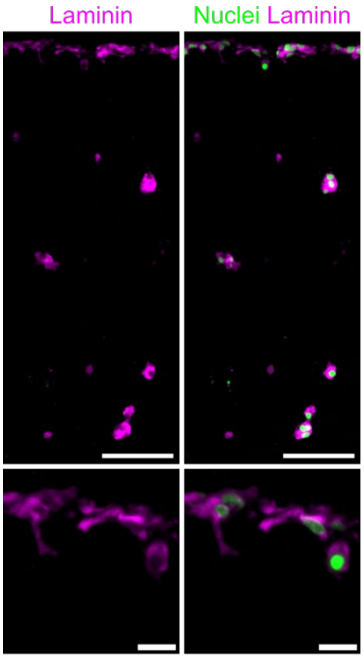

Figure 4.4.7. Average intensity projections of cuts of samples 9 days after printing embedded in $PEGDA_{575}$ and OCT immunostained with DAPI (nuclei) and Laminin. Scale bars of panels above = 100 µm. Scale bars of panels below = 20 µm.

To do so, we immunostained histological cuts with an antibody against laminin, one of the main constituents of the intestinal basement membrane [119], and DAPI to identify the cells' nuclei (Figure 4.4.7). We could observe that NIH/3T3 fibroblasts express the laminin protein, an important protein for cell adhesion.

4.4.3. Stromal fibroblasts allow the growth of organoid-derived single cells on GelMA-PEGDA hydrogels

Once we assessed that the NIH/3T3 fibroblasts could successfully grow inside the GelMA-PEGDA hydrogels for at least 11 days, we proceeded to evaluate if these hydrogels would allow the culture of organoid-derived cells. For that, cell-free flat GelMA-PEGDA hydrogels were first printed as detailed in section x and immediately mounted onto Transwell inserts. 4 days after the printing, intestinal organoids were digested into single cells as detailed in section x and seeded on the scaffolds ($3x10^5$ single cells per scaffold). By immunostaining against F-Actin, we observed that 3 days after the seeding there were almost no cells attached (Figure 4.4.8). Throughout the whole surface of the hydrogel, we could find one single epithelial cluster. Maintaining the culture for 2 more days did not yield any better outcome. Thus, despite the innate presence of cell adhesion cues in these hydrogels provided by GelMA, we could conclude that organoid-derived epithelial cells could not grow on these hydrogels.

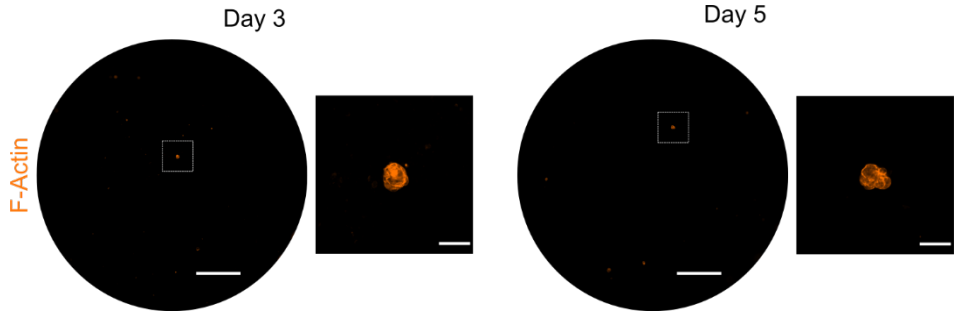

Figure 4.4.8. Maximum intensity projections of representative samples of organoid-derived single cells cultured on cell-free GelMA-PEGDA hydrogels fixed 3 and 5 days after the seeding immunostained with rhodamine-phalloidin (F-actin). Scale bars = 1000 µm. Zoom-ins scale bars = 100 µm.

Next, we tested if these same cells would grow on fibroblast-laden hydrogels. For that, we followed the same printing, mounting and culturing procedure described above but with GelMA-PEGDA hydrogels with embedded NIH/3T3 fibroblasts. In this case, we observed that 1 day after seeding, the epithelial single cells had gathered together forming multicellular clusters that occupied 15% of the surface. 2 days later, we observed that these clusters had merged with each other forming larger epithelial patches.

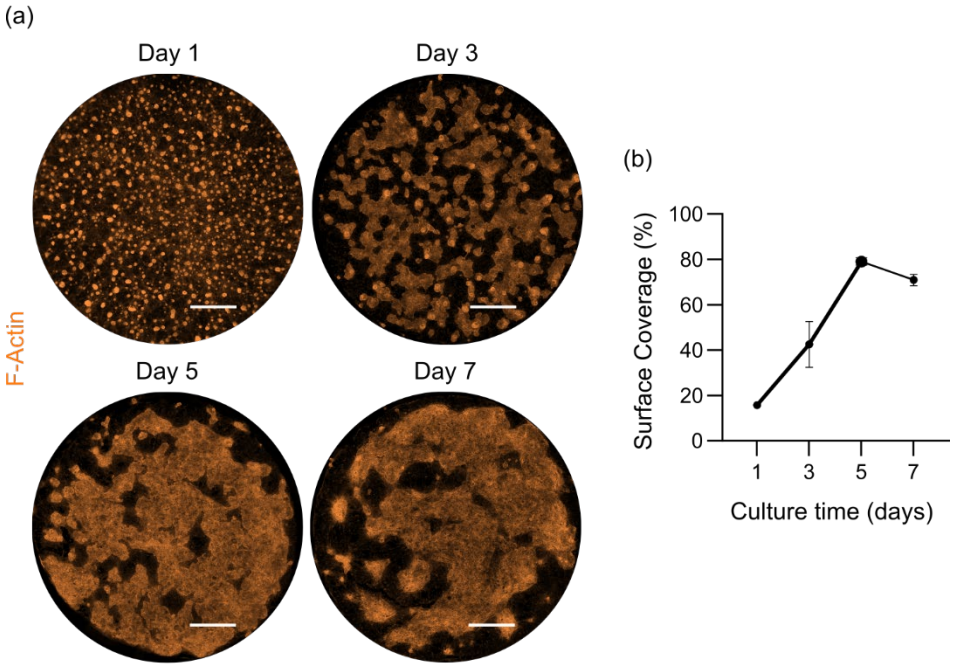

Figure 4.4.9. Surface coverage of single cells derived from organoids on GelMA-PEGDA hydrogels with embedded NIH/3T3 at days 1, 3, 5 and 7 after seeding. (a) Maximum intensity projections of representative samples immunostained with rhodamine-phalloidin (F-actin). Scale bars = 1000 μm. (b) Quantification of the surface coverage. Mean ± SEM. N ≥ 1, n ≥ 1.

At day 5 after seeding, the patches had expanded forming a quasi-continuous monolayer that took over almost 80% of the surface. Continuing the culture for 2 more days (day 7 after seeding) did not result in a further progression of the monolayer, rather there was even a bit of retraction (surface coverage ≈ 70%). Still, these results strongly suggest that the addition of fibroblasts to the model enabled the adhesion of organoid-derived epithelial cells and consequently, their growth.

4.4.4. Fibroblasts embedded within GelMA-PEGDA hydrogels surround, make direct contact and lead the expansion of organoid-derived clusters

In light of these results, we aimed to elucidate by which mechanism the fibroblasts were promoting the growth of the organoid-derived epithelial cells. To do so, we designed a live-imaging experiment to see how the two cell types behaved in co-culture. For that, we used fluorescent NIH/3T3 (LINTERNA NIH/3T3), and mT organoid-derived epithelial cells to be able to follow them using fluorescence microscopy. Noteworthy, the low ratio of fluorescent vs total fibroblasts despite culturing them with the appropriate selection antibiotic, significantly eased their visualization, especially when co-cultured with the epithelial cells. 4 days after printing the fibroblast-laden hydrogels, we seeded

the single cells derived from organoids, and 1 day after, we acquired a 12-hour time-lapse video. Interestingly, we could clearly observe how the fibroblasts approached and made physical contact with the epithelial clusters (Figure 4.4.10).

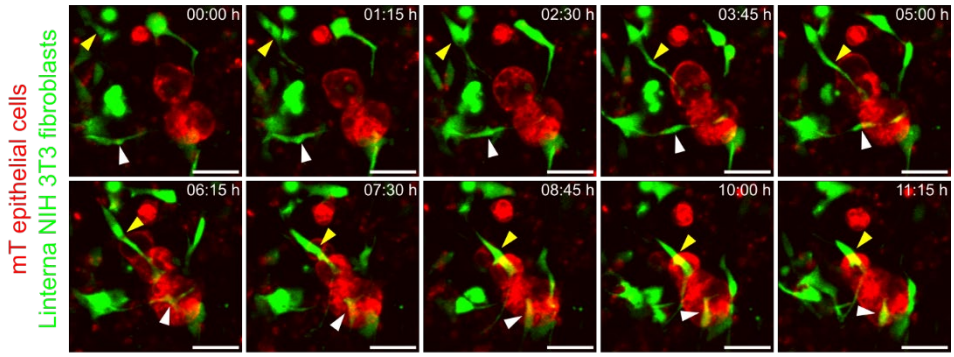

Figure 4.4.10. Representative snapshots of time-lapse experiments of GelMA-PEGDA hydrogels with embedded fibroblasts and organoid-derived cells on top. Time 00:00h corresponds to 1 day after the seeding, and to 5 days after the printing of the hydrogels. Arrow heads highlight 2 fibroblasts (one with white and another one with yellow) migrating towards the cluster of epithelial cells. Scale bars: 50 µm.

In sum, these results go in line with the results obtained in section 4.2, where we showed that the physical presence of fibroblasts was fundamental for epithelial cells to efficiently migrate and maintain its integrity in a gap closure model. In this section, we have again demonstrated the importance of fibroblasts within the culture, as without them, epithelial cells are not even able to attach to the hydrogel.

To gain further insight into this cross-talk between fibroblasts and epithelial cells in these experiments, we did a series of immunostainings at different time points and we looked at how the two cell types organized within the culture (Figure 4.4.11). By immunostaining with α-SMA antibody, we were able to distinguish the fibroblasts from the epithelial cells. Strikingly, we observed that 3 days after seeding the organoid-derived single cells on top of the fibroblast-laden hydrogels, the epithelial cells had first gathered together forming multicellular 3D clusters, and, while some of the fibroblasts embedded within the hydrogel were underneath the clusters, most of them were radially surrounding them, suggesting a physical interaction between the two cell types. Indeed, in some specific regions, we could observe the emergence of tongues of epithelial cells (highlighted with arrow heads) protruding from the main cluster, coinciding with aligned fibroblasts.

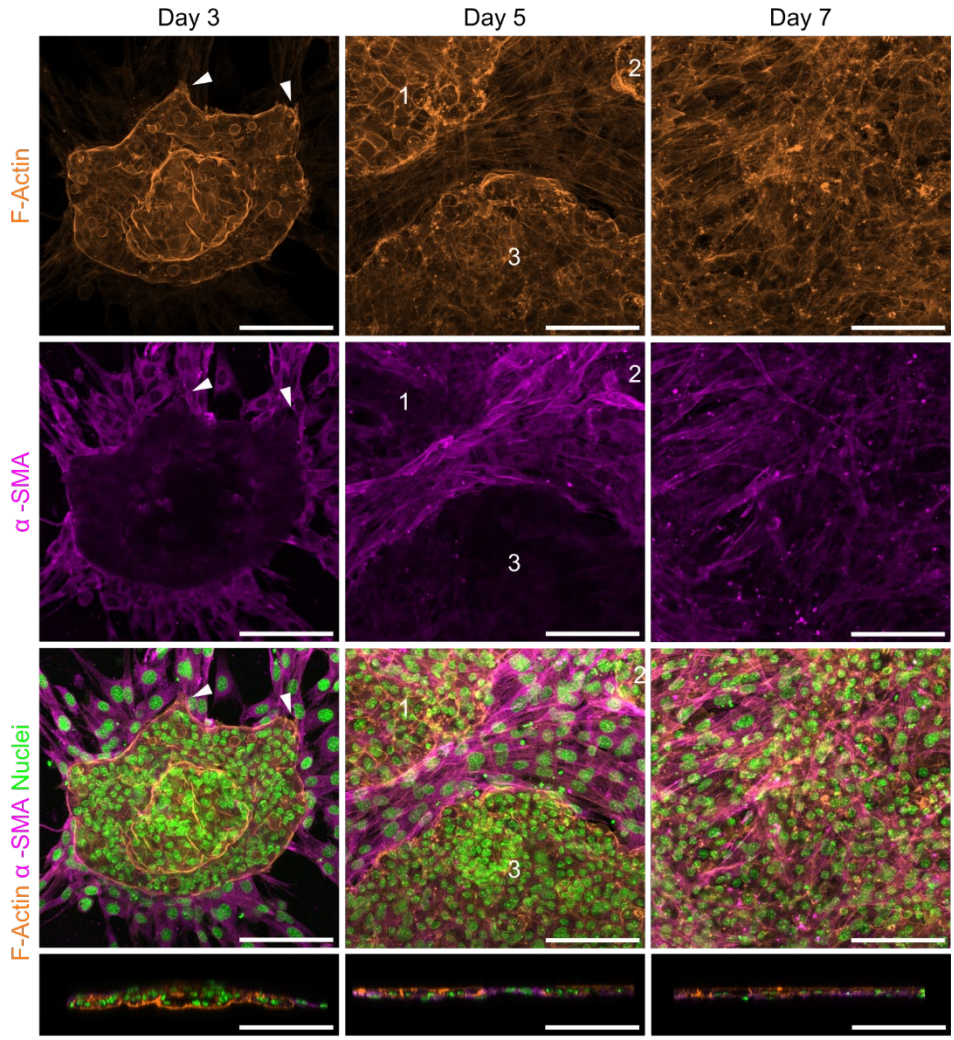

Figure 4.4.11. Maximum intensity projections (first three panels above) or orthogonal views (last panel below) of representative samples immunostained with rhodamine-phalloidin (F-actin), α-SMA and DAPI (nuclei) of days 3, 5 and 7 after seeding. Arrow heads in left panel indicate the tongues of epithelial cells coming out of the main cluster. Numbers in middle panel identify the epithelial clusters. Scale bars = 100 μm.

These results, which are truly reminiscent of what we described in section 4.3, might suggest that the fibroblasts could be pulling from the epithelial cells to help them spread over the hydrogel surface, in other words, enabling the epithelial cells to transition from 3D clusters to 2D monolayers. 2 days later (day 5 after the seeding), we could observe perpendicular F-Actin and α-SMA fibbers of fibroblasts connecting two epithelial clusters that were far apart (clusters 1 and 2), while between closer clusters (clusters 1 and 3), the fibroblasts disposed in parallel respect to the clusters. At later stages (7 days after the seeding), we could see that all over the surface there were fibroblasts with a rather

anisotropic disposition, and right on top there was a complete epithelial monolayer.

These differences in fibroblasts' orientation in respect to the monolayer over time, suggest that the cross-talk between the two cell types arouses an active response of the fibroblasts population: (i) when epithelial cells are distributed as isolated clusters, fibroblasts move towards the clusters, position themselves perpendicular to them and lead their spreading; (ii) upon epithelial migration, fibroblasts at one migration edge may collide with the ones at the migration edge of a neighbouring epithelial cluster, resulting in their perpendicular arrangement to the edge; and finally, (iii) when the epithelium reaches confluence, fibroblasts distribute underneath with no preferential orientation.

4.4.5. Organoid-derived monolayers on fibroblast-laden GelMA-PEGDA hydrogels display crypt-like regions

Next, we characterized the engineered organoid-derived epithelial monolayers in terms of different cell types and their organization. Specifically, we scanned the monolayers looking for crypt-like regions by analysing the presence and distribution of both Ki67$^+$ proliferative cells and Lgr5-GFP$^+$ stem cells. At days 3 and 5 after the seeding of organoid-derived cells, we observed the presence of regions where cells had a smaller area, more compacted nuclei and positive signal for Ki67 (Figure 4.4.12), which we identified as crypt-like regions [88].

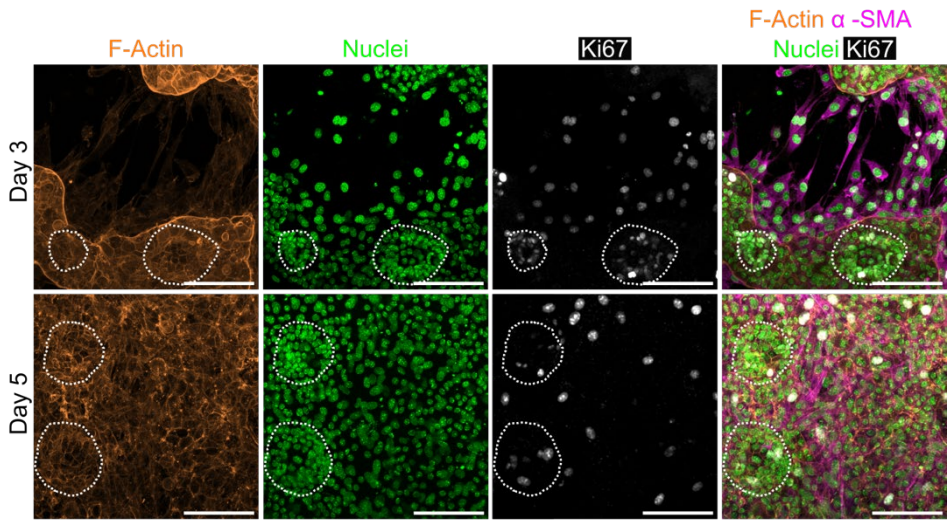

Figure 4.4.12. Maximum intensity projections of representative samples immunostained with rhodamine-phalloidin (F-actin), α-SMA, DAPI (nuclei) and Ki67 antibodies at days 3 and 5 after seeding. Dotted areas indicate crypt-like regions. Scale bars = 100 μm.

We also observed the presence of stem cells (Lgr5⁺) expressing GFP in those crypt-like regions (Figure 4.4.13). Altogether, these results show the suitability of GelMA-PEGDA hydrogels with embedded NIH/3T3 fibroblasts to allow the growth of homeostatic-like organoid-derived epithelial monolayers.

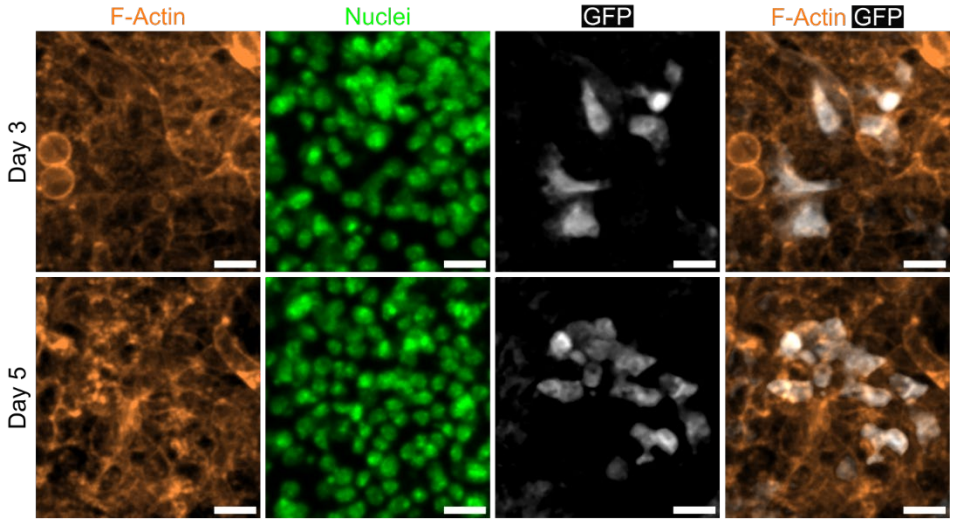

Figure 4.4.13. Maximum intensity projections of representative samples immunostained with rhodamine-phalloidin (F-actin), DAPI (nuclei), and GFP (Lgr5⁺ stem cells) antibodies at days 3 and5 after seeding. Scale bars = 20 µm.

4.4.6. Microstructuring GelMA-PEGDA hydrogels in villus-like pillars impacts on the localization of the embedded NIH/3T3 fibroblasts

Having confirmed that fibroblast-laden GelMA-PEGDA allow the growth of organoid-derived monolayers in flat samples, we proceeded to incorporate the three-dimensionality of the villus-like pillars. For that, we fabricated villus-like GelMA-PEGDA hydrogels with embedded fibroblasts (section 3.4.4). Next, we assumed that these 3D hydrogels would exhibit the same mechanical properties as the flat ones. Similarly, we considered that the viability of the NIH/3T3 fibroblasts embedded within the 3D hydrogels would be similar to that of the 2D samples in the time scale evaluated, since the material composition did not change. Yet, what was not straight forward was if the incorporation of villus-like microstructures into the hydrogel would affect the distribution of fibroblasts. To evaluate this, we fabricated villus-like GelMA-PEGDA hydrogels with embedded NIH/3T3 (section 3.4.4) and we studied how the cells were distributed across the hydrogel and if this distribution changed over culture time (Figure 4.4.14).

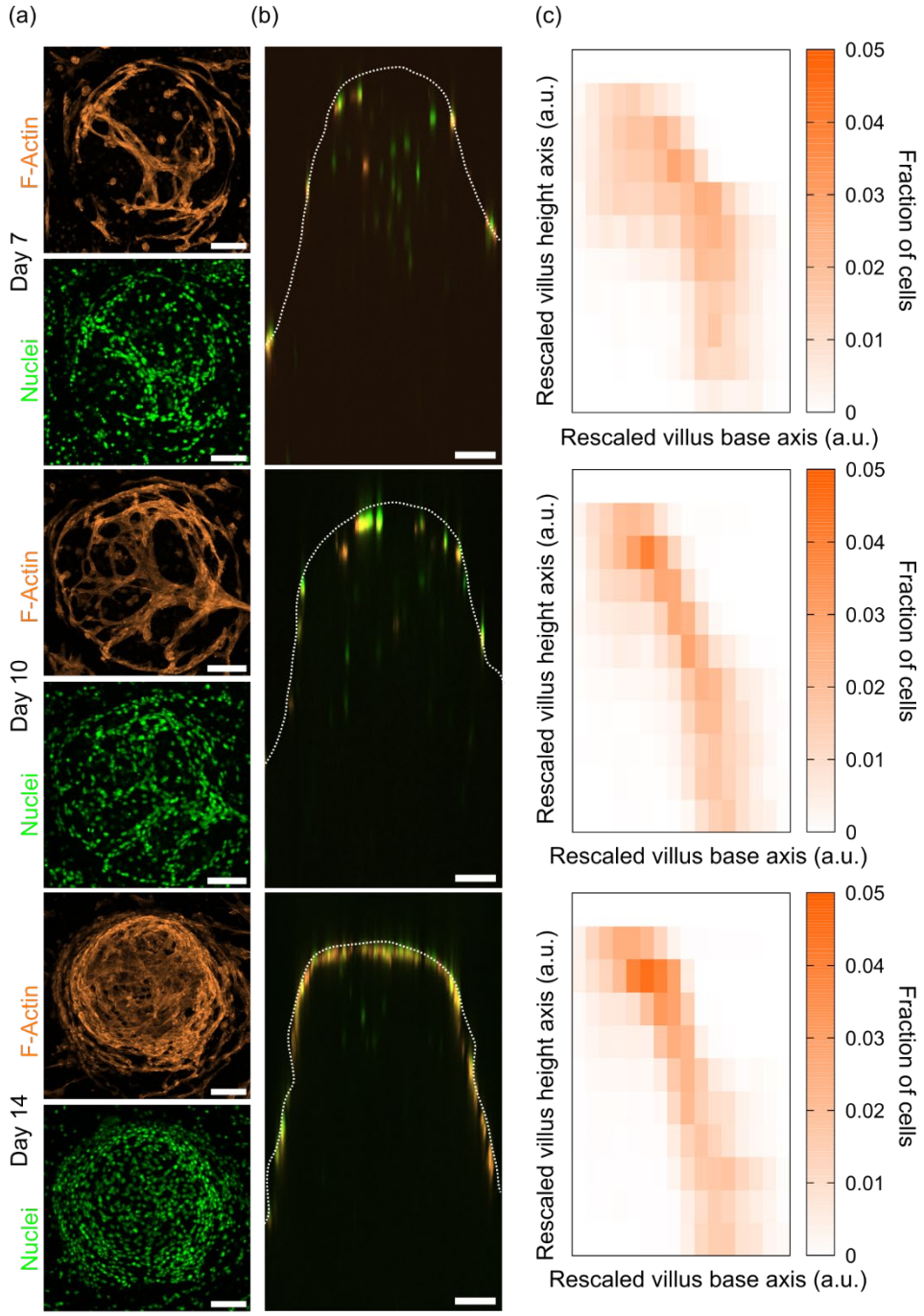

Figure 4.4.14. Representative images immunostained with rhodamine-phalloidin (F-Actin) and DAPI (nuclei). Scale bars = 100 µm. (a) Maximum intensity projections (b) Cross sections. (c) Graphs plotting the distribution of cells across the height and the radius of the villi. Day 7: 4 pillars, Day 10: 8 pillars, Day 14: 8 pillars. Top panel: day 7. Middle panel: day 10. Bottom panel: day 14.

More in detail, after corresponding immunostaining and imaging, within each individual villus-like pillar (spanning from the base to the tip), we detected fibroblasts' nuclei and we plotted an histogram displaying the fraction of cells as a function of their position in the villus height and villus base axes. What we observed was that at early timepoints (day 7), cells were rather homogeneously distributed throughout the pillars there were some inside and some already close to or on the surface. Three days later (day 10) and specially seven days after seeding (day 14 after fabrication), we clearly observed the tendency of fibroblasts to accumulate at the surface of the pillars and leave empty the inside (Figure 4.4.14). Indeed, this is analogous to what we observed in the case of the flat hydrogels (Figure 4.4.6). However, in the case of the 3D structures, fibroblasts are not evenly distributed on the hydrogel-medium interphase, but they accumulate at the tip (Figure 4.4.14).

We speculate that the heterogeneous distribution of fibroblasts within the villus-like hydrogels can lead to differences in growth and morphology within the fibroblastic population. In flat hydrogels, we observed that organoid-derived epithelial cells could only grow on GelMA-PEGDA hydrogels when there were fibroblasts embedded. Moreover, we could see how fibroblasts were physically interacting with epithelial clusters and leading their expansion into monolayers. Therefore, we anticipate that this anisotropic distribution of fibroblasts within the villus-like hydrogels can affect how epithelial cells grow once seeded.

4.4.7. Villus-like fibroblast-laden hydrogels sustain the growth of organoid-derived epithelial cells

To elucidate if the asymmetric distribution of fibroblasts within the villus-like PEGDA-AA hydrogels had an impact on how organoid-derived cells grew, we first printed villus-like hydrogels with embedded NIH/3T3 (section 3.4.4). Then, seven days later, when we observed that the fibroblasts started to accumulate at the interface between the cell culture medium and the hydrogel, we seeded the epithelial cells on top (section 3.4.5). Three days after the seeding, we observed that epithelial cells had attached to specific regions of the hydrogel, namely, the tip and the base of the villi, and were forming a monolayer (Figure 4.4.15 (a)). In regard to the fibroblasts, we noticed that at day 3 after seeding the epithelial cells (ten days after printing), they were mainly localized beneath them, leaving almost empty the regions without monolayer. Moreover, beneath the monolayer, they started to form a multilayer and to acquire a more spindle-like morphology, as seen by more elongated nuclei (Figure 4.4.15 (b), (c)).

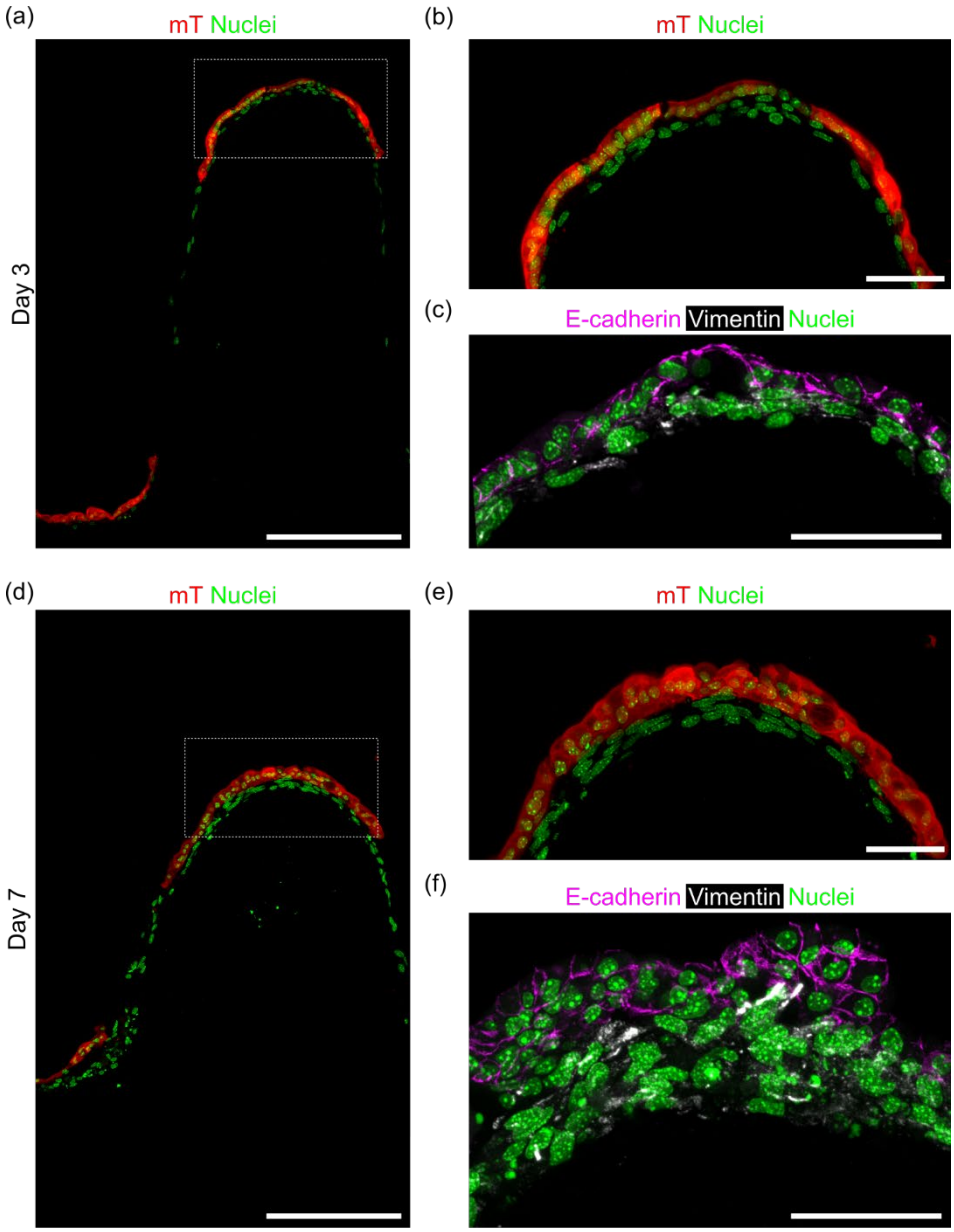

Figure 4.4.15. Maximum intensity projections of cuts of GelMA-PEGDA hydrogels with 3T3 fibroblasts inside and mT organoid derived epithelial cells on top immunostained with DAPI (nuclei). Top panels (a), (b) and (c) correspond to day 3 after seeding. Bottom panels (d), (e) and (f) correspond to day 7 after seeding. (a) (d) Full length villus-base unit. Scale bars: 200 μm (b) (e) Zoom-ins of (a) (d). Scale bars = 50 μm. (c) (f) Cuts immunostained with E-cadherin, Vimentin and DAPI. Scale bars = 50 μm.

Four days later (that is to say, day 7 after seeding and fourteen days after the printing), the monolayers occupied approximately the same surface as the previous timepoint, there was no retraction nor any progression towards the

walls of the villi, which are the less curved parts of the hydrogel (Figure 4.4.15 (d)).

At this timepoint, there were more fibroblasts than at day 3, but still there was a clear difference between the regions with an epithelial monolayer on top, where there were more fibroblasts, and the regions without. Not only was there a difference in quantity but those beneath the monolayer seemed to be more elongated and foremost, more aligned with the outline of the hydrogel (Figure 4.4.15 (d), (e)). We also observed that the regions with a multilayer of stromal cells increased with time and increased with the presence of epithelial cells on top (Figure 4.4.15 (f)).

Having a closer look at the epithelial cells over time, we observed that at day 3 after seeding, they formed a single layer, had a columnar shape, and seemed well attached to the hydrogel (Figure 4.4.15 (b)), whereas at day 7, some regions had more than one layer of epithelial cells, and those had a more roundish morphology (Figure 4.4.15 (e)), suggesting poor cell attachment possibly prior to cell shedding. Overall, maintaining the samples in culture for longer did not result in epithelial cells covering a larger portion of the hydrogel surface, instead, they remained at the base and at the tip of the microstructures. Intriguingly, at any given culture timepoint, fibroblasts disposed slightly differently if cocultured with epithelial cells or not. For instance, at day 14 after printing, fibroblasts cultured alone were homogenously distributed along the outline of the hydrogel with a slight preference for the tip (Figure 4.4.16 (a, left)). Instead, in the presence of organoid-derived cells, the walls of the pillars were rather depleted from fibroblasts (Figure 4.4.16 (a, right)). These results suggest once again that fibroblasts are able migrate within these GelMA-PEGDA hydrogels, but, what's more important, it seems that they sense epithelial cells and migrate to mainly position right beneath where epithelial cells are located.

Not only did we unveil this influence of epithelial cells in drawing the migration of fibroblasts towards them but we also spotted differences in the morphology of fibroblasts depending on if they had epithelial cells on top or not (Figure 4.4.16 (a)). To further study this, we segmented fibroblasts' nuclei, and we quantified their elongation. We observed that when fibroblasts were cultured alone, their nucleus was significantly less elongated than when fibroblasts were cocultured with organoid-derived epithelial cells. Differences in nuclei elongation have been previously linked to curvature variations[120]. However, since in both cases the fibroblasts experience the same curvature, we attribute this effect directly to the presence of epithelial cells.

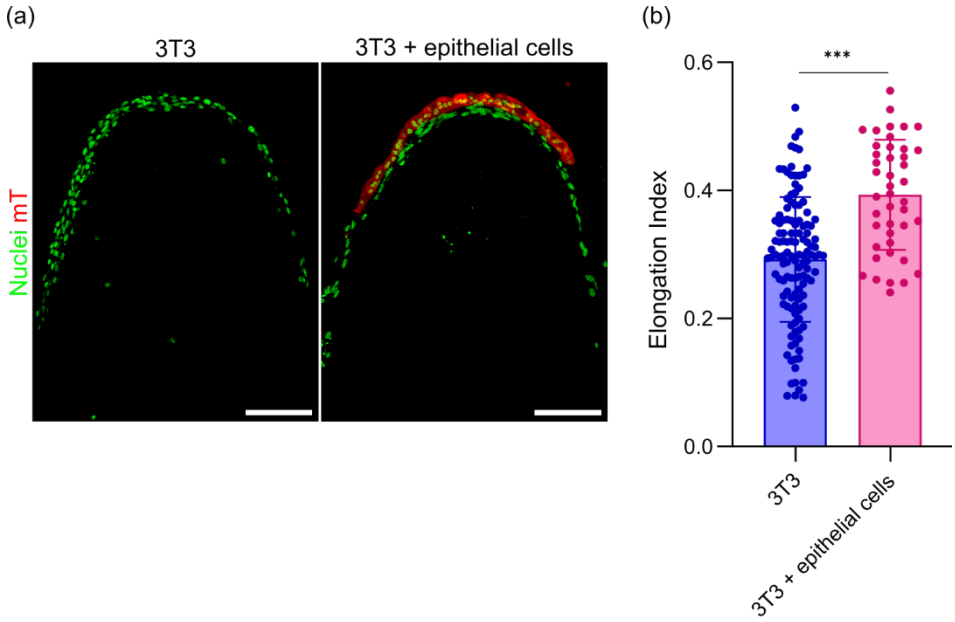

Figure 4.4.16. (a) Maximum intensity projections of cuts of GelMA-PEGDA hydrogels with 3T3 fibroblasts inside or 3T3 fibroblasts inside and mT organoid-derived epithelial cells on top at day 14 after printing immunostained with DAPI (nuclei). Scale bars: 100 µm. (b) Elongation index of nuclei for each condition. Mean ± SD. T-test. (***) $p < 0.001$.

Overall, the experiments in this section demonstrate the requirement that epithelial cells have of fibroblasts to grow on GelMA-PEGDA hydrogels. In its turn, this demonstrates the importance of developing physiological-like *in vitro* to further investigate the epithelium-stroma crosstalk.

5. Discussion

The rise of new and sophisticated microfabrication techniques, together with the research of new materials to mimic the ECM such as hydrogels and the emergence of organoids as physiologically relevant new cell culture models has transformed the field of bioengineered *in vitro* models[121]. Because the intestinal epithelium is the tissue where most nutrient and water absorption takes place[1,122], there has been a great interest to develop intestinal *in vitro* models to perform drug absorption and permeability tests. Moreover, given that it is one of the tissues with the highest cell turnover, *in vitro* models of the intestinal epithelium are recognized as highly valuable to study stem cell biology and maintenance of tissue homeostasis.. However, so far, no current *in vitro* model can fulfil all the desired features, i.e. direct access to the apical side, tissue mechanical properties, native crypt-villus architecture, bearing *in vivo* biochemical gradients, physiologically relevant epithelial cell model and mimicking of the mesenchymal compartment. Instead, the best strategy seems to be the engineering of *in vitro* platforms according to the specific aim desired. This thesis aimed at contributing to this field by engineering *in vitro* models of the small intestine that incorporate, in different levels, the input from the stroma. First (sections 4.1 and 4.2), we used synthetic hydrogels to generate intestinal epithelial models with relevant features of the intestinal architecture which could incorporate signalling biochemical gradients to achieve native-like cell compartmentalization. Then, we directly incorporated the cellular stromal compartment by creating co-cultures of primary mesenchymal and epithelial cells (sections 4.3 and 4.4). This was achieved both in 2D and 3D models that allowed us to study the effects of the stromal compartment in epithelial growth and migration.

As explained before, the characteristic 3D architecture of the intestinal epithelium composed of crypt and villus units serves several organic functions. First, it allows to increase the absorption surface in the villi, and it shields the stem cells from the biological or physical dangers within the lumen. In the lab we have previously reported that using a photolithography-based technique we can successfully fabricate PEGDA-AA hydrogels with villus-like microstructures. In the first section of this thesis, we aimed at better mimicking the native topography of the small intestinal epithelium by engineering an *in vitro* model containing crypt-like structures. First, we showed how, by adapting the photolithography-based fabrication procedure (employing photomasks with black circular windows and optimising the light exposure time), we could obtain PEGDA-based hydrogels with crypt-like cavities. The photomasks with the smallest windows (50 μm) yielded microstructured hydrogels with cavities dimensions (depth of 209 μm, and bottom diameter of 58 μm) in the range of those reported for intestinal crypts (60[123] – 100 μm[124] in depth, 44 μm in bottom

diameter). This result points out to photolithography-based polymerization as a simple, versatile yet robust technique to fabricate microstructured hydrogels. However, further characterization revealed the presence of partially-crosslinked polymer inside the cavities. This was most likely due to the nature of the chemical reaction employed (free radical polymerization and acrylate-based) and light scattering, which extended the reaction to the theoretically non-illuminated regions, thus inducing some degree of polymer crosslinking in the cavities. In contrast, thiol-ene chemistry is less sensitive to oxygen inhibition and the polymer is crosslinked via a step-growth mechanism, resulting in more homogeneous networks[125]. Other alternative methods are the use of replica moulding[65,66], shorter polymer chains and/or hydrogels with high polymer content[70]. Indeed, they obtain empty crypts but at the cost of compromising mechanical properties[66] or hydrogel porosity[70]. To try to overcome this limitation inherent to the fabrication technology employed and the prepolymer solution used while maintaining both the mechanical properties and the mesh size, we again adapted the fabrication protocol to obtain larger crypt features. For that, we designed new photomasks with larger crypts and we reoptimized light exposure times. Upon hydrogel functionalization with collagen I, we observed a faint signal suspended across the cavities. This signal corresponding to collagen I most likely coincided with partially-crosslinked material still present in the cavities. Because the crypts were larger and deeper, the amount of partially-crosslinked polymer did not completely cover the cavities, which allowed the coupled protein to reach deeper.

Next, we seeded organoid-derived cells on top of PEGDA-based hydrogels with crypts of 150, 250 and 300 μm in diameter. Interestingly, we observed the formation of epithelial monolayers on the three kinds of crypt-like hydrogels tested. However, in the hydrogels with crypts of 250 and 300 μm in diameter, the monolayer was discontinued in the cavities, coinciding with the protein pattern. Conversely, in the 150 μm crypts, a fully covering epithelium monolayer could be obtained, although it could not be maintained for longer than three days. We reasoned this might be due to collagen I protein floating between flat regions rather than following the outline of the crypts, thus making both the links between collagen I – hydrogel and cells – collagen I very fragile. Altogether, these results suggest that, although the photolithography-based technique employed to fabricate villus-like protruding structures yielded hydrogels with seemingly well-defined edges, the same technique does not seem to be the optimal to obtain completely hollow structures. We observed that increasing crypt size could (i) facilitate the entrance of PBS in these larger features and removing a greater part of the partially crosslinked material and/or (ii) modify the dynamics of the polymerization reaction leading to better crypts. However, even though free-radical polymerization is an attractive chemistry to crosslink hydrogels because of its speed and simplicity, the fact that the reaction continues as long as there are reactive groups and photoinitiator left to react makes it difficult to control

and to confine in space and time. Collagen I hydrogels containing crypt-like (and villus-like) structures have been fabricated through replica moulding[66,67]. The use of collagen I -a natural material containing inherent cell adhesion cues- as scaffolding material allowed to directly culture cells without the need to previously functionalize the scaffold. However, in the study by Verhulsel et al[66], the crypt-like structures obtained did not faithfully mimic the native cavities as they did not have the desired aspect ratio, possibly because of the degradation of the hydrogel. In the work by Wang et al 2017b, the crypt-like structures had dimensions (approximately 120 μm in depth and 50 um in diameter) very similar to those reported *in vivo* (between 60 and 100 um in depth)[123,124] However, both studies employed the replica moulding technique, which requires numerous and complicated steps before obtaining the final hydrogel scaffold. The work presented in the first section of this thesis suggests that light-based fabrication techniques could pose as a valid alternative if the crosslinking reaction could be better confined, by, for instance, employing a technique different than acrylate-based such as thiol-ene chemical reactions.

The particular crypt-villus architecture of the intestinal epithelium has another fundamental function: to provide a physical scaffolding for biochemical gradients to be formed and maintained[100]. Gradients of Wnt, BMP and EGF signalling pathways have been proven to play a key role in the tissue organization and homeostasis by driving the maintenance of the intestinal stem cells (ISCs) at the crypts and their ordered differentiation along the villus axis. However, intestinal organoids and 2D derived monolayers lacking the tissue topography are still able to self-organize into crypt and villus-like regions[7,53,59,60], thus underlining the capacity of epithelial-derived gradients, mainly orchestrated by Paneth cells[2,126,127] to organize the tissue, and apparently limiting the prominent role of architecture in the formation and maintenance of gradients. Therefore, the decoupling of the intestinal geometry from the biochemical gradients present within is not straightforward and it remains as an open challenge. Since, *in vivo* biomolecular gradients are spatially patterned through the crypt-villus axis, *in vitro* models should provide a crosstalk between the architectural cues and the biomolecular gradients to induce tissue patterning and thus be physiologically relevant. To achieve this, we have used a photolithography-based approach to produce 3D villus-like PEGDA-AA hydrogels[69] to provide organoid-derived epithelial cells with topographical cues with well-controlled biochemical gradients. First, we demonstrated how we could fabricate low macromolecular content PEGDA-AA hydrogels (soft and highly porous) with high aspect ratio microstructures resembling intestinal villi. Similar villus-like structures have been previously achieved by replica moulding or 3D bioprinting[65,66,70]. These techniques often require multiple steps or are time-consuming. On the contrary, we used a fast single-step approach that overcomes those limitations. Moreover, the resulting hydrogels also offered elasticity values in the range of those reported for the intestine[49]. Matrix stiffness has been shown to impact cell

behaviour in numerous biological contexts such as differentiation lineage of mesenchymal stem cells[128,129]. Specifically in the intestine, a clear example of the relevance of matrix elasticity is the standard model used to perform drug absorption and permeability tests during preclinical trials. Caco-2 cells grown on hard polycarbonate membranes displayed transepithelial electrical resistance (TEER) values much higher than when seeded on soft hydrogels[74]. Yet, because of the carcinogenic nature of Caco-2 cells, TEER values still appeared greater than those reported for the small intestine[130]. Instead, organoid-derived primary epithelial cells cultured on Transwell inserts for 21 days displayed TEER values in the range of the native tissue[60]. Here, we went one step further and we cultured organoid-derived epithelial cells on soft hydrogels, thus retrieving the biological properties of the intestinal epithelial cells and the mechanical ones of the tissue. To the best of our knowledge, the developed 3D platform presented in the second section of this thesis is the only one purely based on a synthetic hydrogel that allows the culture of organoid-derived cells. The use of a synthetic hydrogel yielded a very regular mesh size where protein diffusion can be easily studied. Using this property, we could predict the size of our polymer network and we established it was sufficient to allow the diffusion of factors of the ISC niche, Moreover, our set-up was compatible with Light Sheet Florescence Microscopy (LSFM), thus providing access to the diffusion dynamics of the gradients' profiles in real time. This revealed that the gradients we generated were stable over time, confirming the suitability of the developed platform to deliver ISC niche biomolecules in a spatially-relevant manner for prolonged time periods.

Most studies generating biochemical gradients have mainly relied on microfluidic platforms[131], thus increasing the complexity of the experimental set-up[132]. To be able to establish gradients in a simple yet effective manner, here we have mounted our hydrogels onto standard Transwell inserts, as they provide two separate basolateral and apical compartments allowing the use of two different cell culture media and therefore, the possibility to generate biochemical gradients through free diffusion in a straightforward fashion, while being compatible with the most standardized cell culture procedures. We observed how the formation of a complete monolayer did not depend on the presence or absence of gradients, but, in the case of *Uniform* condition, monolayers reached 100% surface coverage in less time. We speculate that this might be due to the greater availability of stem cell niche factors in the *Uniform* condition as ISC niche factors are not only delivered basolaterally but also apically. Then, we found that in the presence of gradients (*Asymmetric* condition), stem and proliferative cells localized predominantly to the base region, closer to the source of the ISC niche factors, and the differentiated population (mean signal of CK20 and frequency of FABP1$^+$ enterocytes) were mainly located at the villus tip. In contrast, there was no significant difference in the frequency of proliferative and stem cells between the base and the tip of the villi nor preferred location for the differentiated

population in the *Uniform* condition. Tissue topography alone is thought to guide epithelial cellular compartmentalization by shaping the epithelium-derived gradients[100]. For instance, scaffolds with crypt-like structures (diameter = 50-100 μm, height = 130-170 μm)[65,68,133] were shown to enable the patterning of the crypt-like domains in the absence of exogenously controlled biomolecular gradients, presumably due to the reasons given above. Our results suggest that, in the absence of crypts, the establishment of gradients of ISC niche biomolecules in the villus-like PEGDA-based hydrogels induced an *in vivo*-like epithelial cell compartmentalization. This implies that architectural cues and gradients of factors coming from non-epithelial origin can act synergistically. Indeed, the lack of the physical presence of primary fibroblasts in the model impedes the study of their physical crosstalk with the epithelium. However, at the same time, this allows the control over the concentrations of each individual factor and the possibility to correlate the concentration or the gradient profiles of relevant factors to the cellular response observed. Precisely, using our platform, we showed that when we modified the gradient profiles by increasing concentrations or by adding new factors like Wnt2b, we no longer obtained cell compartmentalization. We reason that this loss of compartmentalization might be due to the higher concentrations that cells were receiving, as the gradients of ISC niche factors, which are only active in the crypt compartment *in vivo*[134], were possibly spanning the entire vertical axis of the scaffolds. Currently, there is no knowledge of the individual contributions of each of the factors secreted by the fibroblasts. In this context, the platform developed in the second section of this thesis could be used to pinpoint which are the essential ISC niche factors and their optimal source concentrations that are needed to obtain *in vivo*-like tissue compartmentalization.

As described previously, gradients formed by biochemical factors such as Noggin and Gremlin[31], R-Spondins[30] and Wnt2b[8] secreted by intestinal fibroblasts underneath the epithelium are needed for ISC maintenance and differentiation and thus, need to be considered when engineering more physiologically relevant intestinal epithelium platforms. In this context, the first half of this thesis aimed to include, in a spatio-relevant manner, the paracrine signalling of intestinal fibroblasts in an *in vitro* model of the intestinal epithelium. Yet, in other biological scenarios, mostly pathological ones such as cancer or wound healing in skin, fibroblasts have been described to have a physical crosstalk with epithelial cells. Here, considering also that intestinal fibroblasts are right underneath the epithelium, we hypothesize that their physical presence, and not only their paracrine signalling, might be pivotal even under non-pathological conditions. Therefore, in the second half of this thesis we aimed at physically including the mesenchymal compartment in the intestinal models. First, by addressing their role in epithelial migration and, second by building a three-dimensional intestinal model with *in vivo*-like architecture and cell composition.

To address the first point, we have developed a 2D coculture *in vitro* model employing organoid-derived epithelial cells and primary fibroblasts isolated from mouse lamina propria to study epithelial migration. First, we characterized the isolated mesenchymal cells from lamina propria to elucidate if the obtained cell populations were comparable to those reported to exist *in vivo*. For that, we performed scRNAseq and we obtained four main groups, a first one accounting for 1% of the total population expressing Pecam1, classified as endothelial cells[135–138], a second representing the 2% expressing Gap43, identified as neurons[139,140] and glial cells[141], a third one encompassing 10% of the cells expressing Cd52, categorised as immune cells[142], and a fourth comprising 75% of the total cells expressing Vimentin but not the markers mentioned above, which could be categorised as fibroblasts[33,118]. These results suggest that the isolation protocol followed, and, more importantly, the succeeding cell culture, resulted in the identification of the four main cell populations reported to be present in the native intestinal mucosa[32,33,111]. Next, we analysed the expression of factors involved in Wnt and BMP signalling within the fibroblast group, and we found different subpopulations that we could quite faithfully annotate as telocytes (expressing Wnt4, Wnt5a, Dkk3, Sfrp1, Bmp4 and Bmp5), a first group of PDGFRA^{low} cells (expressing Wnt2b, Rspo3 and Chrd (BMP antagonist)), a second group of PDGFRA^{low} cells (expressing Grem1, Grem2, Bmp1 and Dkk2), and two last groups of pericytes that were marked by their no expression of any of the relevant factors of the ISC niche[33]. Compared to previous studies characterizing the mesenchymal cells of the mouse small intestinal stroma[32,33], we opted to not identify any subpopulation as "trophocytes", reported to be marked by the high expression of Rspo3 and Grem1, together with other Rspo, Dkks and Bmp4. In our opinion, this population and the PDGFRA^{low} cells are difficult to distinguish, as both are marked by their expression of low levels of PDGFRA and high expression of Grem1, among others. As for the other subpopulations we identified, they were mainly marked by the expression of the same factors, thus suggesting consistency with the different studies reported[32,33,111]. Still, it is worth mentioning that the field of intestinal fibroblasts subpopulations has been frequently subjected to debate and controversy. First, because there are no markers that are restrictive to one subpopulation (for instance, Acta2 is expressed by myocytes, telocytes and pericytes) and no factors are expressed by only one subpopulation (for instance, Dkk3 is expressed by telocytes, trophocytes, myocytes and PDGFRA^{low} cells), the distinction between one type of fibroblast and another has been challenging[32,33]. Moreover, the location of each kind is not very precise either, frequently we can find different kinds physically adjacent one to another[33], arising the reasonable doubt of redundancy. Finally, it is also at least puzzling the fact that, within one population, there is expression of proliferative promoting factors and differentiation promoting factors. However, it remains to be deciphered whether this is because there is fine tuning of the expression of different factors in the temporal scale, or in the spatial scale. Taking all this into account and to

have the broadest representation from the intestinal stroma, we decided to use the unfractioned mesenchyme to study its impact on the migration of epithelial cells. To do so, we first cultured organoids and primary fibroblasts in 3D Matrigel drops. After 2 days in culture, we observed that when crypts were cultured in *+ fibr. cond med.* or in *+ fibroblasts* conditions, that is to say, in the presence of the paracrine signalling from the primary fibroblasts, they were forming cystic structures without budding units.

Similar cysts have been previously reported[2,8,28,30] upon the culture of wild type organoids in the presence of Wnt3a, a proliferation promoting factor secreted by Paneth cells that constitutes the stem cell niche. Later, it was found out that non-epithelial cells were also producing Wnt agonists such as Wnt2b that indeed induced this morphological change from budding organoids into cysts[8]. Thus, historically, this cystic morphology in organoids was linked to a boost of proliferation caused by Wnt activation. Since the scRNAseq analysis revealed a significantly high expression of Wnt2b (together with other factors) in the isolated primary fibroblasts, we first hypothesized that this factor (and possibly others inducing proliferation such as Rspo3) was involved in inducing this cystic morphology in the crypts. However, when we immunostained for Ki67 crypts grown in *control* condition and we compared them with crypts grown in *fibr. cond. med.* condition, we did not observe an increase in the percentage of cells positive for Ki67 in the *fibr. cond.* Indeed, careful review of the studies reporting the morphological transformation of organoids into cysts upon culture with Wnt factors or with fibroblasts has unmasked a rather weak link to an increase in proliferation. First, none of the studies claiming this association has actually quantified nor compared the number of proliferative cells in normal organoids versus cystic organoids and, what's more, they all based their conclusion on the visual, at least biased, consideration of higher intensity signal of lacZ on Axin2-lacZ (reporting stem cells) derived organoids cultured with medium supplemented with Wnt3a compared to those cultured with ENR medium. Moreover, in a very recent study, analysis of 5-etinil-2'-desoxiuridina (EdU) (a thymidine analogue nucleoside that gets incorporated into the DNA during cell division) uptake from organoids cultured with EN vs organoids cultured with intestinal fibroblasts unveiled a much lower division rate in organoids cultured with the mesenchymal cells[112]. In this same study, they quantified the relative transcript levels of stem cell markers and they found that organoids cultured with the mesenchymal cells had significantly lower numbers. Finally, culture of organoids with BMP recombinant factors that promote differentiation resulted in very similar outcomes in all analysis: organoid cystic morphology, few EdU uptake and low transcript levels of stem cell markers[112]. Taking all these studies into account, together with the expression of both proliferation and differentiation promoting factors by our population of primary fibroblasts as revealed by scRNAseq, we believe that the cystic morphology observed in our cell cultures with *+ fibr. cond. med* or *+ fibroblasts* and possibly, that observed in

other studies, cannot be faithfully attributed to an increase in Wnt signalling that translates into cell proliferation. Instead, we speculate that this transition from budding organoids into spherical structures is due to a nonlocalized activation of different signalling pathways, for sure including Wnt, but also possibly involving BMP.

Next, we observed that, compared to *fibr. cond. med.*, in the *+ fibroblasts*, cysts were visibly deformed. Instead of being rather spherical, they had peaks that coincided with where the fibroblasts were physically interacting with the cysts. In later stages, we observed how, from the 3D cysts, tongues of 2D epithelial monolayers sprouted. Conversely, organoids cultured without the physical presence of fibroblasts never underwent this 3D to 2D transition. This implies that fibroblasts enabled this transition, for which epithelial migration was required. Actually, in pathological conditions such as cancer, cancer associated fibroblasts (CAFs) have been described to physically interact with epithelial tumours, pulling from epithelial cells to lead their migration and thus invasion[143]. To the best of our knowledge, this type of physical crosstalk has not been described in physiological conditions excepting during development. Thus, we wanted to further study this role of fibroblasts in epithelial migration in homeostatic conditions using a 2D *in vitro* model where migration was studied upon the generation of a cell-free area, rather than scratching as performed in the typical wound healing assay. When organoid-derived epithelial cells were cultured with ENRCV medium (*control*), we observed that cells were not able to close the gap. Instead, in the presence of primary fibroblasts_CM/ENRCV medium, the same cells were now able to close a much larger fraction of the gap. In the same amount of time but in the presence of actual primary fibroblasts, epithelial cells fully closed the gap. A closer look unmasked the appearance of holes within the monolayer upon migration in all three conditions. Intriguingly, they generally emerged next to cells with larger area, which usually coincides with differentiated cells[88]. Beguilingly, in a very recent report employing MDCK monolayers[144], the appearance of holes was correlated with cell division or by cell-stretching events, a phenomenon that could be occurring in our setup given that holes typically emerged next to large cells. After some time, both in *+ fibr. cond. med* and *+ fibroblasts*, epithelial cells were able to close the hole, thus restoring tissue integrity. Instead, in *control* condition, although cells extended many and large protrusions, these were seemingly not sufficient for holes to close. Holes in *control* condition were more regular and with well-defined edges and they seemed to be under higher tension and thus to confine epithelial cells, which looked quite columnar shaped. Instead, holes in the other two conditions had more irregular shapes and did not confine the cells as much. Intriguingly, in a very recent report employing MDCK monolayers[144], the appearance of holes was linked to monolayers being under tension (rather than shear). This result suggest that epithelial cells cultured with fibroblasts' secreted factors *(+ fibr. cond. med* and *+ fibroblasts* conditions) might be under less tension,

hypothetically because their cell-ECM adhesions are stronger. However, in the study by Sonam et al[144], a threshold area was found above which holes could not close. In our experiments, we have not observed such transition, but we have observed a greater tendency of smaller holes to close than of bigger holes. On the other hand, both in *+ fibr. cond. med* and *+ fibroblasts* we could find epithelial cells displaying a spindle shape, more fibroblast-like, a morphology that, theoretically, allows cells to be more motile. This might explain why in *+ fibr. cond. med* and *+ fibroblasts* conditions, cells were able to close the holes.

When we immunostained samples with Ki67 to elucidate if the ability to fully close the gap was due to differences in cell proliferation, we obtained the same percentage of $Ki67^+$ cells in all the conditions analysed, thus discarding any main role of cell proliferation in epithelial migration. These results go in line with the cell proliferation results obtained in the 3D cultures of crypts with ENRCV medium vs primary fibroblasts_CM medium, in which we observed no apparent differences, and with the results obtained from the scRNAseq, in which fibroblasts were seen to be expressing both proliferation and differentiation promoting factors. Although it would have been elegant to confirm that in our setup, blocking of the proliferation does also not impact cell migration, it would have been technically impossible to inhibit the proliferation of epithelial cells but not of mesenchymal cells in the *+ fibroblasts* condition. On the other hand, what we did observe was that, regardless of the condition, the percentage of proliferative cells was higher in the migration front than in the monolayer. Analysis of the localization of different cell types upon wound healing in skin *in vitro* models revealed 3 differential regions: the wound edge populated by leader cells which are non-proliferative, a central region composed mainly of proliferative cells (thus called proliferative hub), and an innermost region where differentiated cells localize[145]. Conversely, in our experiments, we do not observe such segregation. In another *in vitro* study using Madin-Darby canine kidney (MDCK) epithelial cells, a sudden increase in cell proliferation was detected 12 h after starting the wound assay, when wounds had already completely closed[146]. Interestingly, treatment with mitomycin C, a drug that completely blocks cell proliferation, did not impact on the rate of wound closure. Therefore, in this setup, cell proliferation is thought to act as a mechanism to replace dead cells rather than as a cell migration driving factor. Conversely, in two other studies, proliferative cells were localized at the wound edge right after damage, when no significant cell migration had been initiated yet[147,148]. However, in our experiments, proliferative regions are detected already before initiating the migration assay, discarding the possibility that cell proliferation is acting simply as a dead cells' replacement mechanism, and during migration (at 24h, exactly halfway to complete gap closure), discarding the possibility that cell proliferation is acting simply as an activating migration event. It is worth discussing that the abovementioned studies are based on the analysis of cell migration upon typical wound scratching, whereas the setup presented here allows to investigate cell

migration decoupled from cell damage, that is to say, in homeostatic conditions. Still, in an also free surface-based study but employing MDCK cells, cell divisions were localized within the initial monolayer covered region rather than localizing at the migration front[149]. Therefore, in the system presented here, we speculate that, upon barrier removal, proliferative cells at the migration front can and use the free space to grow in size, whereas the proliferative cells within the monolayer are confined and cannot expand. With increasing culture time, this results in proliferative cells localised at the migration front occupying a larger surface than those at the monolayer. Therefore, in a given area, there are less cells in the migration front than in the monolayer. When quantifying cells in this area, this may yield a higher percentage of $Ki67^+$ cells in the migration front than in the monolayer. We also observed how the closer to the front cells are, the more distance they travel (both total distance and net displacement, data not shown). We speculate that this might be due to a higher motility of proliferative cells compared to differentiated cells. To test this speculation, one could compare the migration capabilities of a monolayer of only differentiated cells (by sorting them for FABP1, for instance) with that composed of proliferative cells (by sorting them for Ki67, for instance). The analysis of the individual cell trajectories was in accordance with the gap closure results, meaning that, in the *control* condition, cells moved in all directions, whereas in the *+ fibr. cond. med.*, they tended to go towards the gap, a preference that was highly accentuated in the *+ fibroblasts* condition. These results suggested a potential physical role of fibroblasts in the migration of epithelial cells. To elucidate this, we analysed the migration videos using PIV and, to our surprise, not only did we identify a region migrating towards the gap, corresponding to epithelial cells, but also another region migrating towards the monolayer, corresponding to fibroblasts. In other words, while epithelial cells were migrating to close the gap, fibroblasts were migrating towards the monolayer, both movements aligned in the x axis, as no significant contribution was found in the y component of velocity. Based on these observations, it seems that the most efficient epithelial migration requires not only the motility of epithelial cells but also that of fibroblasts, thus confirming a clear physical role of fibroblasts in homeostatic epithelial migration. Analysis of fibroblasts' orientation revealed that they were preferentially aligned with the migration direction. Intriguingly, fibroblasts located in the central regions of the gap, far from the monolayer edges, were equally aligned. This phenomenon, called long-range ordering, has been described mainly in the context of tumour microenvironment[150]. Interestingly, when fibroblasts align circumferentially respect to the tumour mass, this often leads to tumour confinement, whereas when they align perpendicularly, it leads to cell migration (as we observe in our experiments) and eventually tumour invasion. Because a similar ordering can be observed in the underlying collagen fibbers of tumours[115,151], we assessed, (i) if there was relevant expression of typical ECM proteins in the *+ fibroblasts* condition and (ii) if they were disposed in any particular fashion. Indeed, we observed fibbers of collagen IV, laminin, and fibronectin, aligned with the

migration direction, as fibroblasts themselves. These results suggest that, not only fibroblasts migrate towards the wound, but while doing so, they secrete ECM proteins, resulting in patterns of aligned fibbers in the migration direction. In the same way it has been described in cancer metastasis, we speculate these patterns of ECM fibbers might be used for epithelial cells to migrate, and to do it in an oriented and thus efficient manner. All in all, the 2D coculture *in vitro* system devised in the third part of this thesis has allowed to unveil for the first time, a physical role of fibroblasts in the migration of intestinal epithelial cells in a physiological context. Still, whether this crosstalk occurs *in vivo* is still to be investigated.

Precisely because we have observed that intestinal fibroblasts not only have an impact on epithelial cells through their secreted factors but also through direct interaction, in the fourth part of this thesis we attempted to engineer an *in vitro* model that, not only recapitulated the native architecture, as we did in the first part of the thesis, but that it also incorporated the physical presence of fibroblasts, as we did in the third section. Since AA is cytotoxic, we had to find an alternative hydrogel for the engineering of this new platform. Previously in the lab, it was demonstrated that co-networks of GelMA and PEGDA can be a good compromise between inherent cell adhesion motives and robustness to allow cell embedding[74]. To fabricate GelMA-PEGDA hydrogels, in the lab we customised a DLP-based bioprinter able to crosslink the polymers using visible light. GelMA-PEGDA hydrogels of low macromolecular content fabricated with this technology were found to have native-like stiffness (GelMA-PEGDA hydrogels ≈ 6 kPa, small intestine ≈ 14 – 22 kPa[49]), a highly desirable feature to suitably mimic physiological conditions. Techniques such as extrusion-based bioprinting impose a considerable degree of shear stress on the cells, resulting in poor cell viability results. Instead, we found that using our customised DLP-based bioprinter, the majority of embedded NIH/3T3 fibroblasts were viable right after printing. Moreover, life/dead assay at day 7 yielded the same percentage of viable cells, suggesting that the chosen hydrogel allows gas exchange and nutrient transport for cells to grow within. The fabricated GelMA-PEGDA hydrogels also sustained cell division, as seen by the immunostainings of Ki67 between days 4 and 11 after printing. Surface coverage analysis of 2D projected images of the hydrogels and posterior orthogonal histological cuts unveiled the accumulation and spreading of cells at the surface of the hydrogel, reaching almost 100% surface coverage at day 11 after printing, together with a reduction of cells in the bulk. *In vivo*, most cells are at maximum of 200 mm from the nearest capillary, the source of nutrients and oxygen[152]. Given that our hydrogels are thicker than 200 mm, we hypothesize that the limited diffusion of nutrients and specially oxygen through the thickness of the hydrogel might induce the formation of gradients and thus, the migration of cells towards the surface and their accumulation in that region. This phenomenon was also observed in the 3D villus-like GelMA-PEGDA hydrogels, as we observed how, over time, fibroblasts

accumulated at the outline of the hydrogels, that is to say, at the cell culture medium-hydrogel interface. However, in the 3D hydrogels, we also observed a much higher fraction of cells at the tip of the pillars than at the base, a behaviour we cannot solely ascribe to nutrients and oxygen diffusion. Recent evidence has shown that cells can respond to various physical cues in their environments including the local geometry, and in particular, curvature[120]. However, the scale of curvatures reported to impact on cell distribution is much smaller than those offered by the engineered villus-like GelMA-PEGDA hydrogels presented here. Further experiments analysing the distribution of cells within microstructured hydrogels with convexities and concavities of the same curvature would be needed to assuredly rule out substrate curvature as a driving force for the heterogeneous cell distribution observed. Nevertheless, it should also be noted that, while the reported studies have analysed the migratory patterns of cells seeded on substrates[120,153–155], in our case, cells are within the substrates and therefore, do not sense curvature until they reach the hydrogel surface.

Next, we proceeded to culture organoid-derived epithelial cells on top of the fibroblast-laden villus-like GelMA-PEGDA hydrogels. In particular, we wanted to study if this asymmetric distribution of fibroblasts within the villus-like microstructures had an impact on how organoid-derived cells grew. Throughout the culture, we observed that epithelial cells grew foremost at the tip and at the base of the microstructures. We attribute these preferred locations for epithelial cells to grow to basic sedimentation induced by gravity upon seeding. However, we speculate that their growth at the tips might also be influenced by the larger fraction of fibroblasts found in that region. Maintaining the cultures for longer periods of time did not result in epithelial patches covering a larger surface and, what's more, they started to form multilayers and to have more roundish rather than columnar shape. In parallel, at initial stages fibroblasts preferentially positioned right underneath the epithelial cells, suggesting that they support epithelial growth, as seen in flat hydrogels of GelMA-PEGDA. This also goes in line with the results obtained in section 4.2, where fibroblasts were seen indispensable to maintain epithelial integrity and to enable an efficient epithelial migration Later, when there were more fibroblasts in the hydrogel surface, there were still more quantity underneath the epithelium but there were also fibroblasts in regions without epithelium. Surprisingly though, those fibroblasts underneath were more spread and aligned with the outline of the hydrogel. Indeed, analysis of the elongation index of fibroblasts' nuclei showed that when cocultured with epithelial cells, their nuclei was significantly more elongated than when cultured alone. We speculate that the tractions epithelial cells can be exerting on the substrate might get conveyed to the fibroblasts, thus receiving a mechanical stress, which results into the deformation of the nucleus. However, the fibroblasts that are not in direct contact with epithelial cells, forming part of innermost layers, are equally elongated. One possible explanation for this can be that the tractions exerted by

epithelial cells are inducing a mechanical stress on the hydrogel, and this, in turn, is being transferred to the fibroblasts beneath. Another possible scenario would be that the epithelial cells directly mechanically stress the fibroblasts, and these, in turn, transfer this stress to the underlying fibroblasts. Overall, these results seem to suggest again a clear direct interaction between epithelial cells and fibroblasts and that this is required for epithelial growth. In other *in vitro* studies, the presence of fibroblasts was seen to enhance the barrier properties of the epithelial monolayers[74] or to favour *in vivo*-like epithelial compartmentalization[66]. However, to our knowledge, in no *in vitro* platform, fibroblasts have been reported to have such a strong effect as to allow the growth of epithelial cells, otherwise not possible. We attribute this radical effect to, the use of very soft hydrogels which might enable weaker cell adhesions, and the use of organoid-derived epithelial cells, which might be more sensitive to matrix elasticity than cell lines like Caco-2. In this way, the embedding of fibroblasts into the hydrogels seems to allow stronger cell adhesions and thus, successful epithelial growth.

In sum, in the fourth section of this thesis, we have developed a villus-like GelMA-PEGDA hydrogel that allows to include NIH/3T3 stromal fibroblasts mimicking the lamina propria compartment, and the culture of organoid-derived cells on top. Through this *in vitro* model, we exemplify the importance of engineering platforms that mimic not only the epithelial compartment but also the stromal one, as seen by the inability of organoid-derived cells to grow in the absence of fibroblasts.

6. Conclusions

- An in-house developed photolithography-based technique successfully used to fabricate PEGDA-AA hydrogels with villus-like microstructures was adapted to also produce crypt-like microstructures. However, the free-radical polymerization reaction yielded partially-crosslinked polymer trapped in the cavities, which, in turn, impeded a proper protein functionalization of the hydrogel. Still, organoid-derived monolayers could be grown on these collagen I-functionalized crypt-like hydrogels.

- The fabricated 3D villus-like PEGDA-AA hydrogels have anatomical dimensions, native tissue-like elasticity and a mesh size that allowed the diffusion of the factors of the ISC niche. Steady-state biochemical gradients could be formed along the villus vertical axis within the PEGDA-based hydrogels. Through an *in silico* model developed in the lab, we were able to fit well the experimental diffusion data and thus to predict the gradients of the molecules of the intestinal stem cell niche (ISC) secreted mainly by fibroblasts. Upon collagen I functionalization, organoid-derived single cells could make a complete monolayer within three days after seeding. The presence of gradients of the ISC niche, as opposed to the uniform administration of the same factors, resulted in proliferative and stem cells preferentially located at the bases of the hydrogels, and differentiated cells at the tips of the villus-like microstructures. The culture of organoid-derived single cells under different kind of gradients affected their growth dynamics: at initial stages, the proliferative population was greater, but later, it was less than the basic gradients condition. Moreover, under these conditions, monolayers reached 100% surface coverage in less time. Overall, a novel 3D villus-like hydrogel platform with organoid-derived cells cultured under biochemical gradients of ISC niche was developed.

- The isolated stromal cells from the intestinal lamina propria consisted mainly of fibroblasts, as revealed by the analysis of the scRNAseq. Manual cell annotation evaluating the expression of proliferation and differentiation promoting factors unveiled the existence of most of the subtypes of fibroblasts described to exist in the intestinal lamina propria (telocytes, $PDGRA^{low}$ cells and pericytes). After the detailed characterization of the stromal population (henceforth called primary fibroblasts), we studied their impact on epithelial cells by coculturing intestinal organoids with the primary fibroblasts. The culture of organoids with the paracrine signalling from the intestinal fibroblasts induced their morphological change into cysts. Fibroblasts cocultured with organoids made physical contact and led their spreading until forming 2D monolayers. Upon the observation of this physical crosstalk, a spatio-physiologically relevant *in*

vitro model was devised to study the role of fibroblasts in epithelial migration through the formation of cell-free areas. Epithelial cells alone could not efficiently migrate nor restore the integrity of the monolayer. Instead, when cultured with the paracrine signalling from fibroblasts or, even more, when cocultured with the actual fibroblasts, they migrated directionally and were able to completely close the gap. While epithelial cells were migrating towards the gap, fibroblasts were found to migrate towards the monolayer and to be perpendicularly disposed to the migration front. During this process, fibroblasts also secreted proteins of the ECM that were also aligned perpendicular to the migration front. In sum, primary intestinal fibroblasts were found to be fundamental for efficient epithelial cell migration in a devised *in vitro* model.

- An in-house DLP-based bioprinter allowed to fabricate flat or villus-like GelMA-PEGDA hydrogels with native tissue-like mechanical properties. NIH/3T3 fibroblasts could live, grow and maintain their proliferative capacity for at least seven days while embedded in flat hydrogels. With culture time, they tended to migrate towards the surface. Organoid-derived cells seeded on flat cell-free GelMA-PEGDA hydrogels were not able to attach nor grow. Instead, on fibroblast-laden flat hydrogels, they could attach and form a monolayer that covered almost 80% of the surface, suggesting that, in this model, fibroblasts are required for epithelial growth. Time-lapse movies showed how the two cell types physically interact. Epithelial cells first formed clusters surrounded by radially disposed fibroblasts, which triggered the emergence of tongues of epithelial cells, leading to their expansion. Over time, epithelial monolayers covered most of the hydrogel surface while fibroblasts had an isotropic orientation. The organoid-derived monolayers on top of the fibroblasts-laden GelMA-PEGDA hydrogels had an *in vivo*-like disposition as seen by the presence of crypt-like regions containing proliferative and stem cells. When fibroblasts were embedded in villus-like GelMA-PEGDA hydrogels, they migrated towards the hydrogel-cell culture medium interface, as seen in flat hydrogels, but they also showed a slight preference for the tips. Organoid-derived cells could grow on fibroblast-laden villus-like hydrogels, although they did not cover the whole surface. In these cocultures, fibroblasts tended to accumulate in the regions where there were epithelial cells. Moreover, their nuclei seemed more elongated and aligned with the outline of the hydrogel. Indeed, fibroblasts without epithelial cells on top exhibited a significantly less elongated nucleus than fibroblasts cultured with epithelial cells on top. All in all, a 3D villus-like hydrogel *in vitro* model with embedded fibroblasts and organoid-derived epithelial cells on top was engineered. This platform unveiled the requirement of the presence of fibroblasts for epithelial cells to grow.

7. References

1. Tortora GJ, Derrickson B. *Principles of Anatomy and Physiology*. Vol 53.; 2008.

2. Sato T, Van Es JH, Snippert HJ, et al. Paneth cells constitute the niche for Lgr5 stem cells in intestinal crypts. *Nature*. 2011;469(7330):415-418. doi:10.1038/nature09637

3. Parker A, Maclaren OJ, Fletcher AG, et al. Cell proliferation within small intestinal crypts is the principal driving force for cell migration on villi. *FASEB J*. 2017;31(2):636-649. doi:10.1096/fj.201601002

4. Kaur P, Potten CS. Cell migration velocities in the crypts of the small intestine after cytotoxic insult are not dependent on mitotic activity. *Cell Tissue Kinet*. 1986;19(6):601-610. doi:10.1111/j.1365-2184.1986.tb00761.x

5. Wright NA, Alison M. *The Biology of Epithelial Cell Populations*. Clarendon Press ; Oxford University Press; 1984.

6. Krndija D, El Marjou F, Guirao B, et al. Active cell migration is critical for steady-state epithelial turnover in the gut. 2019;710(August):705-710.

7. Pérez-González C, Ceada G, Greco F, et al. Mechanical Compartmentalization of the Intestinal Organoid Enables Crypt Folding and Collective Cell Migration. *Nat Cell Bio.* 2021. doi:10.1038/s41556-021-00699-6

8. Farin HF, Van Es JH, Clevers H. Redundant sources of Wnt regulate intestinal stem cells and promote formation of paneth cells. *Gastroenterology*. 2012;143(6):1518-1529.e7. doi:10.1053/j.gastro.2012.08.031

9. Gregorieff A, Pinto D, Begthel H, Destrée O, Kielman M, Clevers H. Expression Pattern of Wnt Signaling Components in the Adult Intestine. *Gastroenterology*. 2005;129(2):626-638. doi:10.1053/j.gastro.2005.06.007

10. Haramis A-PG, Begthel H, Born M van den, et al. De novo crypt formation and juvenile polyposis on BMP inhibition in mouse intestine. *Science*. 2004;304(5676):1449. doi:10.1126/science.304.5676.1449

11. Biteau B, Jasper H. EGF signaling regulates the proliferation of intestinal stem cells in Drosophila. *Development*. 2011;138(6):1045-1055. doi:10.1242/dev.056671

12. Amit I, Citri A, Shay T, et al. A module of negative feedback regulators defines growth factor signaling. *Nat Genet*. 2007;39(4):503-512. doi:10.1038/ng1987

13. Grant S, Qiao L, Dent P. Roles of ERBB family receptor tyrosine kinases, and downstream signaling pathways, in the control of cell growth and surival.

Front Biosci. 2002;(12):376-389.

14. Olayioye MA. Update on HER-2 as a target for cancer therapy Intracellular signaling pathways of ErbB2/HER-2 and family members. *Breast Cancer Res*. 2001;3(6):385-389. doi:10.1186/bcr327

15. Fre S, Huyghe M, Mourikis P, Robine S, Louvard D, Artavanis-Tsakonas S. Notch signals control the fate of immature progenitor cells in the intestine. *Nature*. 2005;435(7044):964-968. doi:10.1038/nature03589

16. Batlle E, Henderson JT, Beghtel H, et al. β-catenin and TCF mediate cell positioning in the intestinal epithelium by controlling the expression of EphB/EphrinB. *Cell*. 2002;111(2):251-263. doi:10.1016/S0092-8674(02)01015-2

17. Holmberg J, Genander M, Halford MM, et al. EphB Receptors Coordinate Migration and Proliferation in the Intestinal Stem Cell Niche. *Cell*. 2006;125(6):1151-1163. doi:10.1016/j.cell.2006.04.030

18. Teller IC, Beaulieu JF. Interactions between laminin and epithelial cells in intestinal health and disease. *Expert Rev Mol Med*. 2001;3(24):1-18. doi:10.1017/S1462399401003623

19. Mifflin RC, Pinchuk I V., Saada JI, Powell DW. Intestinal myofibroblasts: Targets for stem cell therapy. *Am J Physiol - Gastrointest Liver Physiol*. 2011;300(5):684-696. doi:10.1152/ajpgi.00474.2010

20. Powell DW, Adegboyega PA, Di Mari JF, Mifflin RC. Epithelial cells and their neighbors: I. Role of intestinal myofibroblasts in development, repair, and cancer. *Am J Physiol - Gastrointest Liver Physiol*. 2005;289(1 52-1):2-7. doi:10.1152/ajpgi.00075.2005

21. Sbarbati R. Morphogenesis of the intestinal villi of the mouse embryo: chance and spatial necessity. *J Anat*. 1982;135(3):477-499. http://www.ncbi.nlm.nih.gov/pubmed/7153168%0Ahttp://www.pubmedcentral.nih.gov/articlerender.fcgi?artid=PMC1169398.

22. Shyer AE, Tallinen T, Nerurkar NL, et al. Villification: How the gut gets its villi. *Science*. 2013;342(6155):212-218. doi:10.1126/science.1238842

23. Bonnans C, Chou J, Werb Z. Remodelling the extracellular matrix in development and disease. *Nat Rev Mol Cell Biol*. 2014;15(12):786-801. doi:10.1038/nrm3904

24. Powell DW, Mifflin RC, Valentich JD, Crowe SE, Saada JI, West AB. Myofibroblasts. II. Intestinal subepithelial myofibroblast. *Am J Physiol - Cell Physiol*. 1999;5(3):108-111. doi:10.1177/175114370400500315

25. Powell DW, Mifflin RC, Valentich JD, Crowe SE, Saada JI, West AB.

Myofibroblasts. I. Paracrine cells important in health and disease. *Am J Physiol*. 1999;32(3):245-247. doi:10.1177/153857449803200307

26. van Es JH, Haegebarth A, Kujala P, et al. A Critical Role for the Wnt Effector Tcf4 in Adult Intestinal Homeostatic Self-Renewal. *Mol Cell Biol*. 2012;32(10):1918-1927. doi:10.1128/mcb.06288-11

27. Durand A, Donahue B, Peignon G, et al. Functional intestinal stem cells after Paneth cell ablation induced by the loss of transcription factor Math1 (Atoh1). *PNAS*. 2012;109(23):8965-8970. doi:10.1073/pnas.1201652109

28. Lei NY, Jabaji Z, Wang J, et al. Intestinal subepithelial myofibroblasts support the growth of intestinal epithelial stem cells. *PLoS One*. 2014;9(1). doi:10.1371/journal.pone.0084651

29. Lahar N, Lei NY, Wang J, et al. Intestinal subepithelial myofibroblasts support in vitro and in vivo growth of human small intestinal epithelium. *PLoS One*. 2011;6(11):1-9. doi:10.1371/journal.pone.0026898

30. Kabiri Z, Greicius G, Madan B, et al. Stroma provides an intestinal stem cell niche in the absence of epithelial Wnts. *Dev*. 2014;141(11):2206-2215. doi:10.1242/dev.104976

31. Kosinski C, Li VSW, Chan ASY, et al. Gene expression patterns of human colon tops and basal crypts and BMP antagonists as intestinal stem cell niche factors. *PNAS*. 2007;104(39):15418-15423. doi:10.1073/pnas.0707210104

32. McCarthy N, Manieri E, Storm EE, et al. Distinct Mesenchymal Cell Populations Generate the Essential Intestinal BMP Signaling Gradient. *Cell Stem Cell*. 2020;26(3):391-402.e5. doi:10.1016/j.stem.2020.01.008

33. McCarthy N, Kraiczy J, Shivdasani RA. Cellular and molecular architecture of the intestinal stem cell niche. *Nat Cell Biol*. 2020;22(9):1033-1041. doi:10.1038/s41556-020-0567-z

34. He XC, Zhang J, Tong WG, et al. BMP signaling inhibits intestinal stem cell self-renewal through suppression of Wnt-β-catenin signaling. *Nat Genet*. 2004;36(10):1117-1121. doi:10.1038/ng1430

35. Jardé T, Chan WH, Rossello FJ, et al. Mesenchymal Niche-Derived Neuregulin-1 Drives Intestinal Stem Cell Proliferation and Regeneration of Damaged Epithelium. *Cell Stem Cell*. 2020;27(4):646-662.e7. doi:10.1016/j.stem.2020.06.021

36. Iizuka M, Konno S. Wound healing of intestinal epithelial cells. *World J Gastroenterol*. 2011;17(17):2161-2171. doi:10.3748/wjg.v17.i17.2161

37. McKaig BC, Makh SS, Hawkey CJ, Podolsky DK, Mahida YR. Normal human colonic subepithelial myofibroblasts enhance epithelial migration

(restitution) via TGF-β3. *Am J Physiol - Gastrointest Liver Physiol*. 1999;276(5 39-5):1087-1093. doi:10.1152/ajpgi.1999.276.5.g1087

38. Mckaig BC, Hughes K, Tighe PJ, Mahida AYR. Differential expression of TGF-β isoforms by normal and inflammatory bowel disease intestinal myofibroblasts. *Am J Physiol - Cell Physiol*. 2002;282(1 51-1):172-182. doi:10.1152/ajpcell.00048.2001

39. Gabbiani G, Ryan GB, Majno G. Presence of Modified Fibroblasts in Granulation Tissue and their Possible Role in Wound Contraction. *New York*. 1971:549-550.

40. Gorono RMR, Petroll WM, Cheat W-T, et al. Radial Keratofomy II. Role of the Myofibroblast in Corneal Wound Contraction. *Invest Ophthalmol Vis Sci*. 1992;33(12):3271-3282.

41. Jester J V., Petroll WM, Cavanagh HD. Corneal stromal wound healing in refractive surgery: The role of myofibroblasts. *Prog Retin Eye Res*. 1999;18(3):311-356. doi:10.1016/S1350-9462(98)00021-4

42. Tomasek JJ, Gabbiani G, Hinz B, Chaponnier C, Brown RA. Myofibroblasts and mechanoregulation of connective tissue remodelling. *Nat Rev Mol Cell Biol*. 2002;3(5):349-363. doi:10.1038/nrm809

43. Seltana A, Basora N, Beaulieu JF. Intestinal epithelial wound healing assay in an epithelial-mesenchymal co-culture system. *Wound Repair Regen*. 2010;18(1):114-122. doi:10.1111/j.1524-475X.2009.00554.x

44. Hidalgo IJ, Raub TJ, Borchardt RT. Characterization of the Human Colon Carcinoma Cell Line (Caco-2) as a Model System for Intestinal Epithelial Permeability. *Gastroenterology*. 1989;96(2):736-749. doi:10.1016/S0016-5085(89)80072-1

45. Brück S, Strohmeier J, Busch D, Drozdzik M, Oswald S. Caco-2 cells – expression, regulation and function of drug transporters compared with human jejunal tissue. *Biopharm Drug Dispos*. 2017;38(2):115-126. doi:10.1002/bdd.2025

46. Kang T, Guan R, Chen X, Song Y, Jiang H, Zhao J. In vitro toxicity of different-sized ZnO nanoparticles in Caco-2 cells. *Nanoscale Res Lett*. 2013;8(1):1-8. doi:10.1186/1556-276X-8-496

47. Sun H, Chow ECY, Liu S, Du Y, Pang KS. The Caco-2 cell monolayer: Usefulness and limitations. *Expert Opin Drug Metab Toxicol*. 2008;4(4):395-411. doi:10.1517/17425255.4.4.395

48. Sambuy Y, De Angelis I, Ranaldi G, Scarino ML, Stammati A, Zucco F. The Caco-2 cell line as a model of the intestinal barrier: Influence of cell and culture-related factors on Caco-2 cell functional characteristics. *Cell Biol*

Toxicol. 2005;21(1):1-26. doi:10.1007/s10565-005-0085-6

49. Sotres J, Jankovskaja S, Wannerberger K, Arnebrant T. Ex-Vivo Force Spectroscopy of Intestinal Mucosa Reveals the Mechanical Properties of Mucus Blankets. *Sci Rep*. 2017;7(1):1-14. doi:10.1038/s41598-017-07552-7

50. Yu J, Peng S, Luo D, March JC. In vitro 3D human small intestinal villous model for drug permeability determination. *Biotechnol Bioeng*. 2012;109(9):2173-2178. doi:10.1002/bit.24518

51. Nguyen QT, Hwang Y, Chen AC, Varghese S, Sah RL. Cartilage-like mechanical properties of poly (ethylene glycol)-diacrylate hydrogels. *Biomaterials*. 2012;33(28):6682-6690. doi:10.1016/j.biomaterials.2012.06.005

52. Gjorevski N, Sachs N, Manfrin A, et al. Designer matrices for intestinal stem cell and organoid culture. *Nature*. 2016;539(7630):560-564. doi:10.1038/nature20168

53. Sato T, Vries RG, Snippert HJ, et al. Single Lgr5 stem cells build crypt-villus structures in vitro without a mesenchymal niche. *Nature*. 2009;459(7244):262-265. doi:10.1038/nature07935

54. Dekkers JF, Wiegerinck CL, De Jonge HR, et al. A functional CFTR assay using primary cystic fibrosis intestinal organoids. *Nat Med*. 2013;19(7):939-945. doi:10.1038/nm.3201

55. Fumagalli A, Drost J, Suijkerbuijk SJE, et al. Genetic dissection of colorectal cancer progression by orthotopic transplantation of engineered cancer organoids. *PNAS*. 2017;114(12):E2357-E2364. doi:10.1073/pnas.1701219114

56. Spence JR, Mayhew CN, Rankin SA, et al. Directed differentiation of human pluripotent stem cells into intestinal tissue in vitro. *Nature*. 2011;470(7332):105-110. doi:10.1038/nature09691

57. Yui S, Nakamura T, Sato T, et al. Functional engraftment of colon epithelium expanded in vitro from a single adult Lgr5+ stem cell. *Nat Med*. 2012;18(4):618-623. doi:10.1038/nm.2695

58. Wang Y, DiSalvo M, Gunasekara DB, et al. Self-renewing Monolayer of Primary Colonic or Rectal Epithelial Cells. *Cmgh*. 2017;4(1):165-182.e7. doi:10.1016/j.jcmgh.2017.02.011

59. Thorne CA, Chen IW, Sanman LE, Cobb MH, Wu LF, Altschuler SJ. Enteroid Monolayers Reveal an Autonomous WNT and BMP Circuit Controlling Intestinal Epithelial Growth and Organization. *Dev Cell*. 2018;44(5):624-633.e4. doi:10.1016/j.devcel.2018.01.024

60. Altay G, Larrañaga E, Tosi S, et al. Self-organized intestinal epithelial monolayers in crypt and villus-like domains show effective barrier function. *Sci Rep*. 2019;9(1):1-14. doi:10.1038/s41598-019-46497-x

61. Sen AK, Raj A, Banerjee U, Iqbal SR. *Soft Lithography, Molding, and Micromachining Techniques for Polymer Micro Devices.*; 2019.

62. Wright NA, Carter J, Irwin M. The measurement of villus cell population size in the mouse small intestine in normal and abnormal states: a comparison of absolute measurements with morphometric estimators in sectioned immersion-fixed material. *Cell Tissue Kinet*. 1989;22(6):425-450. doi:10.1111/j.1365-2184.1989.tb00227.x

63. Pereira C, Araújo F, Barrias CC, Granja PL, Sarmento B. Dissecting stromal-epithelial interactions in a 3D invitro cellularized intestinal model for permeability studies. *Biomaterials*. 2015;56:36-45. doi:10.1016/j.biomaterials.2015.03.054

64. Pereira e Silva A, Soares JRA, Mattos EB de A, et al. A histomorphometric classification system for normal and inflamed mouse duodenum—Quali-quantitative approach. *Int J Exp Pathol*. 2018;99(4):189-198. doi:10.1111/iep.12286

65. Wang Y, Gunasekara DB, Reed MI, et al. A microengineered collagen scaffold for generating a polarized crypt-villus architecture of human small intestinal epithelium. *Biomaterials*. 2017;128:44-55. doi:10.1016/j.biomaterials.2017.03.005

66. Verhulsel M, Simon A, Bernheim-Dennery M, et al. Developing an advanced gut on chip model enabling the study of epithelial cell/fibroblast interactions. *Lab Chip*. 2020. doi:10.1039/d0lc00672f

67. Wang Y, Gunasekara DB, Reed MI, et al. A microengineered collagen scaffold for generating a polarized crypt-villus architecture of human small intestinal epithelium. *Biomaterials*. 2017;128:44-55. doi:10.1016/j.biomaterials.2017.03.005

68. Nikolaev M, Mitrofanova O, Broguiere N, et al. Homeostatic mini-intestines through scaffold-guided organoid morphogenesis. *Nature*. 2020;585(7826):574–578. doi:10.1038/s41586-020-2724-8

69. Castaño AG, García-Díaz M, Torras N, Altay G, Comelles J, Martínez E. Dynamic photopolymerization produces complex microstructures on hydrogels in a moldless approach to generate a 3D intestinal tissue model. *Biofabrication*. 2019;11(2). doi:10.1088/1758-5090/ab0478

70. Creff J, Courson R, Mangeat T, et al. Fabrication of 3D scaffolds reproducing intestinal epithelium topography by high-resolution 3D stereolithography. *Biomaterials*. 2019;221(119404):1-13.

doi:10.1016/j.biomaterials.2019.119404

71. Torras N, Zabalo J, Abril E, Carré A, García-díaz M, Martínez E. A simple DLP-bioprinting strategy produces cell-laden crypt- villous structures for an advanced 3D gut model. *bioRxiv*. 2022:1-31.

72. Ahmad AA, Wang Y, Sims CE, Magness ST, Allbritton NL. Optimizing Wnt-3a and R-spondin1 concentrations for stem cell renewal and differentiation in intestinal organoids using a gradient-forming microdevice. *RSC Adv*. 2015;5(91):74881-74891. doi:10.1039/c5ra14923a

73. Attayek PJ, Ahmad AA, Wang Y, et al. In vitro polarization of colonoids to create an intestinal stem cell compartment. *PLoS One*. 2016;11(4):1-23. doi:10.1371/journal.pone.0153795

74. Vila A, Torras N, Castaño AG, et al. Hydrogel co-networks of gelatine methacrylate and poly(ethylene glycol) diacrylate sustain 3D functional in vitro models of intestinal mucosa. *Biofabrication*. 2019;12:1-16. doi:10.1088/1758-5090/ab5f50

75. Torras N, Zabalo J, Abril E, Carré A, García-díaz M. A simple DLP-bioprinting strategy produces cell-laden crypt- villous structures for an advanced 3D gut model . 2022:1-31.

76. Rossi G, Manfrin A, Lutolf MP. Progress and potential in organoid research. *Nat Rev Genet*. 2018;19(11):671-687. doi:10.1038/s41576-018-0051-9

77. Li N, Wang D, Sui Z, et al. Development of an improved three-dimensional in vitro intestinal mucosa model for drug absorption evaluation. *Tissue Eng - Part C Methods*. 2013;19(9):708-719. doi:10.1089/ten.tec.2012.0463

78. Sato T, Clevers H. Growing self-organizing mini-guts from a single intestinal stem cell: Mechanism and applications. *Science*. 2013;340(6137):1190-1194. doi:10.1126/science.1234852

79. Barker N, Van Es JH, Kuipers J, et al. Identification of stem cells in small intestine and colon by marker gene Lgr5. *Nature*. 2007;449(7165):1003-1007. doi:10.1038/nature06196

80. Dekkers JF, Alieva M, Wellens LM, et al. High-resolution 3D imaging of fixed and cleared organoids. *Nat Protoc*. 2019;14(6):1756-1771. doi:10.1038/s41596-019-0160-8

81. Barriga FM, Montagni E, Mana M, et al. Mex3a Marks a Slowly Dividing Subpopulation of Lgr5^{+} Intestinal Stem Cells. *Cell Stem Cell*. 2017;20(6):801-816. doi:10.1016/j.stem.2017.02.007

82. Fernández-Majada V, Welz P-S, Ermolaeva MA, et al. The tumour suppressor CYLD regulates the p53 DNA damage response. *Nat Commun*. 2016;7:12508.

doi:10.1038/ncomms12508

83. Watanabe K, Ueno M, Kamiya D, et al. A ROCK inhibitor permits survival of dissociated human embryonic stem cells. *Nat Biotechnol*. 2007;25(6):681-686. doi:10.1038/nbt1310

84. Khalil H, Nie W, Edwards RA, Yoo J. Isolation of primary myofibroblasts from mouse and human colon tissue. *J Vis Exp*. 2013;(80):1-6. doi:10.3791/50611

85. Altay G. Towards the development of biomimetic in vitro models of intestinal epithelium derived from intestinal organoids. *TDX (Tesis Dr en Xarxa)*. 2018.

86. Altay G, Abad-Lázaro A, Gualda EJ, et al. Modelling biochemical gradients in vitro to control cell compartmentalization in a microengineered 3D model of the intestinal epithelium. *Adv Healthc Mater*. 2022;2201172:1-15. doi:10.1002/adhm.202201172

87. Zheng GXY, Terry JM, Belgrader P, et al. Massively parallel digital transcriptional profiling of single cells. *Nat Commun*. 2017;8. doi:10.1038/ncomms14049

88. Larrañaga E. Effects of substrate-derived cues in driving the selforganization of organoid-derived intestinal epithelia. *TDX (Tesis Dr en Xarxa)*. 2021.

89. Altay G, Batlle E, Fernández-Majada V, Martínez E. In vitro Self-organized Mouse Small Intestinal Epithelial Monolayer Protocol. *Bio-Protocol*. 2020;10(3):1-21. doi:10.21769/bioprotoc.3514

90. Thielicke W, Stamhuis EJ. PIVlab – Towards User-friendly, Affordable and Accurate Digital Particle Image Velocimetry in MATLAB. *J Open Res Softw*. 2014;2. doi:10.5334/jors.bl

91. Loessner D, Meinert C, Kaemmerer E, et al. Functionalization, preparation and use of cell-laden gelatin methacryloyl-based hydrogels as modular tissue culture platforms. *Nat Protoc*. 2016;11(4):727-746. doi:10.1038/nprot.2016.037

92. Van Den Bulcke AI, Bogdanov B, De Rooze N, Schacht EH, Cornelissen M, Berghmans H. Structural and rheological properties of methacrylamide modified gelatin hydrogels. *Biomacromolecules*. 2000;1(1):31-38. doi:10.1021/bm990017d

93. Vila A, Torras N, Castaño AG, et al. Hydrogel co-networks of gelatine methacrylate and poly(ethylene glycol) diacrylate sustain 3D functional in vitro models of intestinal mucosa. *Biofabrication*. 2020;12(2). doi:10.1088/1758-5090/ab5f50

94. Vila A. Hydrogel co-networks of gelatin methacryloyl and poly(ethylene glycol)diacrylate sustain 3D functional in vitro models of intestinal mucosa.

TDX (Tesis Dr en Xarxa). 2020.

95. Habeeb AFSA. Determination of free amino groups in proteins by trinitrobenzenesulfonic acid. *Anal Biochem*. 1966;14(3):328-336. doi:10.1016/0003-2697(66)90275-2

96. Anseth KS, Bowman CN, Brannon-Peppas L. Mechanical properties of hydrogels and their experimental determination. *Biomaterials*. 1996;17(17):1647-1657. doi:10.1016/0142-9612(96)87644-7

97. Ahearne M, Yang Y, El Haj AJ, Then KY, Liu KK. Characterizing the viscoelastic properties of thin hydrogel-based constructs for tissue engineering applications. *J R Soc Interface*. 2005;2(5):455-463. doi:10.1098/rsif.2005.0065

98. Altay G, Tosi S, García-Díaz M, Martínez E. Imaging the Cell Morphological Response to 3D Topography and Curvature in Engineered Intestinal Tissues. *Front Bioeng Biotechnol*. 2020;8(April):1-12. doi:10.3389/fbioe.2020.00294

99. Schmidt U, Weigert M, Broaddus C, Myers G. *Cell Detection with Star-Convex Polygons*.; 2018. doi:10.1007/978-3-030-00934-2_30

100. Bollenbach T, Heisenberg CP. Gradients Are Shaping Up. *Cell*. 2015;161(3):431-432. doi:10.1016/j.cell.2015.04.009

101. Castaño AG. Engineering poly (ethylene glycol) diacrylate-based microstructures to develop an in vitro model of small intestinal epithelium. *TDX (Tesis Dr en Xarxa)*. 2017.

102. Kelly P, Menzies I, Crane R, et al. Responses of small intestinal architecture and function over time to environmental factors in a tropical population. *Am J Trop Med Hyg*. 2004;70(4):412-419. doi:10.4269/ajtmh.2004.70.412

103. Marsh MN, Swift JA. A study of the small intestinal mucosa using the scanning electron microscope. *Gut*. 1969;10(11):940-949. doi:10.1136/gut.10.11.940

104. Peppas NA, Merrill EW. Crosslinked poly(vinyl alcohol) hydrogels as swollen elastic networks. *J Appl Polym Sci*. 1977;21(7):1763-1770. doi:10.1002/app.1977.070210704

105. Peppas NA, Bures P, Leobandung W, Ichikawa H. Hydrogels in pharmaceutical formulations. *Eur J Pharm Biopharm*. 2000;50(1):27-46. doi:10.1016/S0939-6411(00)00090-4

106. Yang T. *Mechanical and Swelling Properties of Hydrogels*.; 2012.

107. Weber LM, Lopez CG, Anseth KS. Effects of PEG hydrogel crosslinking density on protein diffusion and encapsulated islet survival and function. *J Biomed Mater Res A*. 2009;90(3):720-729. doi:10.1002/jbm.a.32134

108. Lee S, Tong X, Yang F. The effects of varying poly(ethylene glycol) hydrogel crosslinking density and the crosslinking mechanism on protein accumulation in three-dimensional hydrogels. *Acta Biomater*. 2014;10(10):4167-4174. doi:10.1016/j.actbio.2014.05.023

109. Moll R, Schiller DL, Franke WW. Identification of protein IT of the intestinal cytoskeleton as a novel type I cytokeratin with unusual properties and expression patterns. *J Cell Biol*. 1990;111(2):567-580. doi:10.1083/jcb.111.2.567

110. Valenta T, Degirmenci B, Moor AE, et al. Wnt Ligands Secreted by Subepithelial Mesenchymal Cells Are Essential for the Survival of Intestinal Stem Cells and Gut Homeostasis. *Cell Rep*. 2016;15(5):911-918. doi:10.1016/j.celrep.2016.03.088

111. Kim JE, Fei L, Yin WC, et al. Single cell and genetic analyses reveal conserved populations and signaling mechanisms of gastrointestinal stromal niches. *Nat Commun*. 2020;11(1):1-15. doi:10.1038/s41467-019-14058-5

112. McCarthy N, Tie G, Madha S, et al. Smooth muscle contributes to the development and function of a layered intestinal stem cell niche. *Dev Cell*. 2023:1-15. doi:10.1016/j.devcel.2023.02.012

113. Sato T, Stange DE, Ferrante M, et al. Long-term expansion of epithelial organoids from human colon, adenoma, adenocarcinoma, and Barrett's epithelium. *Gastroenterology*. 2011;141(5):1762-1772. doi:10.1053/j.gastro.2011.07.050

114. Cheng H, Leblond CP. Origin, differentiation and renewal of the four main epithelial cell types in the mouse small intestine IV. Paneth cells. *Am J Anat*. 1974;141(4):521-535. doi:10.1002/aja.1001410406

115. Provenzano PP, Eliceiri KW, Campbell JM, Inman DR, White JG, Keely PJ. Collagen reorganization at the tumor-stromal interface facilitates local invasion. *BMC Med*. 2006;16:1-15. doi:10.1186/1741-7015-4-38

116. Han W, Chen S, Yuan W, et al. Oriented collagen fibers direct tumor cell intravasation. *PNAS*. 2016;113(40):11208-11213. doi:10.1073/pnas.1610347113

117. Abbas B, Hayes TL, Wilson DJ, Carr KE. Internal structure of the intestinal villus: morphological and morphometric observations at different levels of the mouse villus. *J Anat*. 1989;162:263-273..

118. Roulis M, Flavell RA. Fibroblasts and myofibroblasts of the intestinal lamina propria in physiology and disease. *Differentiation*. 2016;92(3):116-131. doi:10.1016/j.diff.2016.05.002

119. Li ACY, Thompson RPH. Basement membrane components. *J Clin Pathol*.

2003;56(12):885-887. doi:10.1136/jcp.56.12.885

120. Pieuchot L, Marteau J, Guignandon A, et al. Curvotaxis directs cell migration through cell-scale curvature landscapes. *Nat Commun*. 2018;9(1). doi:10.1038/s41467-018-06494-6

121. Dutton JS, Hinman SS, Kim R, Wang Y, Allbritton NL. Primary Cell-Derived Intestinal Models: Recapitulating Physiology. *Trends Biotechnol*. 2019;37(7):744-760. doi:10.1016/j.tibtech.2018.12.001

122. Balimane P V., Chong S. Cell culture-based models for intestinal permeability: A critique. *Drug Discov Today*. 2005;10(5):335-343. doi:10.1016/S1359-6446(04)03354-9

123. Sumigray KD, Terwilliger M, Lechler T. Morphogenesis and Compartmentalization of the Intestinal Crypt. *Dev Cell*. 2018;45(2):183-197.e5. doi:10.1016/j.devcel.2018.03.024

124. Zhao J, de Vera J, Narushima S, et al. R-spondin1, A Novel Intestinotrophic Mitogen, Ameliorates Experimental Colitis in Mice. *Gastroenterology*. 2007;132(4):1331-1343. doi:10.1053/j.gastro.2007.02.001

125. Lin C-C, Ki CS, Shih H. Thiol-norbornene photo-click hydrogels for tissue engineering applications. *J Appl Polym Sci*. 2015;132(8). doi:10.1002/app.41563.Thiol-norbornene

126. Farin HF, Jordens I, Mosa MH, et al. Visualization of a short-range Wnt gradient in the intestinal stem-cell niche. *Nature*. 2016;530(7590):340-343. doi:10.1038/nature16937

127. Serra D, Mayr U, Boni A, et al. Self-organization and symmetry breaking in intestinal organoid development. *Nature*. 2019. doi:10.1038/s41586-019-1146-y

128. Engler AJ, Sen S, Sweeney HL, Discher DE. Matrix Elasticity Directs Stem Cell Lineage Specification. *Cell*. 2006;126(4):677-689. doi:10.1016/j.cell.2006.06.044

129. Wells RG. The role of matrix stiffness in regulating cell behavior. *Hepatology*. 2008;47(4):1394-1400. doi:10.1002/hep.22193

130. Srinivasan B, Kolli AR, Esch MB, Abaci HE, Shuler ML, Hickman JJ. TEER Measurement Techniques for In Vitro Barrier Model Systems. *J Lab Autom*. 2015;20(2):107-126. doi:10.1177/2211068214561025

131. Kobel S, Lutolf MP. Biomaterials meet microfluidics: Building the next generation of artificial niches. *Curr Opin Biotechnol*. 2011;22(5):690-697. doi:10.1016/j.copbio.2011.07.001

132. Fung WT, Beyzavi A, Abgrall P, Nguyen NT, Li HY. Microfluidic platform for controlling the differentiation of embryoid bodies. *Lab Chip*. 2009;9(17):2591-2595. doi:10.1039/b903753e

133. Xi W, Saleh J, Yamada A, et al. Modulation of designer biomimetic matrices for optimized differentiated intestinal epithelial cultures. *Biomaterials*. 2022;282:121380. doi:10.1016/j.biomaterials.2022.121380

134. Gehart H, Clevers H. Tales from the crypt: new insights into intestinal stem cells. *Nat Rev Gastroenterol Hepatol*. 2019;16(1):19-34. doi:10.1038/s41575-018-0081-y

135. van Mourik JA, Leeksma OC, Reinders JH, de Groot PG, Zandbergen-Spaargaren J. Vascular endothelial cells synthesize a plasma membrane protein indistinguishable from the platelet membrane glycoprotein IIa. *J Biol Chem*. 1985;260(20):11300-11306. doi:10.1016/s0021-9258(17)39180-9

136. Giltay J, Brinkman H, Modderman P, von dem Borne A, van Mourik J. Human vascular endothelial cells express a membrane protein complex immunochemically indistinguishable from the platelet VLA-2 (glycoprotein Ia-IIa) complex. *Blood*. 1989;73(5):1235-1241. doi:10.1182/blood.v73.5.1235.1235

137. Muller WA, Ratti CM, Mcdonnell SL, Cohn ZA. A Human Endothelial Cell-restricted Externally Disposed Plasmalemmal Protein enriched in intercellular junctions. *J Exp Med*. 1989;170(August).

138. Albelda SM, Oliver PD, Romer LH, Buck CA. EndoCAM: A novel endothelial cell-cell adhesion molecule. *J Cell Biol*. 1990;110(4):1227-1237. doi:10.1083/jcb.110.4.1227

139. Skene JHP, Willard M. Changes in axonally transported proteins during axon regeneration in toad retinal ganglion cells. *J Cell Biol*. 1981;89(1):86-95. doi:10.1083/jcb.89.1.86

140. Skene JHP, Willard M. Characteristics of growth-associated polypeptides in regenerating toad retinal ganglion cell axons. *J Neurosci*. 1981;1(4):419-426. doi:10.1523/jneurosci.01-04-00419.1981

141. Steisslinger HW, Aloyo VJ, Vitković L. Characterization of two plasma membrane proteins abundant in rat brain. *Brain Res*. 1987;415(2):375-379. doi:10.1016/0006-8993(87)90224-1

142. Hale G, Xia M, Tighe HP, et al. The CAMPATH-1 antigen (CDw52). 1990:118-127.

143. Labernadie A, Kato T, Brugués A, et al. A mechanically active heterotypic E-cadherin/N-cadherin adhesion enables fibroblasts to drive cancer cell invasion. *Nat Cell Biol*. 2017;19(3):224-237. doi:10.1038/ncb3478

144. Sonam S, Balasubramaniam L, Lin SZ, et al. Mechanical stress driven by rigidity sensing governs epithelial stability. *Nat Phys*. 2023;19(1):132-141. doi:10.1038/s41567-022-01826-2

145. Zanca A, Flegg JA, Osborne JM. Push or Pull? Cell Proliferation and Migration During Wound Healing. *Front Syst Biol*. 2022;2(April):1-14. doi:10.3389/fsysb.2022.876075

146. Farooqui R, Fenteany G. Multiple rows of cells behind an epithelial wound edge extend cryptic lamellipodia to collectively drive cell-sheet movement. *J Cell Sci*. 2005;118(1):51-63. doi:10.1242/jcs.01577

147. Viziam CB, Matoltsy AG, Mescon H. Epithelialization of Small Wounds. *J Invest Dermatol*. 1954;43(6):499-507. doi:10.1038/jid.1964.192

148. Garlick JA. Engineering Skin to Study Human Disease – Tissue Models for Cancer Biology and Wound Repair. *Adv Biochem Engin/Biotechnol*. 2006;103(January):207-239.

149. Poujade M, Hertzog A, Jouanneau J, et al. Collective migration of an epithelial monolayer in response to a model wound. *PNAS*. 2007;104(41):15988-15993.

150. Li X, Balagam R, He T, Lee PP, Igoshin OA, Levine H. On the mechanism of long-range orientational order of fibroblasts. 2017. doi:10.1073/pnas.1707210114/

151. Peranzoni E, Rivas A, Bougherara H, Salmon H. Positive and negative influence of the matrix architecture on antitumor immune surveillance. 2013:4431-4448. doi:10.1007/s00018-013-1339-8

152. Lovett M, Ph D, Lee K, et al. Vascularization Strategies for Tissue Engineering. *Tissue Eng - Part B Rev*. 2009;15(3).

153. Werner M, Blanquer SBG, Haimi SP, et al. Surface Curvature Differentially Regulates Stem Cell Migration and Differentiation via Altered Attachment Morphology and Nuclear Deformation. *Adv Sci*. 2017;4(2):1-11. doi:10.1002/advs.201600347

154. Yu SM, Oh JM, Lee J, et al. Substrate curvature affects the shape, orientation, and polarization of renal epithelial cells. *Acta Biomater*. 2018;77:311-321. doi:10.1016/j.actbio.2018.07.019

155. Luciano M, Versaevel M, Vercruysse E, Gabriele S. Mechanoresponse of epithelial monolayers to in-plane and out-of-plane curvatures imposed by 3D microwells. 2022.

8. Resum en català

Avui en dia, el model *in vitro* estàndard de l'intestí prim en el camp del desenvolupament de fàrmacs encara consisteix en una monocapa de cèl·lules cancerígenes sembrades a sobre d'un substrat dur. Malgrat els grans avenços que aquest model ha suposat, no recapitula de manera fidedigna la complexitat del teixit. Recentment, s'ha aconseguit establir el cultiu primari i longeu de cèl·lules de l'epiteli intestinal a través dels anomenats "organoids" intestinals, estructures tridimensionals auto-organitzades que recapitulen moltes de les característiques del teixit nadiu. Tanmateix, presenten vàries limitacions: (i) al ser estructures tancades, l'accés a la part apical és complicat, (ii) per créixer, necessiten estar dins d'una matriu altament heterogènia que dificulta poder establir gradients de factors bioquímics ben controlats, (ii) malgrat recapitular la organització cel·lular del teixit, no mimetitzen la seva arquitectura i (iv) no inclouen el compartiment "estromal" (principalment fibroblasts), malgrat s'hagi demostrat ser essencial en el manteniment del nínxol de cèl·lules mare. Per tant, l'objectiu general d'aquesta tesi és contribuir al desenvolupament de models in vitro de l'epiteli intestinal que incorporin el compartiment "estromal" en diferents nivells.

En la primera secció d'aquesta tesi, hem adaptat amb èxit una tècnica desenvolupada al nostre laboratori que es basa en fotolitografia per fabricar hidrogels de diacrilat de polietilè glicol (PEGDA) amb cavitats semblant a les criptes intestinals. Tot i que la naturalesa de la reacció química emprada va resultar en la presència de polímer parcialment entrellaçat atrapat a les cavitats, la proteïna col·lagen I va poder ser acoblada als hidrogels i es van poder formar monocapes derivades d'organoids a sobre.

En la segona secció d'aquesta tesi, hem desenvolupat un model *in vitro* que permet el cultiu de cèl·lules derivades d'organoids en hidrogels amb unes microestructures que reprodueix les vellositats intestinals sota l'efecte de gradients bioquímics del nínxol de cèl·lules mare. Els hidrogels fabricats tenien una elasticitat semblant a la del teixit nadiu, i les dimensions de les estructures s'assemblaven a les de les vellositats. La mida de la xarxa de l'hidrogel va permetre la difusió de factors del nínxol de cèl·lules mare, els quals van formar gradients estables al llarg de l'eix vertical de les microestructures. Per poder predir els perfils d'aquests gradients, es va desenvolupar un model *in silico* de la difusió de les proteïnes a través del hidrogel. La proteïna col·lagen I es va acoblar als hidrogels i això va permetre el creixement de cèl·lules derivades d'organoides, les quals van crear monocapes completes. Només quan aquestes van ser cultivades sota gradients de factors del nínxol de cèl·lules mare, en contraposició a concentracions uniformes d'aquests, van mostrar una organització cel·lular semblant a la del teixit nadiu. Sota gradients que

fomentaven la proliferació, les monocapes van créixer més ràpid però això va comportar una severa reducció de la població de cèl·lules proliferatives. Aquests resultats demostren que el model tridimensional d'epiteli intestinal desenvolupat aquí recapitula l'organització cel·lular que es troba *in vivo*. Aquest model podria ser utilitzat per analitzar de manera sistemàtica l'efecte de gradients de factors, sobretot aquells provinents de fibroblasts, i estudiar la resposta cel·lular.

La tercera secció d'aquesta tesi ha tingut per objectiu l'estudi de l'hipotètic efecte físic dels fibroblasts en la migració de les cèl·lules epitelials en condicions no patològiques. A través del cocultiu de fibroblasts amb organoids intestinals, hem vist que la senyalització paracrina dels fibroblasts indueix una morfologia esfèrica en els organoides, mentre que la presència física dels fibroblasts dona lloc a una transició dels organoides cap a monocapes bidimensionals. Aquest efecte físic dels fibroblasts també es va observar en un model bidimensional *in vitro* de cocultiu. Monocapes derivades d'organoids exposades a un espai lliure de cèl·lules (forat) van migrar direccionalment cap al forat i van aconseguir tancar-lo. Durant aquest procés, vam observar que els fibroblasts també migraven, però cap a la monocapa epitelial. A més, s'alineaven perpendicularment al front de migració i produïen proteïnes de la matriu extracel·lular alineades de la mateixa manera, creant carrils que podrien estan sent utilitzats per les cèl·lules epitelials per migrar direccionalment. Sota només la senyalització paracrina dels fibroblasts, les monocapes no van migrar tan eficientment i no van tancar els forats. Sota cap efecte provinent dels fibroblasts, les cèl·lules epitelials migraven de manera aleatòria i recuperaven la integritat del teixit.

Vist el rol físic dels fibroblasts en l'epiteli intestinal, en la quarta secció d'aquesta tesi hem volgut desenvolupar un model *in vitro* que inclogués el compartiment "estromal", juntament amb el teixit epitelial, i que a la vegada captures l'arquitectura del teixit nadiu. Per dur-ho a terme, vam emprar una tecnologia de bioimpressió 3D desenvolupada al nostre laboratori per fabricar hidrogels de metacriloil de gelatina (GelMA) i PEGDA plans i amb microestructures mimetitzant les vellositats intestinals. Primer, en hidrogels plans, els fibroblasts encapsulats van mostrar ser viables, tenir capacitat de proliferar i estirar-se sobre la superfície dels hidrogels. Cèl·lules derivades d'organoids sembrades sobre els hidrogels només van poder créixer quan hi havia fibroblasts encapsulats a dins. En hidrogels amb microestructures, els fibroblasts encapsulats es van posicionar a la superfície, igual que ho feien en hidrogels plans, però preferentment a les puntes de les microestructures. Les cèl·lules epitelials sembrades a sobre van créixer principalment a les puntes i a les valls de les microestructures. En aquests co-cultius, els fibroblasts es van col·locar principalment sota de les epitelials. Els fibroblasts en co-cultiu van mostrar tenir un nucli més allargat que els fibroblasts cultivats sense epitelials a sobre,

indicant una comunicació física entre els dos tipus cel·lulars. En conjunt, hem desenvolupat un model *in vitro* que mimetitza l'arquitectura del teixit nadiu i conté, no només l'epiteli, sinó també el compartiment "estromal". A través d'aquesta plataforma, hem pogut veure una comunicació bidireccional entre les cèl·lules epitelials i els fibroblasts.